LATVIAN JOURNAL of PHYSICS and TECHNICAL SCIENCES

ISSN 0868 - 8257

3

(Vol. 61)

2024

CONTENTS

LATVIAN
JOURNAL
of
PHYSICS
and TECHNICAL
SCIENCES

LATVIJAS
FIZIKAS
un TEHNISKO
ZINĀTŅU
ŽURNĀLS

Published six times a year since February 1964
Iznāk sešas reizes gadā kopš 1964. gada februāra

3 (Vol. 61) • 2024

RĪGA

Language Editor: O. Ivanova
Computer Designer: I. Begicevs

INDEXED (PUBLISHED) IN

www.scopus.com
www.sciendo.com
EBSCO (Academic Search Complete, www.epnet.com), INSPEC (www.iee.org.com).
VINITI (www.viniti.ru), Begell House Inc/ (EDC, www.edata-center.com).

Issuers: Institute of Physical Energetics,
Institute of Solid State Physics, University of Latvia
Registration Certificate Number: 000700221

Editorial Contacts:
14 Dzerbenes Street, Riga, LV-1006
LATVIA
tel: +371 26245896
M: +371 29363105
leo@lza.lv

LATVIAN JOURNAL OF PHYSICS
AND TECHNICAL SCIENCES
2024, N 3

DOI: 10.2478/lpts-2024-0016

INVESTIGATION OF PHASE SEPARATION AND MORPHOLOGY OF ORGANIC-INORGANIC INTERPENETRATING POLYMER NETWORKS

T. Tsebriienko*, A. Popov

Institute of Solid State Physics, University of Latvia,
8 Kengaraga Str., Riga, LV-1063, LATVIA
*e-mail tamara.tsebriienko@cfi.lu.lv

The paper investigates the process of phase separation and morphology of organic-inorganic interpenetrating polymer networks (OI IPNs) based on the cross-linked polyurethane (PU), poly(hydroxyethyl methacrylate) (PHEMA) and poly(titanium oxide) $(–TiO_2–)_n$ obtained by sol-gel method in the presence of poly(oxypropylene glycol) (POPG) at various molar ratio of titanium (IV) isopropoxide ($Ti(OPr^i)_4$) and water. It has been established that the phase separation in OI IPNs depends on the kinetics of PHEMA-component formation and it occurs through the mechanism of the spinodal decomposition. It has been shown that by varying the ratio of IPNs components, content of inorganic component and $Ti(OPr^i)_4/H_2O$ molar ratio it is possible to control the phase separation process and obtain OI IPNs with a different phase structure.

Keywords: *Interpenetrating polymer networks, light scattering, phase separation, poly (titanium oxide), radical polymerization.*

1. INTRODUCTION

One of the ways to solve the problem of creating new materials with the required complex of physical and mechanical properties is to obtain polymer blends, which allows combining the valuable properties of each component. A promising method for obtaining such blends is reaction mixing, in particular, the synthesis of interpenetrating polymer networks (IPNs) [1], [2].

A specific feature of IPNs is that at a certain stage of cross-linking reactions, phase separation occurs as a result of thermodynamic incompatibility of high-molecular components and, as a consequence, the structure of such a system becomes heterogeneous [3], [4]. Since the phase separation process and chemical reactions occur simultaneously, the composition and ratio of components change with time. Thus, the IPNs formation proceeds under thermodynamically non-equilibrium conditions. In addition, this process is usually incomplete due to the high viscosity and the entanglement of the chains causing the "forced" kinetic stability of the networks without macrophase formation of the components. The final structure of such polymer systems is conventionally characterised by the presence of three regions of different composition: two phases and the interfacial region (IFR), which is a measure of the unseparated part of the system [2]. The larger the IFR fraction, the smaller the degree of separation and the higher the nonequilibrium of the system as a whole.

The whole complex of properties of IPNs is determined by their final structure, which depends on the phase separation rate. In turn, the phase separation rate is determined by the kinetics of chemical reactions of IPN components formation. Therefore, it is possible to control the phase separation process by changing the factors affecting the reaction rate. These are temperature, ratio of components, concentration of polymerisation initiator, presence of catalyst, crosslinking agent, filler and compatibiliser, curing sequence [3], [4]. Depending on the conditions of IPN formation, phase separation can occur either by the nucleation and growth or by the spinodal decomposition mechanism [3], [4].

While the phase separation process for IPNs has been studied quite fully [2]–[4], there are practically no data on the study of phase separation in organic-inorganic interpenetrating polymer networks.

One of the most promising inorganic components of OI IPNs is titanium dioxide TiO_2 in amorphous or crystalline state. This is due to its wide range of applications for the implementation of photochemical processes, for the creation of membranes, catalytic sensors, photosensitive materials, for stimulation of various biochemical and biophysical processes [5]–[15].

The promising sol-gel method is used to obtain the inorganic component of the OI IPNs due to its simplicity, environmental safety and the possibility of its uniform distribution in the polymer matrix even at the molecular level [16].

Works on the incorporation of poly (titanium oxide) gel into an organic matrix began to appear about fifteenth years ago. The organic component in such organo-inorganic materials has traditionally been represented by the acrylate [17], [18]. In these works, for such purposes, a unique mixture of thermodynamically incompatible polymers was chosen, but it was linked to each other due to the mechanical interweaving of polymer chains at the molecular level. At this moment, there is little information about the preparation and study of such polymer systems.

The aim of the study is to investigate the phase separation process and morphology of OI IPNs based on cross-linked polyurethane, poly(hydroxyethyl methacrylate) and poly(titanium oxide) prepared by sol-gel method in poly(oxypropylene glycol) medium depending on the kinetics of PHEMA component formation.

2. EXPERIMENTAL

Poly(titanium oxide) used as an inorganic component in OI IPNs was synthesized by hydrolysis-condensation reaction of titanium (IV) isopropoxide in POPG medium (MM 1000).

The $Ti(OPr^i)_4/H_2O$ ratio was 1/1 and 1/2 mol/mol, and the $Ti(OPr^i)_4$ content in POPG was 0.5; 5.0; 10.0 wt%, which in terms of TiO_2 was 0.14; 1.40; 2.80 wt%, respectively. The prepared $(–TiO_2–)_n$ gels were evacuated at 85 °C with residual pressure of 2 mm Hg to remove water and isopropyl alcohol, which were formed by hydrolysis-condensation reactions.

Macrodiisocyanate was synthesized on the base of $(–TiO_2–)_n$ gel and toluylene diisocyanate (TDI) (a mixture of 2,4- and 2,6-TDI isomers in 80/20 wt.% ratio). Further, a crosslinking agent was added to the macrodiisocyanate, and titanium-containing urethane composition was obtained. To form OI IPNs, 2-hydroxyethyl methacrylate (HEMA) was added to this composition with the radical polymerisation initiator 2,2-azobis-isobutyronitrile (AIBN) at a concentration of 0.025 mol/L. After stirring, the reaction mixture was poured into an antiadhesive treated hermetic form followed by polymerisation at 60 °C (20 h) and 100 °C (2.5 h). The initial IPNs were prepared on the basis of PU and PHEMA without $(–TiO_2–)_n$. The ratio of PU/PHEMA components in the initial and OI IPNs was 70/30, 50/50, 30/70 wt%.

The kinetics of polymerization of initial PU, titanium-containing PU, initial IPNs and OI IPNs were studied at 60 °C on a DAK-1-1A differential calorimeter.

The study of the formation kinetics of initial PU and titanium-containing PU showed that $(–TiO_2–)_n$ acted as a catalyst for the urethane formation reaction. For pure PU, the reaction rate constant (K_r) was $6.4 \cdot 10^{-5}$ kg/mol·s, while for titanium-containing PU, $K_r = 1.5 \cdot 10^{-4}$ kg/mol·s (0.5% $Ti(OPr^i)_4$ in POPG). Therefore, the HEMA polymerisation process takes place *in situ* in the already formed cross-linked PU. It seemed only possible to investigate the polymerization kinetics of HEMA for IPNs and OI IPNs.

To study the kinetics of PHEMA formation in IPNs and OI IPNs, its parameters such as the time to reach the maximum of reduced rate of PHEMA formation (τ_{max}) and the maximum value of its reduced rate (W_{max}) were determined (Tables 1 and 2). The reduced reaction rate of PHEMA formation calculated from $W_{red} = V/M$, where $V = dM/d\tau$, M is the amount of unreacted monomer and τ is reaction time.

Since the chemical reactions of OI IPN formation are accompanied by phase separation, this process was simultaneously investigated by light scattering. For this purpose, homogeneous reaction mixtures (Ti-containing urethane composition and HEMA with AIBN) were placed between two glasses in the chamber of a light scattering device heated to 60 ºC and the change of light scattering intensity (I) was observed over time (τ). It is known that, regardless of the mechanism of phase separation, the process of transition of the system from a single-phase to a two-phase state is accompanied by a kink in the dependence $I = f(\tau)$. The kink point on this dependence determined the time of phase separation onset. The time dependences of the logarithm of the light scattering intensity at the initial stages of phase separation were linear in all cases. According to [19], this is one of the criteria of the spinodal mechanism of phase separation, and the light scattering data were processed and interpreted in the framework of the Cahn–Hilliard theory [20] to calculate the so-called enhancement factor $2R(q)$. The enhancement factor characterises the rate of increase of concentration fluctuations during isothermal phase separation according to the equation $\ln(I/I_0) = 2R(q)\tau$, where q is the wave number. Generally, phase separation by the spinodal mechanism begins with the formation of a continuously interconnected periodic structure, which gradually shifts to droplet as a result of the decomposition of spinodal structures at the last stages of phase separation due to an increase in the interfacial tension.

The morphology of the obtained initial IPNs and OI IPNs was investigated by optical microscopy.

Table 1. Kinetic Characteristics of HEMA Polymerisation in IPNs and OI IPNs with a Molar Ratio of $Ti(OPr^i)_4/H_2O$ = 1/1 and Parameters of Their Phase Separation

Sample	$(–TiO_2–)_n$ in POPOG, wt%	PU/ PHEMA / $(–TiO_2–)_n$, wt%	$W_{max}\times10^2$, min^{-1}	τ_{max}, min	$\tau_{ps,}$ min	α_{ps}	$2R(q)\cdot10^3$, s
IPNs -1	-	50/50/0	20.00	38	15.0	0.003	4.07
IPNs -2	-	30/70/0	26.00	30	13.5	0.005	5.50
OI IPNs -1	0.14	69.96/29.98/0.06	9.20	51	20.0	0.009	3.17
OI IPNs -2	0.14	49.98/49.98/0.04	-	-	18.0	-	3.40
OI IPNs -3	0.14	29.99/69.98/0.03	-	-	17.5	-	3.67
OI IPNs -4	1.40	69.55/29.78/0.67	3.33	66	PS not observed *		
OI IPNs -5	1.40	49.80/49.80/0.40	15.00	46	PS not observed *		
OI IPNs -6	1.40	29.92/69.80/0.28	20.65	32	25.0	0.015	2.42
OI IPNs -7	2.80	69.08/29.58/1.34	1.05	70	PS not observed *		

* the duration of the experiment for 2 hours

Table 2. Kinetic Characteristics of HEMA Polymerisation in IPNs and OI IPNs with a Molar Ratio of $Ti(OPr^i)_4/H_2O$ = 1/2 and Parameters of Their Phase Separation

Sample	$(–TiO_2–)_n$ in POPOG, wt%	PU/ PHEMA / $(–TiO_2–)_n$, wt%	$W_{max}\times10^2$, min^{-1}	τ_{max}, min	$\tau_{ps,}$ min	α_{ps}	$2R(q)\cdot10^3$, s
OI IPNs -8	0.14	69.96/29.98/0.06	10.30	53	17.0	0.004	3.33
OI IPNs -9	0.14	29.99/69.98/0.03	-	-	16.1	-	4.17
OI IPNs -10	1.40	69.55/29.78/0.67	6.10	64	PS not observed *		
OI IPNs -11	1.40	49.80/49.80/0.40	15.30	44	26.0	0.006	1.22
OI IPNs -12	1.40	29.92/69.80/0.28	22.20	30	20.1	0.009	3.17
OI IPNs -13	2.80	69.08/29.58/1.34	1.10	74	PS not observed *		

* the duration of the experiment for 2 hours

3. RESULTS AND DISCUSSION

Figure 1 shows the dependence of $\ln(I/I_0) = f(\tau)$ for IPNs with 30/70 wt% PU/PHEMA ratio (curve 1) and OI IPNs at the same PU/PHEMA ratio and different $(–TiO_2–)_n$ content in POPG and $Ti(OPr^i)_4/H_2O$ molar ratio (curves 2–5). Similar linear dependencies were obtained for all investigated IPNs for which phase separation was observed. Such linearity, as mentioned earlier, is one of the criteria for the spinodal mechanism of phase separation. From the slope of the plots of the relationship $\ln(I/I_0) = f(\tau)$, the values of $2R(q)$ were calculated. These values, as well as the time of phase separation onset (τ_{ps}) and the degree of HEMA conversion at the time of phase separation onset (α_{ps}) are shown in Tables 1 and 2.

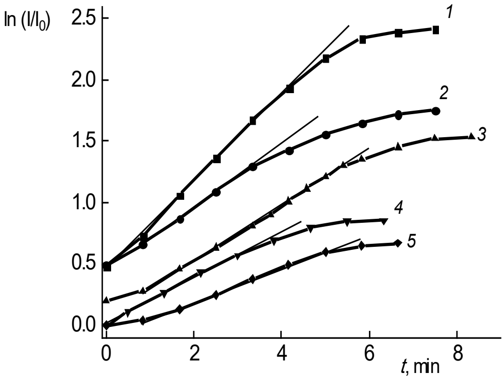

Fig. 1. Time dependence of ln(I/I_0) for the initial IPNs (1) and OI IPNs (2-5) of PU/PHEMA of 30/70 wt% composition with $(–TiO_2–)_n$ content in POPG of 0.14 (2, 3) and 1.40 wt% (4, 5) and $Ti(OPr^i)_4/H_2O$ ratio = 1/2 (2, 4) and 1/1 mol/mol (3, 5).

The data of Tables 1 and 2 show that an increase in PU amount both in the initial IPNs (IPNs -1 and IPNs -2) and in OI IPNs with the same content of $(–TiO_2–)_n$ in POPG and molar ratio $Ti(OPr^i)_4/H_2O$ (OI IPNs - 1, OI IPNs - 2 and OI IPNs - 3; OI IPNs - 8 and OI IPNs - 9; OI IPNs - 11 and OI IPNs - 12) leads to an increase in the initiation time of phase separation and a decrease in its rate. This is due to the fact that the phase separation rate is determined by the rate of chemical reactions. As it follows from Tables 1 and 2, with increasing PU content, the reaction of radical polymerisation of HEMA slows down (the value of W_{max} decreases and the time to reach this maximum increases t_{max}). This is probably due to the fact that increasing the PU content increases the viscosity and crosslinking density of the system as a whole, making it more difficult for AIBN radicals to escape from the "cage". The so-called "cage" effects [21] increase the probability of recombination of initial radicals and reduce the efficiency of initiation, which causes a decrease in the reaction rate of HEMA radical polymerization. Therefore, those values of HEMA monomer conversion (a_{ps}), which are sufficient for loss of compatibility in the reaction system, are reached much later.

The essential factors affecting the phase separation process in OI IPNs are the content and structure of the inorganic component $(–TiO_2–)_n$. From the results shown in Tables 1 and 2, it is evident that for OI IPNs of the same PU/PHEMA composition and $Ti(OPr^i)_4/H_2O$ molar ratio (OI IPNs -3 and OI IPNs -6; OI IPNs -9 and OI IPNs-12), phase separation slows down with increasing $(–TiO_2–)_n$ content. As mentioned above, poly(titanium oxide) catalyses the urethane formation reaction, as a consequence of which the polymerisation of HEMA in OI IPNs takes place in an almost formed cross-linked PU; in this case, donor–acceptor interaction between the C=O group of HEMA and titanium atoms is possible [22]. All this leads to an increase in the viscosity of the system and an enhanced influence of the "cage" effect, which is reflected in a decrease of the initiation efficiency and, as a consequence, a reduced rate of PHEMA formation of OI IPNs component. This, in turn, leads to an increase in the time of the onset of phase separation and a decrease in its rate (Tables 1 and 2). It is worth mentioning that for the OI IPNs with a PU/PHEMA ratio of 70/30 wt. %, $(–TiO_2–)_n$ content of 0.67

and 1.34 wt. % and $Ti(OPr^i)_4/H_2O$ molar ratio 1/1 and 1/2 (OI IPNs -4, OI IPNs -7, OI IPNs -10, OI IPNs -13, Tables 1, 2), as well as for OI IPNs with a PU/PHEMA ratio of 50/50 wt. %, $(–TiO_2–)_n$ content of 0.40 wt. % and a molar ratio of $Ti(OPr^i)_4/H_2O$ 1/1 (OI IPNs -5, Table 1), no change of the light scattering intensity was observed during the experiment (about 2 hours). This indicates the absence of phase separation in such systems, or that the phase separation in OI IPNs starts at higher degrees of component conversion. The significant increase in the compatibility in OI IPNs with such $(–TiO_2–)_n$ content is possible also due to the higher grafting of $(–TiO_2–)_n$ to both components of the IPNs (PU and PGEMA). On the one hand, poly(titanium oxide) can be grafted to POPG during the sol–gel synthesis, and, on the other hand, probably to PHEMA as a result of exchange reaction between residues of non-hydrolysed isopropoxide groups (OPr^i) in $Ti(OPr^i)_4$ with hydroxyl groups of HEMA during the formation of OI IPNs.

It is known [23] that during sol-gel synthesis, depending on the $Ti(OPr^i)_4/H_2O$ ratio, different structures of poly(titanium oxide) can be formed. Thus, when the ratio of $H_2O/Ti(OPr^i)_4 \leq 1$, as a rule, linear poly(titanium oxide) is formed, and when the ratio of $H_2O/Ti(OPr^i)_4 \geq 1$, branched poly(titanium oxide) is obtained. It can be assumed that the structure of the resulting poly(titanium oxide) will also affect the phase separation parameters. Comparing the time of the onset of phase separation and its rate in the OI IPNs with the same PU/PHEMA ratio and the same $(–TiO_2–)_n$ content, but obtained at different molar ratios of $Ti(OPr^i)_4/H_2O$ (OI IPNs -1 and OI IPNs -8; OI IPNs -3 and OI IPNs -9; OI IPNs -6 and OI IPNs -12), it is evident (Tables 1 and 2), that for the OI IPNs where the poly(titanium oxide) is formed at a molar ratio of $Ti(OPr^i)_4/H_2O = 1/1$, the time of the onset of phase separation increases and its rate decreases compared to the OI IPNs where $(–TiO_2–)_n$ formed at $Ti(OPr^i)_4/H_2O = 1/2$. The most likely reason for this effect could be that $(–TiO_2–)_n$ with a linear structure is more bound to POPG and probably has more residues of non-hydrolysed isopropoxy groups (OPr^i) for possible grafting to PHEMA during OI IPNs formation than $(–TiO_2–)_n$ with a branched structure, which in turn may limit the number of such interactions due to the appearance of steric complications.

The results of the study of the phase separation process in the IPNs and OI IPNs are confirmed by optical microscopy data. As an example, microphotographs of IPNs and OI IPNs films with 50/50 wt% PU/PHEMA ratio, different $(–TiO_2–)_n$ content and $Ti(OPr^i)_4/H_2O$ molar ratio are shown in Fig. 2. It follows from Fig. 2 that phase separation in the investigated mixtures occurs by the spinodal mechanism. The initial IPN is characterised by clear interconnected structures (Fig. 2a), which become finer and less distinct for OI IPNs (Figs. 2b, 2c) as a result of a slower phase separation process. The sizes of structural formations in Fig. 2c (1.4 wt% $(–TiO_2–)_n$ in POPG) are slightly smaller than those in Fig. 2b (0.14 wt% $(–TiO_2–)_n$ in POPG). Obviously, the phase separation rate decreases with increasing $(–TiO_2–)_n$ content in POPG, and no phase separation is observed at all when the ratio of $Ti(OPr^i)_4/H_2O$ is changed from 1/2 (Fig. 2c) to 1/1 (Fig. 2d). It should be noted that morphological structures very similar to each other are observed for all phase-separated OI IPNs with different contents of $(–TiO_2–)_n$ and different molar ratios of $Ti(OPr^i)_4/H_2O$.

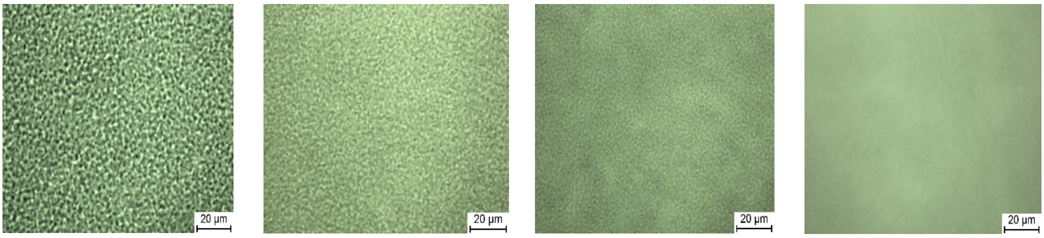

a b c d

Fig. 2. Microphotographs of the initial IPNs (a) and OI IPNs (b-d) with 50/50 wt% PU/PHEMA and $(–TiO_2–)_n$ content in POPG: 0.14 (b); 1.40 wt% (c, d) and $Ti(OPr^i)_4/H_2O$ ratio: 1/2 (b, c), 1/1 mol/mol (d).

4. CONCLUSIONS

The studies have shown that during the formation of both IPNs and OI IPNs, phase separation occurs by the spinodal decomposition mechanism. At the same time, the phase separation rate in OI IPNs depends on the PU/PHEMA ratio, $(–TiO_2–)_n$ content, and its structure. It has been found that the phase separation rate is lower in the formation of OI IPNs than in the initial IPNs with the same component ratio. This process slows down when the amount of $(–TiO_2–)_n$ increases and the molar ratio $Ti(OPr^i)_4/H_2O = 1/1$. At a certain content of $(–TiO_2–)_n$ in OI IPNs, phase separation is not observed at all during the experiment, which indicates a high level of compatibility in such systems. Thus, it is shown that by varying the ratio of IPNs components, the content of the inorganic component and the molar ratio of $Ti(OPr^i)_4/H_2O$ it is possible to control the phase separation process and to obtain OI IPNs with different phase structure.

ACKNOWLEDGEMENTS

The authors are grateful to the Prof., Dr. Chem. Tatiana Alekseeva, Dr. Chem. Taisa Ignatova and Researcher Liubov Vorontsova from the Institute of Macromolecular Chemistry of the National Academy of Sciences of Ukraine for their help in developing the article.

REFERENCES

1. Sperling, L.H. (2012). *Interpenetrating Polymer Networks and Related Materials*. Springer Science & Business Media: Cham, Switzerland.
2. Lipatov, Yu. (2001). *Phase-Separated Interpenetrating Polymer Networks*. USChTU: Dnepropetrovsk.
3. Lipatov, Yu.S., & Nesterov, A.E. (1997). *Thermodynamics of Polymer Blend*s. Lancaster–Basel: Techn. Publ. Co.
4. Lipatov, Y. S. (2006). Phase Separation in Filled Polymer Blends. *Journal of Macromolecular Science, Part B*, *45*(5), 871–888. DOI: 10.1080/15583720600824615

5. Balcerski, W., Ryu, S.Y., & Hoffmann, M. R. (2007). Visible-Light Photoactivity of Nitrogen-Doped TiO_2: Photooxidation of HCO_2H to CO_2 and H_2O. *J. Phys. Chem. C., 111*, 15357–15362. https://doi.org/10.1021/jp074989o
6. Lin, Y. P., Bocharov, D., Isakoviča, I., Pankratov, V., Popov, A. A., Popov, A. I., & Piskunov, S. (2023). Chlorine Adsorption on TiO_2 (110)/Water Interface: Nonadiabatic Molecular Dynamics Simulations for Photocatalytic Water Splitting. *Electronic Materials*, *4* (1), 33-48. https://doi.org/10.3390/electronicmat4010004
7. Kamalov, R., Vokhmintsev, A., Dorosheva, I., Kravets, N., & Weinstein, I. (2016). Synthesis of Composite Based on Carbon Nanotubes and Anodic Titania. *Advanced Science Letters*, *22*(3), 688-690. DOI: 10.1166/asl.2016.6997
8. Dorosheva, I. B., Adiyak, E. V., Valeeva, A. A., & Rempel, A. A. (2019). Synthesis of Nonstoichiometric Titanium Dioxide in the Hydrogen Flow. *AIP Conference Proceedings*, *2174*, 020019. https://doi.org/10.1063/1.5134170
9. Serga, V., Burve, R., Krumina, A., Pankratova, V., Popov, A. I., & Pankratov, V. (2021). Study of Phase Composition, Photocatalytic Activity, and Photoluminescence of TiO_2 with Eu Additive Produced by the Extraction-Pyrolytic Method. *Journal of Materials Research and Technology*, *13*, 2350–2360. https://doi.org/10.1016/j.jmrt.2021.06.029
10. Serga, V., Burve, R., Krumina, A., Romanova, M., Kotomin, E. A., & Popov, A. I. (2021). Extraction–Pyrolytic Method for TiO_2 Polymorphs Production. *Crystals*, *11* (4), 431. https://doi.org/10.3390/cryst11040431
11. Vuoriluoto, M., Hokkanen, A., Mäkelä, T., Harlin, A., & Orelma, H. (2022). Optical Properties of an Organic-Inorganic Hybrid Film Made of Regenerated Cellulose Doped with Light-Scattering TiO_2 Particles. *Optical Materials*, *123*, 111882. https://doi.org/10.1016/j.optmat.2021.111882
12. Heiba, Z. K., El-naggar, A. M., Kamal, A. M., Abd-Elkader, O. H., & Mohamed, M. B. (2023). Optical and Dielectric Properties of PVC/TiO_2/TBAI Ionic Liquid Polymer Electrolyte. *Optical Materials*, *139*, 113764. DOI: 10.1016/j.optmat.2023.113764
13. Compeán-González, C. L., Thomas, A. G., Syres, K. L., Cole, J., & Li, Z. (2022). 4-Mercaptobenzoic Acid Adsorption on TiO_2 Anatase (101) and TiO_2 Rutile (110) Surfaces. *Surfaces*, *5* (2), 238–250. https://doi.org/10.3390/surfaces5020017
14. Anandhi, P., Harikrishnan, S., Senthil Kumar, V. J., Lai, W. C., & Mahmoud, A. E. D. (2022). The Enhanced Energy Density of rGO/TiO_2 Based Nanocomposite as Electrode Material for Supercapacitor. *Electronics*, *11* (11), 1792. https://doi.org/10.3390/electronics11111792
15. Tsebriienko, T., & Popov, A.I. (2021). Effect of Poly (Titanium Oxide) on the Viscoelastic and Thermophysical Properties of Interpenetrating Polymer Networks. *Crystals, 11*, 794. https://doi.org/10.3390/cryst11070794
16. Brinker, C.J., & Scherer, G.W. (1990). *Sol-Gel Science*. New York: Academic Press.
17. Fadeeva, E., Koch, J., Chichkov, B., Kuznetsov, A., Kameneva, O., Bityurin, N., … & Kanaev, A. (2006). Laser Imprinting of 3D Structures in Gel-Based Titanium Oxide Organic-Inorganic Hybrids. *Applied Physics A*, *84* (1), 27–30. https://doi.org/10.1007/s00339-006-3577-1
18. Salomatina, E. V., Bityurin, N. M., Gulenova, M. V., Gracheva, T. A., Drozdov, M. N., Knyazev, A. V., … & Smirnova, L. A. (2013). Synthesis, Structure, and Properties of Organic–Inorganic Nanocomposites Containing Poly (Titanium Oxide). *Journal of Materials Chemistry C*, *1* (39), 6375–6385. https://doi.org/10.1007/s00339-006-3577-1
19. van Aartsen, J.J., & Smolders, C.A. (1970). Light Scattering of Polymer Solutions during Liquid-Liquid Phase Separation. *Eur. Polym. J.*, *6* (8), 1105–1112.
20. Cahn, J.W. (1965). Phase Separation by Spinodal Decomposition in Isotropic System. *J. Chem. Phys.*, *42* (1), 93–99.

21. Korolev, G. V., & Mogilevich, M. M. (2009). *Three-Dimensional Free-Radical Polymerization*. Berlin, Heidelberg: Springer-Verlag. DOI: 10.1007/978-3-540-87567-3
22. Pomogailo, A. D. (2006). Synthesis and Intercalation Chemistry of Hybrid Organo-Inorganic Nanocomposites. *Polymer Science Series C*, *48* (1), 85–111. DOI: 10.1134/S181123820601005X
23. Feld, R., & Cowe P.L. (1965). *The Organic Chemistry of Titanium*. London: Butterworths.

sciendo

LATVIAN JOURNAL OF PHYSICS
AND TECHNICAL SCIENCES
2024, N 3

DOI: 10.2478/lpts-2024-0017

FOCUSED POLARIZATION GRATINGS IN AN AZOBENZENE-BASED MOLECULAR GLASSY FILM

A. Ozols[*], P. Augustovs, K. Balodis, K. Ozols

Riga Technical University,
Faculty of Materials Science and Applied Chemistry,
3/7 Paula Valdena Str., Riga, LV-1048, LATVIA
[*]e-mail: andris.ozols@rtu.lv

Holograms recorded by focused light beams have several advantages over usual plane wave holograms such as reduced size, white light readout possibility and others. Focused polarization grating recording in an azobenzene-based molecular glasy film 5,5,5-triphenylpentyl 4-((4-(2-(4-bis(2-hydroxyethyl)amino)phenyl)-1-cyanovinyl)phenyl)dyazenyl)benzoate (which we shortly denoted as B11) is experimentally studied and compared with such grating recording in other materials. It has been determined that focusing manifests itself differently than in other materials, e.g., as in a-As_2S_3 and a-As-S-Se chalcogenide films. Thus, it reduces the holographic grating recording efficiency independently of recording and readout beam polarizations. It has also been found that recording efficiency with circularly and orthogonally *L-R* polarized beams is higher than with linearly polarized *p-p* beams. The highest diffraction eficiency of 26% is achieved with *L-R* polarized unfocused beams.

Recording efficiency grating period dependences for unfocused beams at 200 J/cm^2 exposure and at 1000 J/cm^2 exposure are different with a maxima at 2 µm and 6 µm, respectively. In contrast, recording efficiency grating period dependences for focused beams at 200 J/cm^2 exposure and at 1000 J/cm^2 exposure are the same with the maximum at 6 µm.

The obtained results are discussed in terms of *trans-cis-trans* photoisomerization followed by mass transfer and their light intensity dependence, light electric field gradient force, the photoinduced light scattering and photoelastic forces.

***Keywords**: Azobenzene-based molecular glassy films, electric gradient force, holographic polarization gratings, light focusing, recording efficiency, photoelastic force, photoisomerization.*

1. INTRODUCTION

Holograms recorded by focused light beams (focused holograms, image plane holograms) have some properties that make them useful. First, their reduced size is a straightforward way to increase the information density of holographic recording. Holographic versatile discs already have higher capacity than other optical discs (CD, DVD, Blu Ray) [1]. Second, they can be read out with extended broad spectrum light sources, including white light sources [2]. Third, they are used when exposure time is limited and high enough laser light intensities are needed [3]. Fourth, they present a convenient method to convert 3D data to 2D form in computer holography [4].

However, the reduction of hologram size, generally speaking, changes its properties. Among them, diffraction efficiency (DE) and spatial frequency response are of primary importance. The physical processes of focused hologram recording are relatively unexplored. To the authors' knowledge, there are four theoretical papers [5]–[8] devoted to this problem and three experimental ones [3], [9], [10]. In the mentioned experimental papers, only scalar elementary holograms (scalar holographic gratings) have been studied. This paper deals with vector holographic gratings (polarization gratings) when not only recording light intensity but also (and mainly) the spatial distribution of light electric field inside the material is important.

The goal of this paper is to study the properties of holographic grating (HG) recording in an azobenzene film depending on their diameter, grating period, recording beam polarizations and exposure. Previously we have investigated scalar HG recorded with *s-s* polarized beams in amorphous As-S-Se and As_2S_3 chalcogenide films [9], [10]. Here we investigate unfocused and focused polarization HG in azobenzene-based molecular glassy film B11, compare properties between them and with previous results in amorphous chalcogenide films. We conclude that focusing HG in B11 film leads to results different from those in amorphous chalcogenide films, and that polarizations of recording beams do not play a qualitatively important role.

2. EXPERIMENTS AND RESULTS

For our experiments, the sample of the azobenzene-based molecular glassy film was synthesized. The chemical name of the film was 5,5,5-triphenylpentyl4-((4-(2-(4-bis(2-hydroxyethyl)amino)phenyl)-1-cyanovinyl)phenyl)dyazenyl)benzoate which we shortly denoted as B11. Its structural formula is given in Fig. 1. Actually, this name refers to one chromophore molecule of which the film consists. These chromophore molecules are kept together by weak Van der Waals forces.

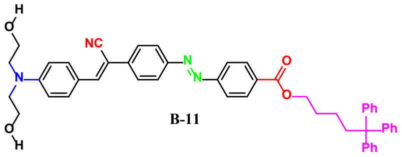

Fig. 1. Structural formula of the studied sample B11. This is an azobenzene molecular glassy film with the thickness d = 1.6 µm put on the glass substrate. Its glass transition temperature is 77 °C. Donor-acceptor push-pull type azochromophore molecule consists of two phenyl rings connected by an azobond –N=N-. Donor is an amino group (blue with N on the left). The main acceptor is carboxylgroup –COO- (red on the right), auxiliary acceptor group is cyano group NC (red on the left).

The absorption spectrum of the sample is presented in Fig. 2.

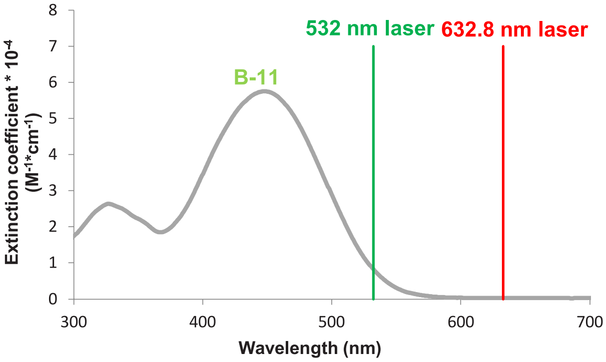

Fig. 2. Absorption spectrum of the B11 film and the laser lines used for holographic grating recording (532 nm) and readout (632.8 nm).

HG recording was carried out by a green Cobolt Samba 60 mW laser at 532 nm but HG readout was performed by a red Melles Griot 35 mW laser at 632.8 nm. HG periods were Λ = 2μm, Λ = 6 μm and Λ = 10.8 μm for unfocused recording beams, and Λ = 2 μm, Λ = 6 μm and Λ = 10 μm for focused recording beams. The 1/e^2 diameters of all beams were measured by a moving screen method (Fig. 3).

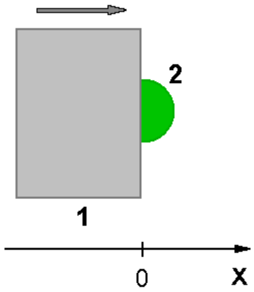

Fig. 3. Moving screen method for laser diameter measurements. 1 – the screen which was gradually moved to the right along the *x*-axis shutting the incident laser beam. 2 – The movement of the screen was started from the position $x = 0$, which corresponded to the half of the transmitted beam power, i.e., to the power ratio $P/P_0 = 0.5$ where *P* was the transmitted beam power, P_0 was the incident beam power. The ratio P/P_0 as the function of *x* was measured.

The calculation for the Gaussian light intensity distribution gives the following theoretical expression for this ratio:

$$\frac{P}{P_0} = 0.5\left[1 - \mathrm{erf}\left(\frac{2\sqrt{2}}{d_0}x\right)\right], \tag{1}$$

where d_0 is the 1/e^2 beam diameter. In our experiments, the power ratio of 0.0142 was technically optimal when small enough beam diameters with the accuracy of 1μm could be measured with our photodetector. Then it follows from Eq. (1) that

$$d_0 = 1.825x. \tag{2}$$

In the case of unfocused beam HG recording, we measured the recording beam diameter $d_0(1)$ = (1.174 ± 0.007) mm and the readout beam diameter $d_0(2)$ = (1.770 ± 0.021) mm. In the case of focused beam recording when the readout beam was focused as well, we measured $d_0(1)$= (0.139 ± 0.011) mm and $d_0(2)$= (0.104 ± 0.021) mm. Light intensity was defined as $I = P/(\pi d_0^2/4)$, where *P* is a beam power. This intensity corresponds to the centre of Gaussian laser beam.

The holographic recording and readout setup schematics for unfocused and focused beam cases are presented in Figs. 4 and 5, respectively. HG recording was carried out by two equal power ($P_1=P_2$) laser beams whose total intensities $I = (P_1 + P_2)/(\pi d_0^2/4)$ were I = 0.92 W/cm^2 and I= 4.93 W/cm^2, respectively. The recording and readout beam polarization were either linear *p-p-p* or circular *L-R-L*. HG were predominantly scalar in linear polarization case, and predominantly vectorial in circular polarization case. Generally speaking, both types of HG were polarization gratings.

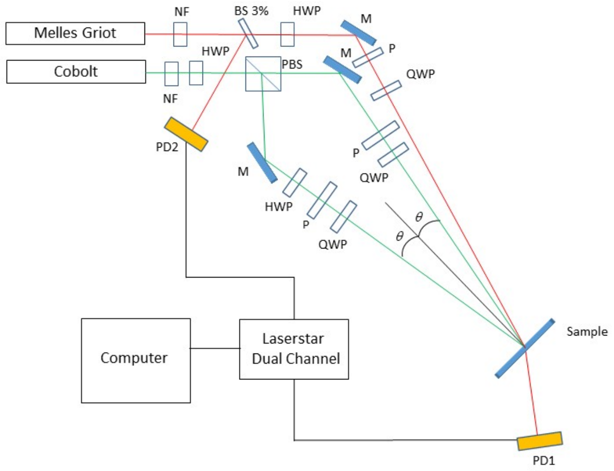

Fig. 4. Holographic recording and readout setup schematic by unfocused laser beams. Notations: NF – neutral density filter, BS 3 % – beam splitter with 3 % reflection coefficient, HWP – half-wave plate, QWP – quarter-wave plate, M – mirror, P – polarizer, PBS – polarization beam splitter, PD1 and PD2 – photodiodes, Laserstar Dual Channel – Ophir Laserstar Dual Channel power meter. Beam formation elements were adjusted for linearly polarized *p-p* beams or circularly polarized *L-R* beams. In the above schematic, the HG recording was performed with *L-* and *R*-polarized beams, readout with *L*-polarized beam.

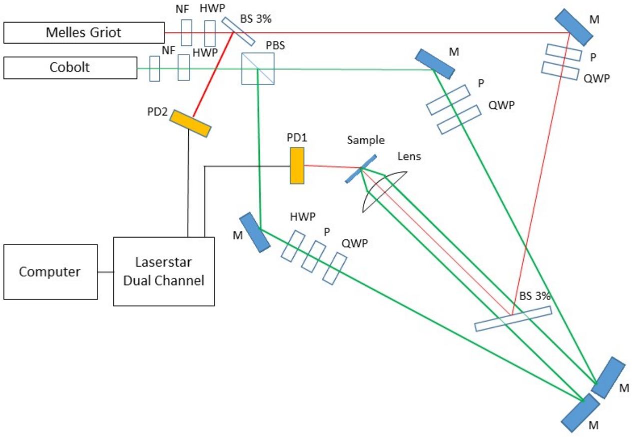

Fig. 5. Holographic recording and readout setup schematic by focused laser beams. Notations: NF – neutral density filter, BS 3 % – beam splitter with 3 % reflection coefficient, HWP – half-wave plate, QWP – quarter-wave plate, M – mirror, PBS – polarization beam splitter, P – polarizer, PD1 and PD2 – photodiodes, Laserstar Dual Channel – Ophir Laserstar Dual Channel power meter. Beam formation elements were adjusted for linearly polarized *p-p* beams or circularly polarized *L-R* beams. In the above schematic, the HG recording was performed with *L-* and *R*-polarized beams, readout with *L*-polarized beam.

Experimental results are presented in Figs. 6–9 and Tables 1–4. The main HG parameter which was measured was diffraction efficiency DE = $[P_d/P_i]$ (%), where P_d was the first-order diffracted beam power and P_i was the readot beam power. DE exposure time dependences for unfocused and focused HG recording at Λ = 6 μm in the case of recording with linearly *p-p* polarized laser beams, and in the case of circularly and orthogonally *L-R* polarized beams are shown in Figs. 6–9. Qualitatively the same DE exposure time dependences were also observed for other HG periods mentioned above. We chose Λ = 6 μm case for the illustration of DE exposure time dependences because the most efficient recording took place at this period.

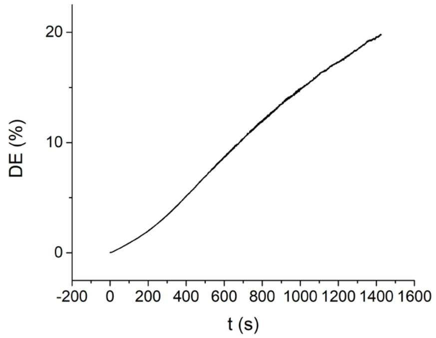

Fig. 6. Diffraction efficiency exposure time dependence for unfocused *p-p* polarized 532 nm laser beams at Λ=6 μm. Readout with *p*-polarized 632.8 nm beam.

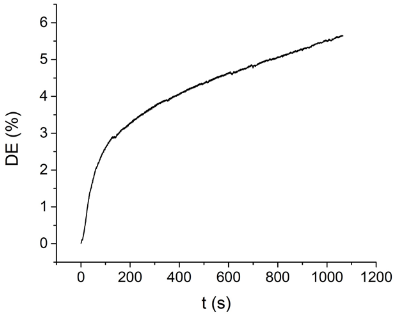

Fig. 7. Diffraction efficiency exposure time dependence for focused *p-p* polarized 532 nm laser beams at Λ=6 μm. Readout with focused *p*-polarized 632.8 nm beam.

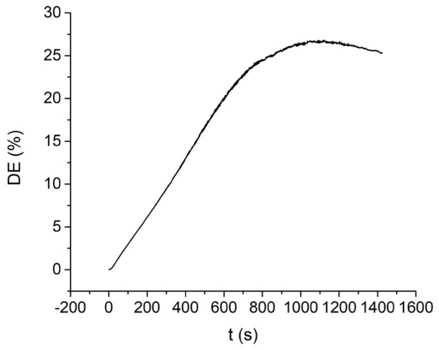

Fig. 8. Diffraction efficiency exposure time dependence for unfocused *L-R* polarized 532 nm laser beams at Λ=6 μm. Readout with *L*-polarized 632.8 nm beam.

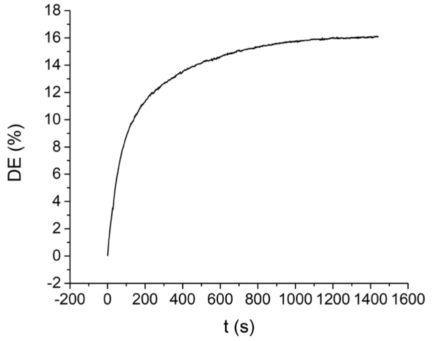

Fig. 9. Diffraction efficiency exposure time dependence for focused *L-R* polarized 532 nm laser beams at Λ=6 μm. Readout with focused *L*-polarized 632.8 nm beam.

Comparison of Figs. 6 and 7 clearly shows that recording with focused laser beams is substantially less efficient, i.e., DE is lower for fixed exposure.

In Figs. 8 and 9, unfocused and focused HG recording DE exposure time dependences are shown in the case of orthogonal circular *L-R* recording beam polarizations.

A comparison of Figs. 8 and 9 shows again that recording with focused laser beams is substantially less efficient also for circularly polarized beams. Thus, focusing reduces the HG recording efficiency independently of beam polarizations. Another conclusion from Figs. 6–9 is that recording with circularly *L-R* polarized beams is more efficient than with linearly *p-p* polarized beams. The same two conclusions are also valid for other HG periods.

An overview of holographic recording parameters for fixed exposures (*It*) 200 J/cm^2 and 1000J/cm^2 and for all studied HG periods is given in Tables 1–4. To characterise HG recording efficiency more precisely, apart from DE defined above, we also determined specific recording energy, $W=It/\mathrm{DE}$ (J/cm^2) and recording efficiency factor, $\mathrm{REF}=\mathrm{DE}/W$ (cm^2%/J) describing both aspects of DE and material sensitivity. Data in each position of Tables 1–4 correspond to the average values of three measurements to minimise the effect of B11 sample nonuniformity. The maximum relative error does not exceed 10 % for DE and *W*, and 14 % for REF in the case of unfocused beam recording. In the case of focused beam recording, maximum relative errors do not exceed 22 %, 27 % and 35 %, respectively.

As recording and readout beam diameters, $d_0(1)$ and $d_0(2)$, were different, it was necessary to normalize them to equal recording and readout beam parameter case $d_0(1)= d_0(2)$. This was done according to the formula derived in the paper [11]:

$$\mathrm{DE}[d_0(2)=d_0(1))]= (1/3)[1+2d_0(2)^2/d_0(1)^2\,]\ \mathrm{DE}[d_0(2)\neq d_0(1)]\ . \tag{3}$$

Table 1. HG Parameters in the Case of Unfocused Recording at 200 J/cm^2 Exposure

Beam polarizations	Λ, μm	DE, %	W, J/cm^2%	REF, (%cm)^2/J
p-p	2	2.9	68	0.043
L-R	2	7.2	28	0.26
p-p	6	2.6	79	0.033
L-R	6	6.9	29	0.24
p-p	10.8	2.6	77	0.034
L-R	10.8	5.8	35	0.17

Table 2. HG Parameters in the Case of Focused Recording at 200 J/cm^2 Exposure

Beam polarizations	Λ, μm	DE, %	W, J/cm^2%	REF, (%cm)^2/J
p-p	2	0.33	620	0.00053
L-R	2	1.5	130	0.012
p-p	6	3.9	50	0.074
L-R	6	4.3	50	0.094
p-p	10	1.7	120	0.015
L-R	10	2.7	80	0.037

Table 3. HG Parameters in the Case of Unfocused Recording at 100 J/cm^2 Exposure

Beam polarizations	Λ, μm	DE, %	W, J/cm^2%	REF, (%cm)^2/J
p-p	2	15	67	0.22
L-R	2	18	55	0.33
p-p	6	16	63	0.25
L-R	6	26	38	0.69
p-p	10.8	16	63	0.25
L-R	10.8	22	45	0.48

Table 4. HG Parameters in the Case of Focused Recording at 100 J/cm^2 Exposure

Beam polarizations	Λ, µm	DE, %	W, J/cm^2%	REF, (%cm)^2/J
p-p	2	2.4	410	0.0059
L-R	2	4.9	210	0.024
p-p	6	4.5	220	0.021
L-R	6	10	100	0.10
p-p	10	3.2	300	0.011
L-R	10	6.1	170	0.039

The following conclusions can be made by inspecting Tables 1–4.

1. Recording efficiency is higher with unfocused beams than with focused ones. Most easily it can be seen by comparing REF values, which take into account both DE and specific recording energy.
2. Recording efficiency with circularly and orthogonally *L-R* polarized beams is higher than with linearly polarized *p-p* beams. The highest DE=26 % is achieved with *L-R* polarized unfocused beams.
3. Recording efficiency Λ-dependences for *unfocused* beams at 200 J/cm^2 exposure and at 1000 J/cm^2 exposure were *different* with maxima at 2 µm and 6µm, respectively.
4. Recording efficiency Λ-dependences for *focused* beams at 200 J/cm^2 exposure and at 1000 J/cm^2 exposure were *the same* with the maximum at 6µm.

The first two conclusions followed also from Figs. 6–9 in the case of Λ=6 µm. Further we discuss the obtained experimental results.

3. DISCUSSION

Let us consider the first conclusion that unfocused beam HG recording in B11 film is more efficient than unfocused recording. In principle, the recording of HG by spherical waves (as in the case of focused beam recording) is less efficient than by plane waves. It is experimentally proven that maximum DE of HG recorded by spherical waves is smaller by approximately 30 % than maximum DE of HG recorded by plane waves [9]. The main physical reason is the nonuniform spatial frequency response of the recording material. However, in our case the real difference is much higher, and we believe that this is due to the recording efficiency intensity dependence in B11 films. Thus, in a-As$_2$S$_3$ films at 632.8 nm we have found that focused beam recording is much more efficient than unfocused recording because of strong light intensity dependence of photostructural changes governing HG inscription [10]. At lesser extent, it is also valid in the case of a-As-S-Se films [9]. Evidently, the light intensity dependence is opposite in B11 films.

HG recording mechanism in B11 film based on literature data [12]–[14] and our observations consisted of four steps.

i. Charge transfer takes place over the aromatic core bridge from donors to acceptors under the influence of 532 nm recording light. As the result, the chromophore molecules which initially were in the *trans* state turn to the *cis* state and reorient perpendicularly to the electric vector of light because of photoinduced quantum transitions.

ii. Further t*rans-cis-trans* photoisomerization cycles takes place according to the spatial polarization modulation of recording light leading to the inscription of volume birefringence grating (VBG).

iii. VBG creates also spatially modulated photoisomerization pressure, which together with electric gradient force results in mass transfer forming surface relief grating (SRG) and/or volume density grating (VDG).

iv. At first, VBG is recorded, and it decays during the readout. The following SRG and VDG grow slower but are stable. There are only SRG and VDG at saturation.

VBG have been recorded much faster than SRG and VDG. Photoinduced birefringence takes place in few seconds whereas relief forms in few hundreds of seconds [14]. Evidently, the lower recording efficiency by focused beams is mainly the result of photoisomerization intensity dependence. As shown by Aleksejeva et al. [14], in the case of B8 films, SRG relief modulation amplitude for intensities higher than 0.4 W/cm^2 decreases, and this decrease is very fast for intensities higher than 1 W/cm^2. The authors explain this phenomenon by too large photosoftening making film unstable. It is highly probable that in B11 films at I=4.93 W/cm^2 photosoftening takes place along with recording, thus decreasing the focused recording efficiency.

The second conclusion about higher recording efficiency with circularly polarized *L-R* beams is more efficient than by linearly polarized *p-p* beams can be explained by the fact that circularly polarized light addresses more chromophores than linearly polarized light already at the stage of VBG [13]. Further, in the case of SRG recording, photoisomerization pressure created by a larger free volume of *cis* form leads to more efficient mass transfer when recorded by *L-R* polarizations compared to *p-p* polarizations [13]. Our atomic force microscope measurements of HG in B11 films have shown that SRG are dominating at large enough exposures reaching relative thickness changes as high as $\Delta d/d$ = 1.0 µm/1.6 µm = 0.625.

The third conclusion about different optimal recording HG periods for unfocused recording at 200 J/cm^2 exposure and at 1000 J/cm^2 exposure (2 µm and 6 µm, respectively) needs more detailed consideration. There are, at least, three factors affecting HG recording efficiency Λ- dependence in azobenzene-based glassy molecular films such as our B11.

First, the most general factor, active in any recording medium, is the spatial resolution of the recording medium, which depends on its atomic structure (size and distribution evenness of photoactive sites), and on the macroscopic inhomogeneities in the bulk and on the surface [15]. Typical spatial resolution of the best silver halide photographic emulsions is expressed by a quantity g= 0.2 µm [15]. This is the minimal image element size, which can be recorded in the emulsion and seen after the emulsion development and is equal to the silver grain size. The resolution of amorphous chalcogenide a-As_2S_3 films is better: $g \leq$ 0.1 µm [15]. The spatial resolution (pixel size) of electronic image capturing devices such as CCD and CMOS is g > 1 µm. The size of azobenzene chromophore molecule (Fig. 1) is about 3 nm [12]. However, the best spatial resolution of azobenzene-based molecular glassy films is about 0.18 µm as shown by our reflection HG recording experiments. This is because photoactive site includes many chromophore molecules taking part in *trans-cis-trans* photoisomerization and mass transfer and because of Rayleigh light scattering by spatial inhomogeneities. Light scattering smears the interference field inside the medium, and its influence is the highest for small HG periods. In principle, HG recording is possible only if the condition $\Lambda \geq 2g$ holds. Practically, much stronger condition $\Lambda >> g$ must be fulfilled. If the light scattering increases during the HG recording then spatial resolution decreases, and the HG period corresponding to the most efficient recording should increase. This is what one can observe when exposure is increased from 200 J/cm^2 to 1000 J/cm^2 (Tables 1 and 3). We have experimentally observed the increase in light scattering during the exposure. This scattering increase is due to the noise grating recording by scattered light waves and recording waves. Thus, we conjecture that effective grain size is increasing (Fig. 10) shifting the optimum HG period from 2 μm to 6 μm.

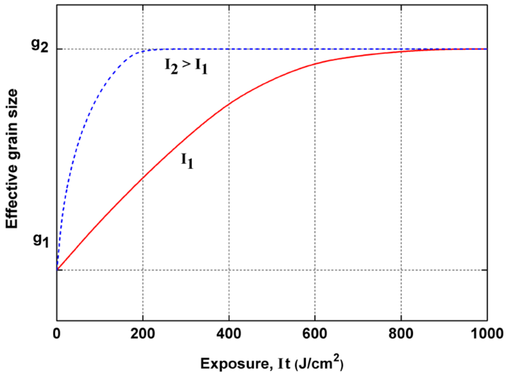

Fig. 10. Effective grain size dependence on exposure and recording light intensity proposed to explain the observed HG recording efficiency Λ- dependences. g_1 is the initial effective grain size and g_2 is the final efective grain size after the 1000 J/cm^2 exposure. Curves correspond to unfocused recording with light intensity I_1 and to focused recording with light intensity I_2.

Second, the very mechanism of mass transfer due to the light electric field gradient force leads to the certain Λ- dependence. The time-averaged electric gradient force density is [13]:

$$\boldsymbol{f} = <(\boldsymbol{P}\nabla)\boldsymbol{E}> , \tag{4}$$

where $\boldsymbol{P}=\chi\boldsymbol{E}$ is the material polarization, χ is the material dielectric susceptibility, $\boldsymbol{E}$ is the light electric field, which harmonically depends on the coordinate along the interference field wave vector (parallel to the sample surface and perpendicular to the bisector between recording beams (see Figs. 4 and 5). Then from Eq. (4) it can be shown both in the cases of *p-p* and *L-R* recording beam polarizations that electric gradient force f is proportional to $1/\Lambda$. Thus, also the surface relief HG recording efficiency is proportional to $1/\Lambda$. This fact explains the recording efficiency decrease at $\Lambda > 2$ μm in the case of unfocused recording at 200 J/cm^2 exposure (Table 1), and at $\Lambda > 6$ μm in the case of unfocused recording at 1000 J/cm^2 exposure (Table 3).

Third, for exposures $It > 200$ J/cm^2 the deformation of the sample surface becomes significant and the surface elastic forces start to counteract the mass transfer. This corresponds to the necessary increase of surface energy density given by the Gibbs-Helmholtz equation:

$$w_s = \sigma - \partial\sigma/\partial T, \tag{5}$$

where σ is the surface tension, T is absolute temperature [16]. On the other hand, the amplitude of the photoinduced changes of surface tension, $\Delta\sigma$, is directly proportional to sample thickness and inversely proportional to HG period, i.e., $\Delta\sigma \sim d/\Lambda$ [17]. Together with the light scattering this fact facilitates the optimal HG recording period shift from 2 μm to 6 μm when exposure is increased from 200 J/cm^2 to 1000 J/cm^2. The interplay between electric gradient force and elastic force determines the maximal DE values.

The fourth conclusion was that recording efficiency Λ-dependences for focused beams at 200 J/cm^2 exposure and at 1000 J/

cm^2 exposure were the same with the maximum at 6μm. The situation is analogous to the unfocused light beam recording at 1000 J/cm^2 . This can be explained by much higher recording light intensity leading to much higher recording speed. Much more *trans-cis-trans* cycles take place per unit of time with much faster mass transfer and SRG recording. We suppose that already after 200 J/cm^2 exposure the same effective grain size g_2 is reached as in the case of unfocused recording after 1000 J/cm^2 exposure (Fig. 10), and photoinduced scattering shifts the recording efficiency maximum to Λ = 6 μm. This is also stimulated by photoinduced elastic forces, which are inversely proportional to HG period as indicated above.

4. CONCLUSIONS

1. Effect of laser beam focusing on polarization holographic grating (HG) properties is experimentally studied in azobenzene-based molecular glassy 5,5,5-triphenylpentyl 4-((4-(2-(4-bis(2-hydroxyethyl)amino)phenyl)-1-cyanovinyl)phenyl)dyazenyl)benzoate film, which we shortly have denoted as B11 film. This effect in B11 film manifests itself differently than in other materials, e.g., as in a-As_2S_3 and a-As-S-Se chalcogenide films.
2. Focusing reduces the HG recording efficiency independently of recording and readout beam polarizations. The main reason is the recording efficiency intensity dependence of surface relief gratings decreasing at high enough intensities due to the photoinduced softening of the B11 film.
3. Recording efficiency with circularly and orthogonally *L-R* polarized beams is higher than with linearly polarized *p-p* beams. The highest diffraction eficiency of 26 % is achieved with *L-R* polarized unfocused beams. This is due to the fact that circularly polarized light addresses more chromophores than linearly polarized light and that at the stage of surface relief grating recording photoisomerization pressure created by a larger free volume of *cis* form leads to more efficient mass transfer when recorded by *L-R* polarizations compared to *p-p* polarizations.
4. Recording efficiency grating period dependences for unfocused beams at 200 J/cm^2 exposure and at 1000 J/cm^2 exposure are different with maxima at 2 μm and 6 μm, respectively. Recording efficiency is maximal at 200 J/cm^2 because then it is mainly determined by electric gradient force inversely proportional to HG period. At 1000 J/cm^2 the phtoinduced increase of light Rayleigh scattering as well as the photoinduced decrease of photoelastic forces counteracting the HG recording lead to the optimal HG period shift from 2 μm to 6 μm.
5. Recording efficiency grating period dependences for focused beams at 200 J/cm^2 exposure and at 1000 J/cm^2 exposure are the same with the maximum at 6 μm. This difference compared to unfocused beam recording case can be explained by much higher recording light intensity resulting in almost immediate optimal HG period shift from 2 μm to 6 μm due to the photoinduced light scattering and photoelastic forces.

REFERENCES

1. Deepika, G. (2011). Holographic versatile disc. In *2011 National Conference on Innovations in Emerging Technology (pp. 145–146).* Erode, India: IEEE. DOI: 10.1109/NCOIET.2011.5738819.
2. Collier, R.J., Burckhardt, C.B., & Lin, L.H. (1971). *Optical Holography.* New York and London: Academic Press.
3. Kalkum, F., Peithmann, K., & Buse, K. (2009). Dynamics of Holographic Recording with Focused Beams in Iron-Doped Lithium Niobate Crystals. *Optics Express, 17* (3), 1321–1329. DOI: 10.1364/OE.17.001321
4. Hendler, L., & Freedland, S. S.(1986). Image Plane Holography for Holographic Presentation of a Three-Dimensional Data Base. *Comp. & Math. With Appls 12A* (6), 777–784.
5. Schönnagel, G. (1975). Recording and Readout of Volume Holograms in Diffraction-Limited Systems. *Kvant. Elektronika 2* (8), 1622–1628 (in Russian).
6. Siegman, A.E. (1977). Bragg Diffraction of a Gaussian Beam by a Crossed-Gaussian Volume Grating. *J.Opt.Soc.Am 67* (4), 545–550.
7. Moharam, M.G., Gaylord, T.K., & Magnusson, R. (1980). Diffraction Characteristics of Three-Dimensional Crossed-Beam Volume Gratings. *J.Opt. Soc.Am. 70* (4), 437–442.
8. Yakimovich, A.P. (1983). Diffraction Efficiency of Volume Phase Microholograms. *Opt. Spektrosk. 55* (3), 490–494 (in Russian).
9. Ozols, A., Ivanovs, Ģ., & Ļaudobelis, M. (1997). Microhologram Recording in Amorphous Semiconductor Films. *Proc. SPIE 2967,* 276–279.
10. Ozols, A., Saharovs, Dm., & Reinfelde, M. (2006). Holographic Recording in Amorphous As_2S_3 Films at 633 nm. *Journ. of Non-Crystalline Solids 352,* 2652–2656.
11. Ozols, A.O., & Schwartz, K.K. (1982). Photosensitivity Criteria of Media and Optimization of Hologram Recording. *Kvant. Elektronika 9* (12), 2441–2448. (in Russian).
12. Sekkat, Z., & Knoll, W. (2002). *Photoreactive Organic Thin Films.* Orlando, FL: Elsevier Science.
13. Zhao, Y, & Ikeda, T. (2009). *Smart Light-Responsive Materials.* Hoboken, New Jersey: Wiley.
14. Aleksejeva, J., Teteris, J., & Tokmakovs, A. (2013). Azobenzene-Containing Low Molecular Weight Organic Glasses for Optical Recording. *Physics Procedia, 44,* 19–24.
15. Schwartz, K. (1993). *The Physics of Optical Recording.* Berlin: Springer Verlag.
16. Prokhorov, M.A. (ed.) (1992). *Physical Encyclopedia* (vol. 3), *646.* Moscow: Bolshaja Rossiiskaja enciklopedija (in Russian).
17. Jastrzebski, Z.D. (1987). *The Nature and Properties of Engineering Materials.* New York: Wiley.

LATVIAN JOURNAL OF PHYSICS
AND TECHNICAL SCIENCES
2024, N 3

DOI: 10.2478/lpts-2024-0018

ASSESSMENT OF VARIOUS FACTORS AFFECTING ECONOMIC INDICATORS IN PROSUMER AND CONSUMER ENERGY COMMUNITIES: A CASE STUDY OF LATVIA

R. Lazdins*, A. Mutule

Institute of Power Engineering,
Riga Technical University
12/1 Azenes Str., Riga, LV-1048, LATVIA
*e-mail: Roberts.Lazdins@rtu.lv

This study explores the recent legislative changes allowing prosumers and consumers in Latvia to form energy communities (EnCs). In spite of legal advancements, the absence of supporting regulations and potential barriers, such as the lack of tailored support schemes and forecasting tools, pose challenges. International experiences highlight additional hurdles, including weak stakeholder dialogue and limited EnC modelling tools. To address these issues, the study proposes a prosumer and consumer EnC business model aligned with Latvia's legislation, emphasising a peer-to-peer (P2P) trading approach. The model incorporates state aid, electricity trader responsibilities, and reinvestment of EnC profits, eliminating the need for a dedicated trading platform. The study introduces a user-friendly planning tool in MS Excel, evaluating economic viability through case studies and scenarios. Findings emphasise the optimisation of EnC effectiveness by adjusting tariffs, minimising initial investment costs, securing external funding, and managing loan durations. The planning tool serves as a universal instrument, offering insights into individual EnC economic indicators based on their unique characteristics. The research provides valuable guidance to stakeholders and policymakers in Latvia's evolving energy landscape.

Keywords: *Energy community, peer-to-peer, case study, modelling.*

1. INTRODUCTION

Due to the legislative change made to the Latvia's Electricity Market Law [1] and the Energy Law [2], electricity active consumers, also known as prosumers, and consumers are one step closer to soon being allowed to create the first EnCs in Latvia. In spite of the legal changes made, it is necessary to develop Cabinet of Ministers Regulations related to the conditions and procedures for sharing electricity, the process for information exchange between market participants and system operators, criteria for the EnC territorial borders and other relevant factors [1], [2].

In spite of the lack of legislation, the EnC implementation and acceptance may also face other implementation barriers, which are already identified in Latvia: lack of support schemes designed specifically for EnCs [3], lack of tools which would forecast economic benefits from the creation of EnCs [4], [5], concerns about the economic impact of the introduction of a single electricity trader for all members of one EnC [1], a small number of existing prosumers [6], [7] and limited amount of shareable electricity [8], [9], as well as EnC-related information and awareness [3], [10].

Other countries have revealed additional barriers that may emerge in Latvia, which based on their experiences can slow down the implementation of EnCs. A comprehensive review [11] identified that a weak dialogue between stakeholders and information dissemination activities does not actualise the benefits of creating EnC, thus creating insufficient interest in participating in them. Moreover, lack of user-friendly and open-access EnC modelling and planning tools makes it difficult for prosumers and consumers to identify economic benefits from the participation in the EnCs, and high complexity of existing business models creates non-transparency of EnC operations, which in turn discourages participation in energy sharing activities [11].

Given the diverse renewable energy and EnC related legislations [12], electricity tariff structures and settlement schemes [13] across the European Union countries, it is not feasible to establish a uniform structure and operational mechanism for EnCs that can be universally applied across countries.

In order for Latvia's electricity consumers to provide an opportunity to overcome the above-mentioned barriers and challenges, which are based on concerns about the economic efficiency of EnC and the availability of related information to a wider part of society, it is necessary to inform the public about the advantages of EnC implementation and the potential structure of it. Moreover, a relatively small number of prosumers in Latvia and the limitation that a prosumer must self-consume at least 80 % of the electricity generated [9] indicate the high potential of prosumer and consumer EnC implementation in Latvia [14], [15].

The choice of the EnC operating scheme is important, thus ensuring the sustainability and viability of the EnC. Studies conducted in [16], [17] determined that it would be advisable to use a P2P energy trading approach, which is also recommended by Latvia's Energy and Climate Plan (NECP) [18]. In addition, this approach can be supplemented with the provisions of the Latvia's Electricity Market Law [1] and Energy Law [2]:

- Members of the EnC can apply for the state aid to partially cover the purchase costs of the system;
- Electricity trader is responsible for accounting of both shared and sold electricity, as well as management of payment mechanisms;

- The profit obtained by the EnC is not distributed or paid out in dividends, but it is invested to achieve the goals set in the EnC statutes (such as for the implementation of measures to increase energy efficiency).

This suggests that the P2P approach can be strengthened by obtaining external funding, such as state aid, and by dispensing with the necessity for a dedicated P2P electricity trading platform, which would be utilised by the existing electricity trader services. Moreover, the primary purpose of the accumulated funds would extend beyond covering EnC costs, including operational expenditures (OPEX) or loan repayments. Instead, the intention is to leverage these saved funds to enhance energy efficiency or implement other welfare measures for the EnC members.

Considering all the above, the following prosumer and consumer EnC business model, compatible with Latvia's existing legislation, can be proposed (see Fig. 1).

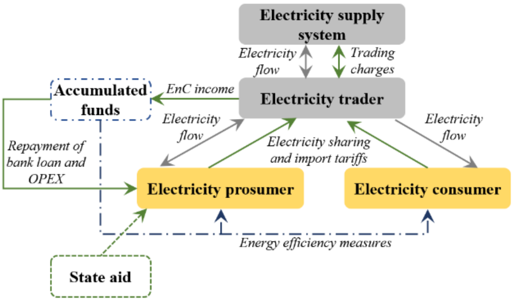

Fig. 1. The proposed business model for prosumer and consumer EnC.

To use the proposed business model, as well as to evaluate the potential and efficiency of its implementation, it is necessary to develop a specifically designed tool to plan sharing-related activities according to each participant's electricity consumption. Moreover, determination of initial investment distributions, as well as the value of the electricity sharing tariff would allow planning EnC in such a way that electricity sharing would not only remunerate cost of the installed electricity generation source, but also generate economic benefits for each EnC member.

Referring to [14], [15], the development of the aforementioned planning tool could effectively tackle the previously mentioned barriers and challenges related to information availability. The necessity and application of the planning tool can be related not only to the modelling of electricity sharing and payment mechanisms, but also to provide recommendations to potential members and other stakeholders about the effects of various factors (generation and consumption level, electricity sharing, import and purchase tariffs, cost allocations and other) on the specifically defined EnC indicators. In addition, ensuring the open-access and user-friendly environment of this planning tool plays an equally important role, thus allowing it to be used with basic programming skills and without the use of specific coding languages, platforms and applications.

While bearing in mind all above, the study aims to present in detail the prosumer and consumer EnC planning tool designed in a freely accessible and user-friendly environment (MS Excel) under Latvia's existing EnC-related legislation, EnC operational guidelines and restrictions. With the help of the developed case studies and scenarios, the study aims to offer recommendations to potential EnC creators, participants and other stakeholders. Moreover, the task is to assess the effect of various factors on the proposed EnC economic viability, as well as economic benefits of the participation in the proposed electricity sharing activities.

The study is structured as follows: Section 2 presents EnC-related legislation guidelines and restrictions, as well as operation and calculations within EnC planning tool. Assumptions of the used data are determined, and case study and scenario modelling is performed in Section 3. Section 4 provides an analysis of the modelled scenarios and draws conclusions about the effect of the considered factors on the defined indicators and viability of the EnC.

2. AN OVERVIEW OF THE PROSUMER AND CONSUMER ENC PLANNING TOOL

2.1. Legislation Guidelines

Taking into account that the main task of the proposed planning tool is to evaluate the operation of the EnCs in Latvia, it must comply with the assumptions and restrictions set by Latvia's legislation.

The Electricity Market Law has determined the following guidelines:

- EnC members are prosumers and consumers;
- Electricity sharing and sales activities must be done using one distribution system operator. Furthermore, EnC cannot manage distribution grid autonomously;
- Electricity trader is responsible for accounting of both shared and sold electricity, as well as management of payment mechanisms;
- Members of EnCs conclude a sharing agreement with each other and also conclude an agreement with the electricity trader on sharing-related obligations;
- Prosumers' generated electricity must be shared with other members of EnC and the excess amount must be sold to the electricity trader at the agreed price;
- Parties involved in electricity sharing cannot participate in net metering system, net settlement system and system of certificates of origin of electricity;
- EnC members cannot participate in several EnC at the same time.

In addition to the aforementioned, amendments to the Electricity Market Law have introduced a new definition of an active user (prosumer): active user – an end-user who produces electricity for his/her own or his/her EnCs needs and can transfer the surplus of electricity produced, which is no more than 20 % of the electricity produced by the user in a 12-month period, to an electricity trader within the net settlement system, sell it, engage in flexibility services or energy efficiency schemes [9].

State aid cannot be applied for without achieving 80 % self-consumption by prosumers, leading to a reduction in costs associated with the purchase of RES-based electricity generation source. Moreover, state aid does not include the purchase of battery energy storage systems [8]. However, a thoroughly cited study [19] has established that when prosumers' self-consumption level surpasses 75 %, there is no economic justification for the acquisition and utilisation of batteries. Based on the decelerated limitations of the EnC operation, the next subsection will be devoted to a detailed review of the steps included in the proposed planning tool with the help of mathematical formulations.

2.2. An Overview of Planning Tool Mathematical Formulations

To determine the EnC electricity production, it is, first, necessary to calculate the hourly amount of electricity produced by the prosumer:

$$P_{RES}^{t} = P_{RES\ cap.} * \delta_{RES}^{t} * \Delta_{\%}^{y}, \tag{1}$$

where $P_{RES\ cap.}$ – the total capacity of the installed RES-based electricity source (kW), δ_{RES}^{t} – hourly coefficients, which determine the amount of electricity hourly generated from 1 kW of installed capacity (kWh/kW), $\Delta_{\%}^{y}$ – annual installed RES-based electricity source degradation coefficient (%).

Prosumers' hourly consumed amount of electricity from their own electricity generation source can be determined as follows:

$$P_{RES\rightarrow Pros.}^{t} = \begin{cases} P_{RES}^{t}, \text{if } P_{RES}^{t} < W_{Pros.}^{t} \\ W_{Pros.}^{t}, \text{if } P_{RES}^{t} \geq W_{Pros.}^{t} \end{cases}, \tag{2}$$

where $W_{Pros.}^{t}$ – prosumers' hourly electricity consumption (kWh).

To determine prosumers' amount of electricity consumed from the grid, the following calculations can be made:

$$P_{grid\rightarrow Pros.}^{t} = \begin{cases} W_{Pros.}^{t} - P_{RES\rightarrow Pros.}^{t}, \text{if } \mathrm{P}_{\mathrm{RES}}^{\mathrm{t}} < \mathrm{W}_{\mathrm{Pros.}}^{\mathrm{t}} \\ 0, \text{if } \mathrm{P}_{\mathrm{RES}}^{\mathrm{t}} \geq \mathrm{W}_{\mathrm{Pros.}}^{\mathrm{t}} \end{cases} \tag{3}$$

Hourly amount of surplus electricity after prosumers' self-consumption, which would be available for sharing with the consumer, can be defined as follows:

$$P_{RES,excess}^{t} = \begin{cases} 0, \text{if } \mathrm{P}_{\mathrm{RES}}^{\mathrm{t}} < \mathrm{W}_{\mathrm{Pros.}}^{\mathrm{t}} \\ P_{RES}^{t} - P_{RES\rightarrow Pros.}^{t}, \text{if } \mathrm{P}_{\mathrm{RES}}^{\mathrm{t}} \geq \mathrm{W}_{\mathrm{Pros.}}^{\mathrm{t}} \end{cases} \tag{4}$$

In the instance when the prosumer would like to pay for the received electricity from their own electricity source, the tariff must encompass the value added tax (VAT):

$$c_{Pros.\ EnC+VAT}^{t} = c_{Pros.\ EnC}^{t} * (1 + VAT), \tag{5}$$

where $c_{Pros.\ EnC}^{t}$ – prosumer's tariff for the received electricity from their own generation source without VAT (EUR/kWh).

Prosumer's hourly payments for the amount of electricity received by its own electricity source can be calculated as follows:

$$C_{EnC\rightarrow Pros.}^{t} = P_{RES\rightarrow Pros.}^{t} * c_{Pros.\ EnC+VAT}^{t}. \tag{6}$$

Prosumer's hourly electricity tariff component for the amount of electricity received from grid with VAT can be determined as follows:

$$c_{Pros.\ grid+VAT}^{t} = c_{Pros.\ grid}^{t} * (1 + VAT), \tag{7}$$

where $c_{Pros.\ grid}^{t}$ – prosumers' electricity component tariff for the received electricity from the grid without VAT (EUR/kWh).

Thereby, prosumer's hourly payments for the amount of electricity received from the grid (without other distribution grid components) is calculated as follows:

$$C_{grid\rightarrow Pros.}^{t} = P_{grid\rightarrow Pros.}^{t} * c_{Pros.\ grid+VAT}^{t}. \tag{8}$$

Annual overall electricity costs (including other grid cost components) for the prosumer, when they participate in the EnC, can be written as follows:

$$C^{y}_{Pros.with\ EnC+VAT} = \Sigma C^{t}_{EnC\rightarrow Pros.} + \Sigma C^{t}_{grid\rightarrow Pros.} + (\Sigma P^{t}_{grid\rightarrow Pros.} * c_{supply\ (grid).Pros.} + I_{conn.Pros.} * \ c_{maintenance\ (grid).Pros.} * 12) \ , * (1+VAT) \tag{9}$$

where $c_{supply\ (grid).Pros.}$ – prosumer's tariff for the supply of electricity from the grid without VAT (EUR/kWh), $I_{conn.Pros.}$ – maximum rated current of prosumer's connection (A), $c_{maintenance\ (grid).Pros.}$ – prosumer's costs for connection maintenance without VAT (EUR/A/month).

Prosumer's total electricity costs without participating in the EnC can be calculated as follows:

$$C^{y}_{Pros.without\ EnC+VAT} = \Sigma C^{t}_{grid\rightarrow Pros.} + (\Sigma P^{t}_{grid\rightarrow Pros.} * c_{supply\ (grid).Pros.} + I_{conn.Pros.} * \ c_{maintenance\ (grid).Pros.} * 12) *. (1+VAT) \tag{10}$$

Consumer's hourly consumed amount of electricity from prosumer's electricity source can be defined as follows:

$$P^{t}_{RES,excess\rightarrow Cons.} = \begin{cases} P^{t}_{RES,excess}, \text{if } \mathrm{P}^{\mathrm{t}}_{\mathrm{RES,excess}} < \mathrm{W}^{\mathrm{t}}_{\mathrm{Cons.}} \\ W^{t}_{Cons.}, \text{if } \mathrm{P}^{\mathrm{t}}_{\mathrm{RES,excess}} \geq \mathrm{W}^{\mathrm{t}}_{\mathrm{Cons.}} \end{cases}, \tag{11}$$

where $W^{t}_{Cons.}$ – consumer's hourly electricity consumption (kWh).

Consumer's hourly amount of electricity imported from the grid can written as follows:

$$P^{t}_{grid\rightarrow Cons.} = \begin{cases} W^{t}_{Cons.} - P^{t}_{RES,excess\rightarrow Cons.}, \text{if } \mathrm{P}^{\mathrm{t}}_{\mathrm{RES,excess}} < \mathrm{W}^{\mathrm{t}}_{\mathrm{Cons.}} \\ 0, \text{if } \mathrm{P}^{\mathrm{t}}_{\mathrm{RES,excess}} \geq \mathrm{W}^{\mathrm{t}}_{\mathrm{Cons.}} \end{cases} \tag{12}$$

To determine hourly amount of electricity sold to the electricity trader, the following calculation is used:

$$P^{t}_{excess\rightarrow trader} = \begin{cases} 0, \text{if } \mathrm{P}^{\mathrm{t}}_{\mathrm{RES,excess}} < \mathrm{W}^{\mathrm{t}}_{\mathrm{Cons.}} \\ P^{t}_{RES,excess} - P^{t}_{RES,excess\rightarrow Cons.}, \text{if } \mathrm{P}^{\mathrm{t}}_{\mathrm{RES,excess}} \geq \mathrm{W}^{\mathrm{t}}_{\mathrm{Cons.}} \end{cases} \tag{13}$$

Electricity tariff for received electricity from the prosumer should include VAT:

$$c^t_{Cons.\ EnC+VAT} = c^t_{Cons.\ EnC} * (1 + VAT), \tag{14}$$

where $c^t_{Cons.\ EnC}$ – electricity tariff for received electricity from the prosumer without VAT (EUR/kWh).

The hourly costs for consumer for receiving electricity from the prosumer (including VAT) are calculated as follows:

$$C^t_{EnC \to Cons.\ (with\, VAT)} = P^t_{RES \to Cons.} * c^t_{Cons.\ EnC+VAT}. \tag{15}$$

Thereby, annual costs for consumer for receiving electricity from the prosumer (including VAT) are determined as follows:

$$C^y_{EnC \to Cons.\ (with\, VAT)} = \Sigma C^t_{EnC \to Cons.\ (with\, VAT)}. \tag{16}$$

Consumer's hourly costs for the received amount of electricity from the prosumer (excluding VAT) can be written as follows:

$$C^t_{EnC \to Cons.\ (without\ VAT)} = P^t_{RES \to Cons.} * c^t_{Cons.\ EnC}. \tag{17}$$

Consumer's annual costs for the received amount of electricity from the prosumer (excluding VAT) can be expressed as follows:

$$C^y_{EnC \to Cons.\ (without\ VAT)} = \Sigma C^t_{EnC \to Cons.\ (without\ VAT)}. \tag{18}$$

Consumer's electricity component tariff for imported electricity from the grid with VAT can be determined as follows:

$$c^t_{Cons.\ grid+VAT} = c^t_{Cons.\ grid} * (1 + VAT), \tag{19}$$

where $c^t_{Cons.\ grid}$ – consumer's electricity component tariff for imported electricity from the grid without VAT (EUR/kWh);

Consumer's hourly payments for the imported electricity from the grid with VAT (excluding other distribution grid tariff components) can be calculated as follows:

$$C^t_{grid \to Cons.} = P^t_{grid \to Cons.} * c^t_{Cons.\ grid+VAT}. \tag{20}$$

Consumer's annual costs (with VAT) for the amount of consumed electricity by participating in the EnC including other grid costs components can be determined as follows:

$$C^{y}_{Cons.with\,EnC+VAT} = C^{y}_{EnC\rightarrow Cons.\ (with\,VAT)} + \Sigma C^{t}_{grid\rightarrow Cons.} + (W^{t}_{Cons.} * c_{supply\ (grid).Cons.} + I_{conn.Cons.} * c_{maintenance\ (grid).Cons.} * 12) * (1 + VAT), \tag{21}$$

where $c_{supply\ (grid).Cons.}$ – consumer's tariff for the supply of electricity from the grid without VAT (EUR/kWh), $I_{conn.Cons.}$ – maximum rated current of consumer's connection (A), $c_{maintenance\ (grid).Cons.}$ – consumer's costs for connection maintenance without VAT (EUR/A/month).

Similar to the aforementioned formula, consumer's annual electricity costs without participating in the EnC can be expressed as follows:

$$C^{y}_{Cons.without\,EnC+VAT} = \Sigma W^{t}_{Cons.} * c^{t}_{Cons.\ grid+VAT} + (\Sigma W^{t}_{Cons.} * c_{supply\ (grid).Cons.} + I_{conn.Cons.} * c_{maintenance\ (grid).Cons.} * 12) * (1 + VAT). \tag{22}$$

Capital expenditure (CAPEX) for the purchase of electricity generation source can be covered by three funding sources: external funding (such as state aid), investment contributions by the prosumer and/or consumer, as well as bank loan. In order to calculate one-time investment contributions by the prosumer and consumer, the following formula can be used:

$$I_0 = I_{0,Pros.} + I_{0,Cons.}, \tag{23}$$

where $I_{0,Pros.}$ – prosumer's one-time payment for the coverage of initial investments (EUR), $I_{0,Cons.}$ – consumer's one-time payment for the coverage of initial investments (EUR).

Total CAPEX (including VAT) can be determined as follows:

$$CAPEX = \left(C_{CAPEX\ per\ kW} * P_{PV\ cap.}\right) * (1 + VAT) - C_{grants}, \tag{24}$$

where $C_{CAPEX\ per\ kW}$ – CAPEX related to an installed generation source capacity of 1 kW without VAT (EUR), C_{grants} – the amount of external funding (state aid) (EUR).

Required amount of bank loan to fully cover CAPEX can be calculated as follows:

$$C_{bank\rightarrow EnC} = \begin{cases} 0, \text{if } \mathrm{I}_0 \geq \mathrm{CAPEX} \\ CAPEX - I_0, \text{if } \mathrm{I}_0 < \mathrm{CAPEX} \end{cases}. \tag{25}$$

To calculate the amount of annual bank loan repayment, the following formula is used:

$$C_{EnC\rightarrow bank}^{y}=\begin{cases} C_{bank\rightarrow EnC} * \left(1+i_{\%,bank}\right) * \\ \dfrac{i_{\%,bank} * \left(1+i_{\%,bank}\right)^{y_{loan}}}{\left(\left(1+i_{\%,bank}\right)^{y_{loan}}\right)-1}, \text{when y} \leq \text{ y}_{\text{loan}}, \\ 0, \text{when y} > \text{ y}_{\text{loan}} \end{cases} \tag{26}$$

where y_{loan} – loan duration (years); $i_{\%,bank}$ – loan interest rate (%).

Annual operational costs (including VAT) for electricity generation source can be written as follows:

$$OPEX^{y}=(C_{OPEX\ per\ kW}^{y} * P_{RES\ cap.}) * (1+VAT), \tag{27}$$

where $C_{OPEX\ per\ kW}^{y}$ – annual operational costs related to an installed generation source capacity of 1 kW without VAT (EUR).

To calculate EnC received hourly income from the electricity sold to the electricity trader, the following formula is used:

$$C_{excess\rightarrow trader}^{t}=P_{excess\rightarrow trader}^{t} * c_{excess\rightarrow trader}^{t}, \tag{28}$$

where $c_{excess\rightarrow trader}^{t}$ – electricity traders' purchase price without taxes (EUR).

Prosumer's annual overall electricity costs if they do not own the electricity generation source can be determined using the following formula:

$$\begin{gathered} C_{el.Pros.\rightarrow trader.without\ RES}^{y}=\Sigma(W_{Pros.}^{t} * c_{Pros.\ grid+VAT}^{t})+ \\ (\Sigma W_{Pros.}^{t} * c_{supply\ (grid).Pros.} \qquad . \\ +I_{conn.Pros.} * \ c_{maintenance\ (grid).Pros.} * 12) * (1+VAT) \end{gathered} \tag{29}$$

Prosumer's annual cost savings regarding reduction of amount of imported electricity from the grid due to the self-consumption of power generated by the installed generation source can be calculated as follows:

$$\begin{gathered} \Delta C_{pros\rightarrow grid\ (with.without\ RES)}^{y}=\Sigma C_{grid\rightarrow Pros.}^{t}+(\Sigma P_{grid\rightarrow Pros.}^{t} * c_{supply\ (grid).Pros.} \\ +I_{conn.Pros.} * \ c_{maintenance\ (grid).Pros.} * 12) \\ * (1+VAT)-C_{el.Pros.\rightarrow trader.without\ RES}^{y} \end{gathered} \tag{30}$$

The annual overall incoming cash flow of the EnC can be determined as follows:

$$Income^{y}_{EnC,RES} = C^{y}_{EnC \rightarrow Cons.\ (without\ VAT)} + \Sigma(P^{t}_{RES \rightarrow Pros.} * c^{t}_{Pros.\ EnC}) + \Delta C^{y}_{pros \rightarrow grid\ (with.without\ RES)} + \Sigma C^{t}_{excess \rightarrow trader} \quad (31)$$

The annual expenses or outcoming cash flow of the EnC is calculated as follows:

$$Expenses^{y}_{EnC,RES} = OPEX^{y} + C^{y}_{EnC \rightarrow bank}. \quad (32)$$

Thereby, annual net cash flow is determined:

$$R^{y}_{EnC,RES} = Income^{y}_{EnC,RES} - Expenses^{y}_{EnC,RES}. \quad (33)$$

Annual net present value for the electricity generation source is calculated as follows:

$$NPV^{y} = -I_{0,Pros.} + \sum_{i=1}^{y} \frac{R^{y}_{EnC,RES}}{\left(1 + i_{\%,d}\right)^{y}}, \quad (34)$$

where $i_{\%,d}$ – discount rate (%).

The annual income for prosumer from the sale of electricity to the electricity trader, assuming non-participation in the EnC (excluding taxes), can be expressed as follows:

$$C^{y}_{Pros \rightarrow trader,without\ EnC} = \Sigma(P^{t}_{RES,excess} * c^{t}_{excess \rightarrow trader}). \quad (35)$$

Prosumer’s annual economic benefits from the participation in the EnC is calculated as follows:

$$EB^{y}_{Pros.} = I_{0,Cons.} + \sum_{i=1}^{y} (-\Sigma C^{t}_{EnC \rightarrow Pros.} + C^{y}_{EnC \rightarrow Cons.\ (without\ VAT)} + \Sigma C^{t}_{excess \rightarrow trader} - C^{y}_{Pros \rightarrow trader,without\ EnC}) \quad (36)$$

Similar to the aforementioned formula, consumer’s economic benefits from the participation in the EnC are calculated as follows:

$$EB^{y}_{Cons.} = -I_{0,Cons.} + \sum_{i=1}^{y} (\ C^{y}_{Cons.without\ EnC+VAT} - C^{y}_{Cons.with\ EnC+VAT}) \quad (37)$$

EnC direct incoming cash flow is credited into accumulated funds, which can help cover the annual costs associated with bank loan repayments and OPEX, as well as making savings for future energy efficiency measures for EnC members. Thereby, annual amount of cash located in EnCs accumulated funds after coverage of annual bank loan payment and OPEX will be zero, if:

$$AF_{EnC}^{y} = \begin{array}{c}(C_{EnC\rightarrow bank}^{y} + OPEX^{y}) \geq (C_{EnC\rightarrow Cons.\ (without\,VAT)}^{y} + \\ \Sigma(P_{RES\rightarrow Pros.}^{t} * c_{Pros.\ EnC}^{t}) + \Sigma C_{excess\rightarrow trader}^{t})\end{array} \tag{38}$$

If the previous formula does not hold, then:

$$AF_{EnC}^{y} = C_{EnC\rightarrow Cons.\ (without\,VAT)}^{y} + \Sigma(P_{RES\rightarrow Pros.}^{t} * c_{Pros.\ EnC}^{t}) + \Sigma C_{excess\rightarrow trader}^{t} - (C_{EnC\rightarrow bank}^{y} + OPEX^{y})) \tag{39}$$

Total amount of cash in EnCs accumulated funds in a specific year can be calculated as:

$$\Sigma AF_{EnC}^{y} = \sum\nolimits_{i=1}^{y} AF_{EnC}^{y}. \tag{40}$$

Finally, to make sure that prosumer's self-consumption level is within the allowed limits, the aforementioned level is calculated as:

$$SC_{Pros.,\%}^{y} = \frac{\Sigma P_{RES\rightarrow Pros.}^{t}}{\Sigma P_{RES}^{t}} * 100\%. \tag{41}$$

In order to demonstrate the developed planning tool in action and determine inclusive tariffs, CAPEX, loan duration, state aid and initial investment coverage scheme effect on indicators characterising the economic efficiency of the EnC, the upcoming paragraph delves into modelling selected EnCs, starting with assumptions included in the modelling process.

3. CASE STUDIES AND SCENARIO MODELLING

3.1. Assumptions

The subsequent case studies and scenarios incorporate the following assumptions:

- To determine prosumers' and consumers' electricity consumption schedule, the 2023 load profile for households [20] was used and it was equated to the monthly average electricity consumption for the year [21];
- Photovoltaics (PV) are used as the prosumer electricity generation source. Hourly coefficients which determine the amount of electricity hourly generated from 1 kW of installed capacity are determined using [22];
- For the creation of the proposed EnC and ensuring its operation, the amount of state aid is allocated, which corresponds to the amount mentioned in [8];
- When modelling electricity tariffs, fixed tariffs are used, as only 15 % of Latvia's electricity consumers in 2023 settle with Nord pool market price [23];
- To calculate the CAPEX associated with an installed generation source capacity of 1 kW (excluding VAT), reference [23] is utilised. This involves selecting PV panel suppliers with the lowest, highest, and average prices on the market.

- Electricity traders' price for the purchase of excess amount of electricity from the EnC is chosen freely due to the fact that electricity traders have the right to offer an individually concluded contract to the prosumer and EnC [1]. In addition, the greatest importance of this price may lie not in its value, but in the value of the relationship between it and the tariff for which the prosumer will share the generated electricity to the consumer.
- As it is assumed that a prosumer is the owner of electricity generation source, it does not make payments for the amount of electricity received from the PV panels.

Taking into account the used modelling assumptions, the following chapter provides the basic data of the three EnCs used, as well as a detailed description of the modelled case studies and scenarios.

3.2. EnCs, Case Studies and Scenarios

The primary objective of modelling is to assess the impact of various selected factors on the NPV, economic benefits for prosumer and consumer participating in the EnC, as well as the accumulation of funds. In order to expand the application of the modelled scenario data to different prosumer and consumer generation and consumption values, three EnCs will be used for modelling (see Table 1).

Table 1. Basic Data of the Modelled EnCs

Data	EnC No1	EnC No2	EnC No3
Installed capacity of PV panels	3 kW	3 kW	4 kW
PV degradation coefficient [15]	0,5%/year		
Prosumers' average monthly electricity consumption	780 kWh	780 kWh	1050 kWh
Consumers' average monthly electricity consumption	175 kWh	300 kWh	175 kWh
Amount of external funding (state aid) [8]	1800 EUR	1800 EUR	2200 EUR
Data applicable to all modelled EnCs (without taxes): Prosumers' annual self-consumption level (80 %) [8], [9]; Consumers' tariff for received electricity from the prosumer: 0.16 EUR/kWh; Electricity traders' price for the purchase of electricity from the EnC: 0.14 EUR/kWh; Electricity tariff component for the purchase of electricity from the grid: 0.18 EUR/kWh; CAPEX related to installed generation source capacity of 1 kW: 958 EUR/kW [24]; Prosumers' and consumers' connection to the grid: 3-phases, 20A [25]; Distribution grid tariff for the supply of electricity: 0.03985 EUR/kWh [25]; Distribution grid tariff for connection maintenance: 0.92 EUR/A/month [25]; Annual OPEX: 1.2 % of PV system costs [15]; Loan duration: 5 years; Interest rate: 5.9 % [26]; Discount rate: 9.96 % [27]; Prosumers' initial investments: 50 % of total CAPEX; Consumers' initial investments: 0 % of total CAPEX; VAT: 21 % [28].			

In order to analyse an inclusive factor effect on NPV, economic benefits from the participation in the EnC and accumulated funds after 20 years of EnC operation, Table 2 displays the formulated case studies along with scenarios illustrating the increase and decrease in the different variables.

Table 2. Modelled Case Studies (CS) and Scenarios (SC)

CS	Description	Base	SC 1	SC 2	SC 3	SC 4	SC 5
1	Consumers' tariff for received electricity from the prosumer (EUR/kWh)	0.16	0.16	0.16	0.16	0.18	0.20
	Electricity traders' price for the purchase of electricity from the EnC (EUR/kWh)	0.14	0.09	0.16	0.18	0.14	0.14
2	Electricity tariff component for the purchase of electricity from the grid (EUR/kWh)	0.18	0.16	0.20			
3	CAPEX related to installed generation source capacity of 1 kW (EUR/kW)	958	641	1427			
4	Loan duration (years)	5	3	7			
5	Amount of external funding (such as state aid) (EUR)	1800 2200	1500 1900	2100 2500			
6	Prosumers' initial investments (% of CAPEX)	50	100	0	50	50	
	Consumers' initial investments (% of CAPEX)	0	0	0	5	50	

Subsequent subsection provides the results of modelling the studied EnC base data and related case studies and scenarios to determine NPV, accumulated funds, prosumers' and consumers' economic benefits from the participation in the EnC.

3.3. Results

Given that the aim of the conducted case studies and scenarios is to determine the effect of the specified factor value on predefined indicators, the next subsections will delve into the values of each indicator corresponding to each Case Study (1–6) and related scenarios. Moreover, values of EnC indicators are reflected at the end of 20-year period, thus reflecting their value at the end of the lifetime of the PV panels.

3.3.1. Net Present Value

The graphic representation of the NPV (the data are reflected for the 20th year) obtained by the planning tool is given in Fig. 2.

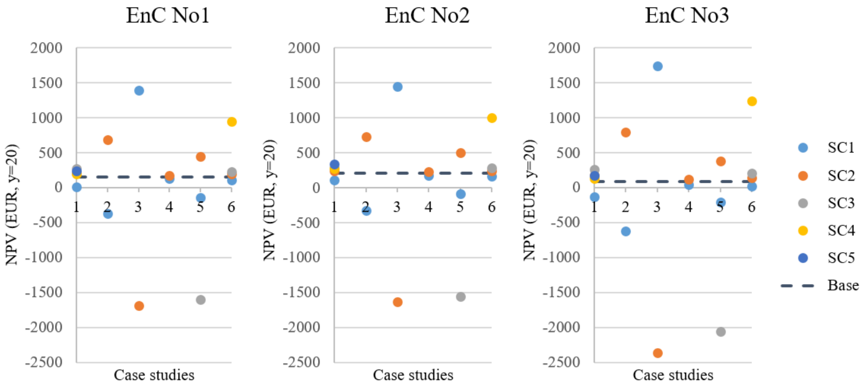

Fig. 2. NPV values under used EnCs, case studies and scenarios (SCs).

The acquired data reveal that among the used baseline EnCs, EnC No 2 yields the highest NPV. Comparing NPV data between EnC No 2 and No 1, it is evident that under baseline conditions, when the electricity traders' purchase price for the excess electricity is lower than the tariff at which the prosumer shares produced electricity with the consumer, an uptick in the consumer's electricity consumption results in a greater amount of electricity available for sharing between the prosumer and consumer, thereby increasing the EnC income. In contrast, comparing NPV data between EnC No 2 and No 3 indicates a decrease in the shared amount of electricity between the prosumer and consumer, leading to a reduction in the EnC income. In spite of the increase of external funding (state aid), the installation of higher-capacity PV panels not only raises the costs associated with covering the prosumer's initial investment but also amplifies the bank loan amount necessary to fully cover CAPEX. Furthermore, the PV panel capacity contributes to a rise in annual OPEX, leading to an increase in an outgoing cash flow and a subsequent reduction in NPV value. Considering the aforementioned factors, prosumer must ensure that, with an increased PV panel installed capacity, consumers' electricity consumption (and, consequently, the shared amount of electricity with the consumer) is sufficiently high to offset the overall expense increment.

By modelling the scenarios included in Case Study 1, it can be observed that as the considered tariff and price increase, the corresponding increase of income from both the prosumer's shared electricity to the consumer and from the sold electricity to the electricity trader can be observed, leading to an overall rise in NPV in all baseline EnCs. If after covering the prosumer's self-consumption most of the electricity is transferred to the consumer, the value of the sharing tariff is more important for the provision of income (as well as NPV) than the traders' electricity purchase price. Thus, it can be concluded that consumers' electricity consumption level can be decisive in determining the impact on NPV with the ratio between sharing tariff and the electricity trader price for purchase of surplus electricity.

Considering that the prosumer's savings from the reduced amount of electricity imports due to the self-consumption of electricity produced by PV panels are also taken into account for determining the NPV, findings from Case Study 2 suggest that the level of savings can decline when the tariff for imported electricity is lower, and, conversely, it can increase when the tariff for imported electricity is higher. Therefore, the NPV of PV panels in the EnC is not only affected by factors within the EnC itself, but it is also significantly impacted by the prevailing conditions in the electricity market.

One of the main factors affecting NPV is initial cost of PV panels. The results of Case Study 3 clearly indicate that the cost of PV panels per installed kW can result in both strongly positive and negative NPV values, thus indicating that its value has a greater effect on NPV than sharing, selling and import tariffs and prices. Thereby, it is highly recommended to choose the most economically advantageous PV panel dealer and installer in order to achieve both the planned payback period and to avoid the forced increase in the sharing tariff, which could partially compensate for the negative NPV, at the same time also causing doubts for the consumer about its potential economic benefits from the participation in the EnC.

Scenario simulation results in Case Study 4 indicate that the duration of the bank loan has a minimal effect on the NPV value, but a slight increase in its value is observed in SC2 when the repayment period of the bank loan is longer. In spite of the additional interest rate-related costs each year, the value of money decreases faster than the interest rate payment increases over the considered period.

Taking into account that external funding (state aid) partially covers the related purchase costs of PV panels, the results in Case Study 5 underscore its significance in achieving a positive NPV. Case study results have shown that a potential decrease in the external funding or no funding at all in the future may not only jeopardise the economic viability of the creation of EnCs but also could heighten prosumer apprehensions regarding the economic efficiency of installing PV panels. Therefore, policymakers and legislators should contemplate either increasing or, at the very least, maintaining the current level of state aid for the development of EnC, as indicated in [8]. This approach not only incentivizes the installation of PV panels at the microgeneration level but also substantiates the economic viability of EnCs.

Results from Case Study 6 have indicated that NPV can be increased if prosumers' initial investment coverage do not exceed 50 %. Respectively, NPV is higher when total CAPEX is fully covered from the bank loan (this is justified in the description of Case Study 4) or by receiving additional one-time payments from the consumer (thus indirectly reducing total CAPEX which have to be covered by the prosumer). Although these two scenarios can increase NPV, their implementation could lead to a decrease in both consumers' economic benefits and accumulated funds (it is discussed in the following subsection).

3.3.2. Accumulated Funds

The graphic representation of the accumulated funds (the data are reflected for the 20th year) obtained by the planning tool is given in Fig. 3.

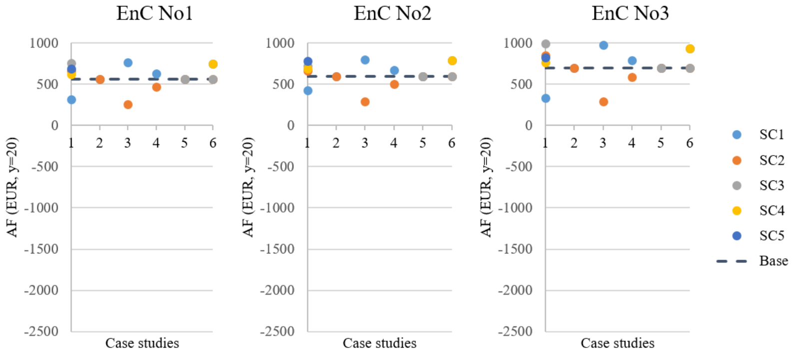

Fig. 3. Accumulated funds (AF) under used EnCs, case studies and scenarios (SCs).

EnC No3 has the highest AF among used baseline EnCs due to the increased amount of electricity generation, which leads to a higher incoming cash flow. Similar to NPV related recommendations, during the planning of the EnC, its potential members must make sure that by installing higher capacity PV panels, consumers' electricity consumption is high enough to generate more income into accumulated funds.

Results of Case Study 1 indicate that an increase in EnC sharing tariff and electricity traders' price for the purchase of excess electricity can increase the value of AF.

However, if electricity traders' offered price is significantly low, EnC income reduces considerably.

As can be seen from Fig. 3, an increase or a decrease of imported electricity tariff in Case Study 2 does not affect AF due to the fact that this indicator includes only direct cash flows and not savings in electricity costs.

The results of Case Study 3 indicate that the increased cost of PV panels per installed kW could increase OPEX, thus significantly reducing the value of AF.

Extending the duration of a bank loan leads to increased additional interest payments, CAPEX and OPEX values and in Case Study 4, the AF indicator shows a slight rise when the repayment period is shorter.

Case Study 5 indicates that external funding could reduce total CAPEX, thereby reducing the amount of bank loan. Given that the prosumer is responsible for the coverage of total CAPEX, changes in subsidies value do not affect the value of AF.

Results of Case Study 6 show that one-time payments for the full coverage of initial investments can significantly increase AF due to the fact that there is no need for bank loan, thereby also reducing annual outgoing cash flow.

3.3.3. Prosumers' Economic Benefits

The values of overall prosumers' economic benefits in the modelled case studies and scenarios are shown in Fig. 4.

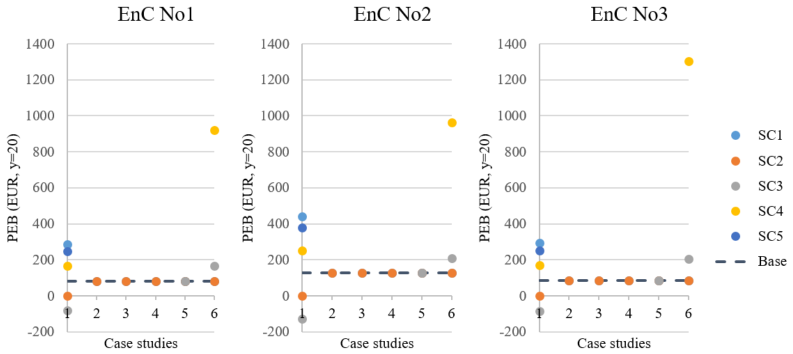

Fig. 4. Prosumers' economic benefits (PEB) under used EnCs, case studies and scenarios (SCs).

Similar to the analysis of NPV, EnC No 2 indicates the highest PEB value of all included baseline EnCs. Considering that in all reviewed EnCs, the prosumers' sharing tariff was higher than the electricity traders' price for the purchase of surplus electricity. An increase in consumers' electricity consumption means a higher income from the shared electricity, thus increasing PEB from the participation in the EnC.

As a result of Case Study 1, it can be concluded that PEB increases when electricity sharing tariff is higher than electricity traders' determined price for the purchase of excess electricity. Respectively, activities of electricity sharing and electricity selling to the electricity trader generate more income than selling all prosumers' excess amount of electricity only to the electricity trader. It is also indicated in SC2: when electricity sharing tariff and traders' purchase price are the same, PEB is equal to zero because participation in the EnC would generate the same revenue as when prosumer would not participate in the EnC and would sell its excess amount of electricity only to the electricity trader. Thereby, to increase PEB value, electricity sharing tariff should be higher than electricity traders' price for the purchase of surplus electricity.

Case Studies 2–5 indicate that an increase or a decrease in electricity import tariff, cost of PV panels per installed kW, loan duration and state aid will not affect PEB due to the fact that these changes are also applicable when the prosumer does not participate in the EnC.

The same can be stated about Case Study 6 SC1 and SC2. Nevertheless, if consumer makes one-time payments to partially cover the total CAPEX, it will be advantageous for the prosumer. Consequently, PEB increases when consumers make one-time payments, helping alleviate the financial burden of prosumer in covering PV initial costs.

3.3.4. Consumers' Economic Benefits

The values of overall consumers' economic benefits in the case studies and scenarios are shown in Fig. 5.

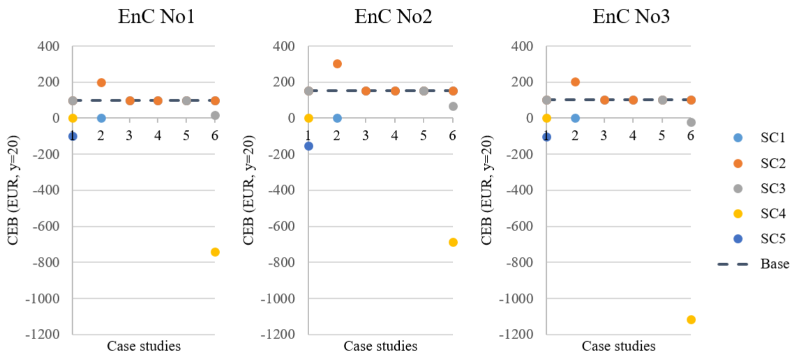

Fig. 5. Consumers' economic benefits (CEB) under used EnCs, case studies and scenarios (SCs).

Similar to the results of NPV and PEB, EnC No 2 indicates the highest CEB value of all included baseline EnCs. CEB increases when consumers' electricity production is higher, thus covering a greater proportion of its total electricity consumption with prosumer shared electricity which tariff is lower than electricity import tariff from the grid.

Case Studies 1 and 2 indicate that CEB increases when sharing tariff is lower than electricity import tariff. In addition, CEB is not affected by electricity traders' purchase price. If electricity import tariff is lower than prosumers' sharing tariff, consumer financial motivation to participate in the EnC would decrease because it would be more beneficiary to fully cover its electricity consumption with cheaper electricity from the grid than by receiving it with a higher tariff from the prosumer.

Similar to PEB values, changes to the contained data in Case Studies 3–5 do not affect CEB due to the fact that the costs associated with PV panels and the payment mechanism are the responsibility of the prosumer.

Results in Case Study 6 show that consumers' one-time payments to partially cover the total CAPEX reduce CEB. Nevertheless, depending on the amount of payment, CEB may still have a positive value.

4. DISCUSSION AND CONCLUSION

To motivate overcoming the identified barriers, the planning tool was developed based on the proposed business model using a P2P approach with accumulated funds and state aid implementation option. Moreover, the operations and mathematical calculations included in the developed planning tool were presented, thus allowing the stakeholders of the EnCs to determine NPV, AF, PEB and CEB.

To provide recommendations on measures to increase the efficiency and sustainability of the proposed EnC, planning tool modelled 3 EnCs (using different electricity consumption levels and installed PV panel capacities), 6 case studies and a total of 17 scenarios, thus allowing to analyse the impact of the following values on the specified indicators of EnC:

- consumers' tariff for received electricity from the prosumer,
- electricity traders' price for the purchase of electricity from the EnC,
- electricity tariff component for the purchase of electricity from the grid,
- CAPEX related to installed generation source capacity of 1 kW,
- loan duration,
- amount of external funding (such as state aid),
- prosumers' and consumers' one-time payment for the coverage of initial investments.

The findings from case studies and scenario modelling suggest that the effectiveness and sustainability of the creation of the proposed prosumer and consumer EnC can be enhanced through the implementation of the following recommendations:

- If electricity sharing tariff is higher than electricity traders' price for the purchase of excess electricity but lower than electricity tariff component for the purchase of electricity from the grid, members of EnC would receive positive economic benefits from the participation in the EnC;
- CAPEX related to installed generation source capacity of 1 kW must be as low as possible, thus reducing the amount of necessary one-time payment for the coverage of initial investments and amount of bank loan;
- Receiving external funding can significantly increase the NPV. It is strongly reccomended that Latvia's legislators and policymakers develop a support mechanism that would be applicable to the procedure for receiving financial support not only for prosumers, but also for the creation of EnC;
- Loan duration affects NPV and AF values and does not affect PEB and CEB. Nevertheless, to increase AF for the energy efficiency or other welfare activities in the future, it is recommended to reduce the aforementioned duration as short as possible;
- Coverage of total CAPEX must be done either from combination of prosumers' initial one-time payment and a bank loan or fully covering total CAPEX by prosumers' investments, thus raising not only the value of AF but also CEB.

Before the creation of EnC, prosumer have to be sure than consumers' electricity consumption level is high enough to increase the overall income from the shared electricity relative to the cost of PV panels.

Furthermore, the primary goal of modelled EnCs, case studies, and scenarios is to assess the impact of the specified factors on the NPV, AF, CEB and PEB generated by the planning tool. It is essential to note that the levels of consumption, generation, tariffs, costs and other factors within potential EnCs in Latvia may vary, potentially affecting the values of the aforementioned indicators – while preserving the nature of their positive or negative effects mentioned in the reccomendations. As a result, the developed planning tool can be employed as an universal instrument to analyse each prosumer and consumer EnC in Latvia individually. Furthermore, the offered business model has the potential to be used and applied in other countries. The developed planning tool and its mathematical formulations can serve as a foundation, open to further modifications for alignment with the legislative guidelines of other countries.

ACKNOWLEDGEMENTS

This publication has been supported by Doctoral Grant programme of Riga Technical University.

REFERENCES

1. Saeima (2024). *Elektroenerģijas tirgus likums*. Available at https://likumi.lv/ta/id/108834-elektroenergijas-tirgus-likums.
2. Saeima (2024). *Enerģētikas likums*. Available at https://likumi.lv/ta/id/49833-energetikas-likums.
3. COME RES (2023). *D7.3: Final policy Report and Recommendations*. COME RES Project.
4. Lesničenoka, E. (2023). *Energokopienu attīstību Latvijā kavē nepilnīgi izstrādātie normatīvie akti*. Available at https://ir.lv/2023/06/28/energokopienu-attistibu-latvija-kave-nepilnigi-izstradatie-normativie-akti/
5. Diedziņa, S. (2023). *Energokopienu izveide iestrēgusi nesakārtotos normatīvos*. Available at https://lasi.lv/par-svarigo/projekti/energokopienu-izveide-iestregusi-nesakartotos-normativos.4500.
6. AS Sadales Tīkls (2023). *AS "Sadales* Tīkls*" 2022. gada pārskats*.
7. Sabiedrisko pakalpojumu regulēšanas komisija (2023). *SPRK Elektroenerģijas tirgus 2022. gada 4. ceturksnis, nozares rādītāji.* Available at https://prezi.com/i/k5qayucvnqoo/sprk-elektroenergijas-tirgus-2022-gada-4-ceturksnis_nozares-raditaji/.
8. Ministru kabinets (2022). *Ministru kabineta noteikumi Nr. 150. Emisijas kvotu izsolīšanas instrumenta finansēto projektu atklāta konkursa "Siltumnīcefekta gāzu emisiju samazināšana mājsaimniecībās – atbalsts atjaunojamo energoresursu izmantošanai" nolikums.* Latvijas Vēstnesis, 48.
9. Valsts kanceleja (2023). *Grozījumi Elektroenerģijas tirgus likumā (23-TA-1661).* Available at https://tapportals.mk.gov.lv/structuralizer/data/nodes/63d59906-6b13-4a52-8457-6344e2cebd37/preview.
10. Pētersone, K., Vecvagare, L., & Āboltiņš, R. (2020). *Recommendations for Development of Renewable Energy Communities in Latvia*. Riga: Green Liberty.
11. Lazdins, R., Mutule, A., & Zalostiba, D. (2021). PV Energy Communities—Challenges and Barriers from a Consumer Perspective: A Literature Review. *Energies, 14 (16),* 4873. DOI: 10.3390/en14164873.
12. European Commission (2023). *Energy Communities Repository.* Available at https://energy-communities-repository.ec.europa.eu/energy-communities-repository-legal-frameworks/energy-communities-repository-policy-database_en.

13. ACER (2023). *Report on Electricity Transmission and Distribution Tariff Methodologies in Europe.* Ljubljana: ACER.
14. Lazdins, R., & Mutule, A. (2022). Scenario simulation of a small-scale energy community management. In *2022 IEEE 63rd International Scientific Conference on Power and Electrical Engineering of Riga Technical University (RTUCON),* (pp. 1–5). 9–11 October 2023. IEEE Xplore: IEEE.
15. Lazdins, R., & Mutule, A. (2024). Impact of Variable Factors on the Viability and Efficiency of Energy Communities: A Scenario Simulation Study in Latvia. In *2023 IEEE 64th International Scientific Conference on Power and Electrical Engineering of Riga Technical University (RTUCON)*, (pp. 1–5). 9–11 October 2023. IEEE Xplore: IEEE.
16. Lazdins, R., Mutule, A., & Kairisa, E. (2022). Feasibilty Study in Energy Community Business Model Development for Latvia. In *2021 IEEE 62nd International Scientific Conference on Power and Electrical Engineering of Riga Technical University (RTUCON)*, (pp. 1–5). 15–17 November 2021. IEEE Xplore: IEEE.
17. Korõtko, T., Plaum, F., Häring, T., Mutule, A., Lazdins, R., Borščevskis, O., … & Carroll, P. (2023). Assessment of Power System Asset Dispatch under Different Local Energy Community Business Models. *Energies, 16*, 3476. DOI: 10.3390/en16083476.
18. Ekonomikas ministrija (2020). *Nacionālais enerģētikas un klimata plāns 2021.-2030. gadam*. Available at https://www.em.gov.lv/lv/nacionalais-energetikas-un-klimata-plans?utm_source=https%3A%2F%2Fwww.bing.com%2F
19. Barbour, E., & Gonzalez, M.C. (2018). Projecting Battery Adoption in the Prosumer Era. *Applied Energy, 215*, 356–370. DOI: 10.1016/j.apenergy.2018.01.056.
20. Sadales Tīkls (2023). *Tipveida slodžu sadalījuma grafiks.* Available at https://sadalestikls.lv/lv/tipveida-slodzu-sadalijuma-grafiks
21. Elektrum (2016). *Elektroenerģijas tirgus atvēršana mājsaimniecībām.* Available at https://www.slideshare.net/Elektrumlv/elektroenerijas-tirgus-atvrana-mjsaimniecbm
22. Renewables Ninja. (n.d.). *Downloads*. Available at https://www.renewables.ninja/downloads#details-pv
23. Sabiedrisko pakalpojumu regulēšanas komisija (2023). *SPRK Elektroenerģijas tirgus 2023. gada 3. ceturksnis, nozares rādītāji.* Available at https://infogram.com/sprk-elektroenergijas-tirgus-2023-gada-3-ceturksnis_nozares-raditaji-1hnq4107o8w1p23?live
24. EKII (2024). *Atbalsts mājsaimniecībām*. Available at https://ekii.lv/index.php?page=atbalsts-majsaimniecibam
25. Sadales Tīkls (2023). *AS "Sadales tīkls" elektroenerģijas sadales sistēmas pakalpojumu diferencētie tarifi no 2023. gada 1. jūlija (bez PVN).* Sadales Tīkls.
26. Swedbank (2024). *Saules paneļu kredīts.* Available at https://www.swedbank.lv/private/credit/loans/solar?language=LAT.
27. Valsts kase (2024). *Diskonta likmes*. Available at https://www.kase.gov.lv/metodika/diskonta-likmes
28. Saeima (2024). *Pievienotās vērtības nodokļa likums*. Available at https://likumi.lv/ta/id/253451-pievienotas-vertibas-nodokla-likums

LATVIAN JOURNAL OF PHYSICS
AND TECHNICAL SCIENCES
2024, N 3

DOI: 10.2478/lpts-2024-0019

EXTENDING TRANSCEIVER CAPACITY WITH A SCALABLE SPECTRUM SLICING TECHNIQUE FOR OPTICAL ACCESS NETWORKS

L. Skladova[1,2,*], R. Murnieks[1,2], I. Kurbatska[1], A. Ostrovskis[1,2],
V. Bobrovs[1], S. Spolitis[1,2]

[1] Institute of Telecommunications,
Riga Technical University
12 Azenes Str., Riga, LV-1048, LATVIA
[2] Communication Technologies Research Center,
Riga Technical University
12 Azenes Str., Riga, LV-1048, LATVIA
*e-mail: laura.skladova@rtu.lv

The paper demonstrates a spectrum slicing technique applied to PAM-4 modulated signal spectrum at 40 Gbaud baudrate for optical access networks. The spectrum slicing is shown in VPIphotonics simulation environment, where characteristics of key components are measured in the laboratory and loaded into the corresponding elements of the simulation setup. The spectrum of electrical baseband signal is sliced in four slices introducing an additional degree of freedom – higher data rate signals can be transmitted by re-using already-existing lower bandwidth transceiver components in an optical access network. This tackles the electronic bottleneck enabling the on-demand variable bandwidth allocation and extends the life span of opto-electrical components during network upgrades. Furthermore, the use of the proposed spectrum slicing technique has a positive side-effect when it comes to security concerns, as the signal spectrum is divided into slices. All slices are necessary to obtain the reconstructed signal and even if an eavesdropper gets most of the slices it is still not enough. The simulation results show that the proposed spectrum slicing and stitching approach is a viable solution to overcome the problem of limited frequency bandwidth of electrical components.

Keywords: *Fast Fourier Transform (FFT), optical access network, pulse amplitude modulation 4 (PAM-4), spectrum slicing, transceiver.*

1. INTRODUCTION

The bandwidth of electrical and opto-electrical components of a transceiver is a major limiting factor causing a bottleneck in fiber optic networks [1]–[3]. Spectrum slicing aims to reuse the existing transceiver's low bandwidth equipment (such as Mach-Zehnder modulator (MZM) and PIN photodiode) to satisfy high bandwidth demands in optical access networks. This technique uses digital signal processing (DSP) to slice the electrical baseband data signal into parts (i.e., spectrum slices). These sliced parts are transmitted through the wavelength-division multiplexed passive optical network (WDM-PON), and then the reconstructed signal is assembled at the receiver [4]–[6].

Next-generation optical access networks, for example, Super-PONs standardized by IEEE 802.3 Working Group [7], must be adaptive when it comes to the ensured data transmission frequency bandwidth. The bandwidth must change dynamically depending on the user demand. In this regard, spectrum-slicing solutions with DSP have a potential to overcome the restrictions of the limited frequency bandwidth of electrical components. Spectrum slicing also introduces another level of security in optical access networks. The signal spectrum is divided into slices and all slices are necessary to obtain the reconstructed signal. Even if an eavesdropper gets most of the slices, it is still not enough to get the reconstructed signal. M-PAM allows transmitting $\log_2(M)$ more data bits over the same bandwidth as non-return-to-zero (NRZ). Therefore, we can slice M-PAM optical signal bandwidth in a smaller number of slices to transmit higher bit rate signals (e.g., doubled or quadrupled) compared to previous research, where NRZ is used [1], [2], [4]–[6]. The authors in [2] achieved maximum transmission rate of 56 Gbit/s and in [5] the maximal reach of 40 km for 10 Gbit/s. In addition, [8] shows that potential energy consumption reduction is measured in hundreds of wats if spectrum slicing using DSP is applied. Even though DSP block adds to energy consumption that depends on the number of operations to perform and specific ASIC implementation, the overall energy consumption is lowered. Effective modulation formats in sense of bits per symbol, for instance, M-PAM, can further reduce power by minimising the required energy to process one bit. This fact can significantly reduce operational expenditure (OPEX) [9]. However, M-PAM implementation is challenging since it has more signal levels and is more sensitive to signal distortions.

The next consideration is the multiplexing scheme for transmitting slices over the network. It depends on the application type – non-real-time and real-time [5]. Non-real-time applications can be supported by time-division-multiplexing (TDM). However, additional synchronization and scheduling techniques are required. In contrast, for real-time applications, wavelength division multiplexing (WDM) allows transmitting each slice on a separate wavelength. WDM also boosts network upgrade to achieve an increase in capacity and reach. Furthermore, no additional inverse Fast-Fourier transform (IFFT) is needed before the WDM multiplexer [8]. It is important to mention that sliceable transceivers have also been studied for metro networks [10], where a high-capacity flow of 100 Gbit/s is established by slicing the signal into two 50 Gbit/s slices [11]. However, metro networks are out of scope of this research as they use different modulation format –

DP-16QAM at 32 Gbaud.

This paper aims at studying a configuration of spectrum-sliced optical access network that requires a lower number of slices to transmit a higher bit rate signal, and simultaneous transmission of these slices over the network. As a result, we have built a 40 Gbaud PAM-4 system with a spectrum slicing technique in VPIphotonics Design Suite [12] supported by MATLAB [13] software. The component characteristics are measured in laboratory and loaded into simulation setup. The bandwidth of 40 Gbaud PAM-4 modulated optical signal is sliced in four slices, each having 10 GHz bandwidth, and transmitted simultaneously over WDM channels. This study demonstrates that telecommunications service providers can ensure the transmission of at least four times broader bandwidth signals than the already-existing equipment allows. The number of slices is determined by the bandwidth of a 10 Gbit/s transceiver and the data signal. 10 Gbit/s electronic equipment is currently the most widely used in the telecommunications industry. We use a transceiver with -3 dB bandwidth of 12 GHz and 40 Gbaud PAM-4 data signal. A higher baudrate would result in the necessity to upgrade electronic components such as digital-to-analogue converter (DAC) and analogue-to-digital converter (ADC) to support 40 GHz frequency bandwidth. That, in turn, means capital investments for substituting the already existing optical access network equipment. Four slices are chosen since they occupy the whole bandwidth of a transceiver and allow using 10 Gbit/s equipment. Additionally, the spectrum slicing technique can be helpful for WDM-PON networks used to deploy 5G communications, where each wavelength should have at least 25 Gbit/s or higher data rates [14]–[16].

The rest of the paper is structured as follows. Section 2 explains how the spectrum slicing technique is implemented using a DSP block. The simulation setup of the optical access network in the downlink to analyse the spectrum slicing technique is shown in Section 3. Section 4 presents the obtained results as spectra and waveform of each slice, eye diagram, and bit error rate (BER) correlation diagrams of the reconstructed signal. This section also provides a discussion of the obtained results. Finally, Section 5 concludes with the usefulness of the proposed technique in avoiding the limited bandwidth problem.

2. SPECTRUM SLICING USING DSP BLOCK

Signal slicing divides a high bandwidth electrical signal spectrum into several lower bandwidth signals. Signal slicing and stitching at the transmitter's and receiver's sides require DSP, as shown for the downlink scenario in optical access networks in Fig. 1. The figure demonstrates signal slicing in four slices used in this research.

Spectrum slicing is implemented with a DSP block in the optical line terminal (OLT), but the stitching of a signal is implemented with another DSP block in the optical network terminal (ONT). The process of spectrum slicing starts when the DSP block receives PAM-4 signal in the time domain. The first operation is to transfer the electrical signal from the time domain to the frequency domain using Fast Fourier Transform (FFT). Then N mathematical rectangular filters with no attenuation and latency divide the spectrum of a signal into slices. After that, slices in the passband (except the first slice) are down-converted to the baseband. Finally, each slice is converted back to the time domain using inverse Fast Fourier Transform (IFFT) to be sent to electro-optic modulators. The proposed spectrum slicing method is scalable in bandwidth.

The process of signal stitching is similar at the receiver's side but in reverse order as spectrum slicing. The received electrical signals representing slices are converted to the frequency domain using FFT. Next, all slices except the first one are up-converted to the initial passband position. The reconstructed signal is obtained by combining all slices into one spectrum. Finally, the signal is converted back to the time domain using iFFT and sent to the signal analyser for quality measurements.

The electrical signal with N GHz frequency bandwidth can be sliced into multiple slices. The number of slices depends on the electrical signal data rate and the signal is sliced in the exact number of slices for each slice to match the transceiver bandwidth [5], [6].

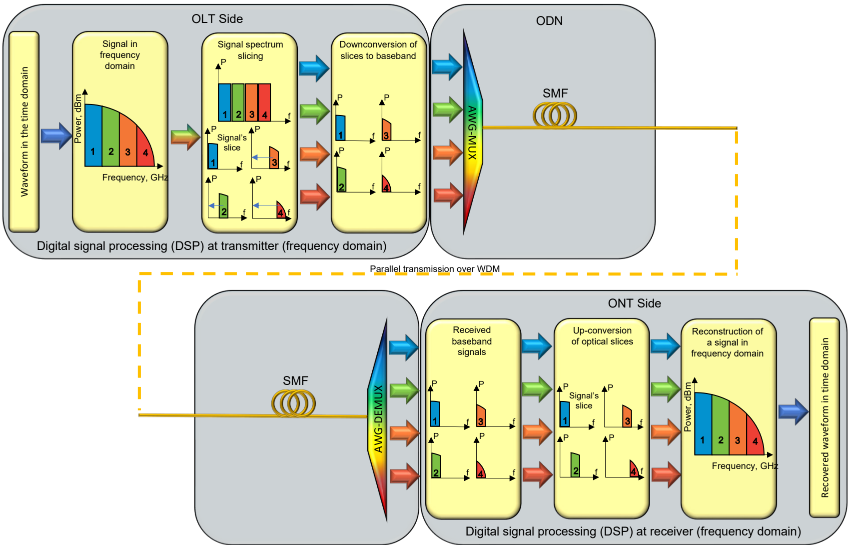

Fig. 1. The proposed principle of slicing an input electrical baseband signal into equal bandwidth slices at the OLT, and a reconstruction of the original signal waveform at the ONT.

Signal slices are transmitted simultaneously over different WDM channels in an optical distribution network (ODN). The used bandwidth of the electro-optical and electrical components of the transceiver is scalable and the necessary electrical bandwidth of the high-frequency network hardware is at least two times smaller than in the case of the initial electrical signal before slicing.

3. STRUCTURE OF THE SETUP

The simulation setup of a WDM-PON system employing spectrum slicing in an OLT to divide 40 Gbaud PAM-4 signals into four 10 GHz slices is shown in Fig. 2. Each slice is transmitted in parallel on a separate wavelength in ODN over ITU-T G.652.D single-mode fiber (SMF) span. Each slice is received, returned to the initial passband position, and the original signal is reconstructed in an ONT. Channel spacing is chosen to be 100 GHz according to the ITU-T G.694.1 recommendation. The 100 GHz channel spacing is chosen over 50 GHz to reduce the crosstalk between adjacent 40 Gbaud PAM-4 channels and improve the BER performance. The parameters of various simulation blocks are set according to equipment available in our lab for further experimental validation purposes.

OLT starts with 40 Gbaud PAM-4 signal generation, which is shown as a PAM-4 block. In a simulation, two pseudo-random bit sequences (PRBS15) with a length of 2^{15} -1 are fed to separate NRZ encoders. The outputs of NRZ coders are combined with a power coupler to form a 40 Gbaud PAM-4 signal. Generated PAM-4 data signal is sent to the DSP block (explained in detail in the previous section). DSP block is implemented in MATLAB and performs spectrum slicing in the simulation environment. The sampling rate of 16 samples per symbol and a data rate of 40 Gbaud are the main parameters considered. We obtain N number of slices as separate waveforms at the output of the DSP block (after the digital-to-analogue converter (DAC)). The signal slices (waveforms) are then sent to MZMs in OLT transmitters. Individual waveforms or slices (N = 1…4) that are separately sent to MZMs are shown in Fig. 2 as dashed lines for simplicity (otherwise slices are sent over individual electrical lanes).

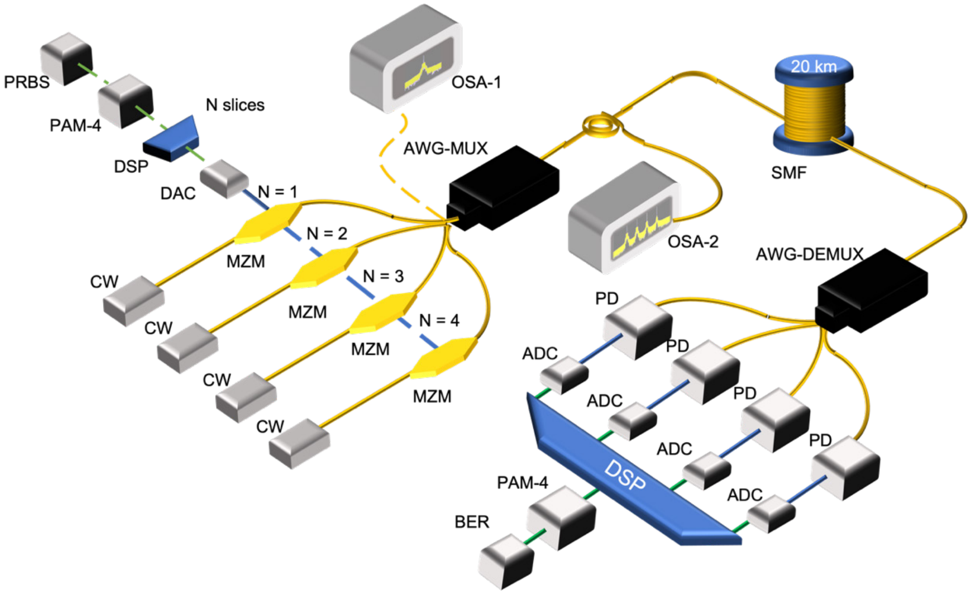

Fig. 2. The WDM-PON setup to analyse PAM-4 signal transmission using a spectrum slicing technique.

OLT transmitter consists of a continuous wave (CW) laser, MZM modulator, DC block for MZM biasing. CW lasers provide optical carriers with an output power of +15 dBm and central frequencies of 193.1, 193.2, 193.3, and 193.4 THz – one for each slice. Channel spacing of 100 GHz ensures negligible optical crosstalk. The laser linewidth is set to 100 kHz, and the side mode suppression ratio to 30 dB. MZM modulator with an extinction ratio of 20 dB modulates the waveform onto an optical carrier. We have measured the 12 GHz MZM amplitude response in a laboratory and loaded it into the simulation to ensure modulator operation as close to the laboratory as possible. Arrayed waveguide grating multiplexer (AWG-MUX) combines modulated optical carriers from all OLT transmitters for further transmission over ODN. AWG-MUX has 3-dB bandwidth of 75 GHz. ODN is implemented as variable-length ITU-T G.652 single-mode fiber (SMF) span with 0.02 dB/km attenuation and 16 ps/nm/km dispersion coefficient at 1550 nm reference wavelength. An optical spectrum analyser (OSA-1) is used before an AWG-MUX to measure the spectra and waveform of each slice, but OSA-2 measures all combined slices before the SMF transmission.

An AWG-DEMUX, with a 3-dB channel bandwidth of 75 GHz, demultiplexes the signal into four separate slices after the signal transmission over ODN. Then each slice is sent to the corresponding PIN photodiode in the ONT receiver. PIN photodiode has 0.7 A/W responsivity and BER 10^{-12} at a sensitivity level of -20 dBm. PIN receives a slice and converts it to an electrical signal to be sent to the DSP block for the reconstruction of the original signal. We have also measured the amplitude response of a 3-dB bandwidth of a 12 GHz PIN photodiode in a laboratory and loaded it into the simulation to ensure photodiode operation as close to the laboratory as possible. After analogue-to-digital converter (ADC) converts electrical signal into a digital signal, the DSP block reconstructs the original signal, and we obtain the original electrical signal in the time domain (waveform) at the output of this block. BER estimation of the reconstructed signal is performed in the VPI simulation setup.

4. RESULTS AND DISCUSSION

We use an eye diagram (Fig. 3a) to qualitatively assess the signal before the fiber transmission. Eye diagrams of the reconstructed 40 Gbaud PAM-4 signal after the B2B transmission are shown in Figs. 3b and 3c.

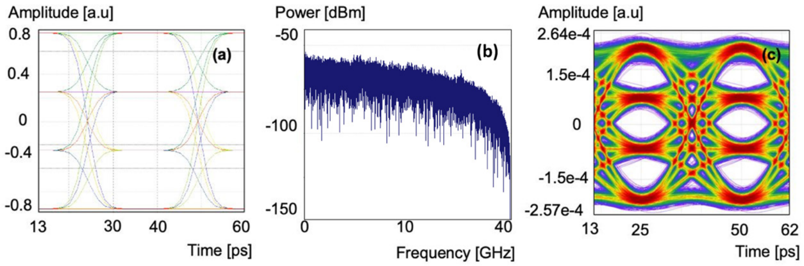

Fig. 3. Diagram of the signal before the fiber transmission, where (a) the eye diagram of the original electrical signal, (b) the electrical spectrum of the reconstructed PAM-4 signal, and (c) the eye diagram of the reconstructed 40 Gbaud PAM-4 signal after B2B transmission.

As shown in Fig. 3b, the spectrum of the reconstructed signal after B2B transmission is relatively smooth. No amplitude fluctuations can be seen in the transition areas of each slice. The eye diagram of the received signal is well open, and all four levels are distinguishable as no time skew or amplitude compression is observed in Fig. 3. The BER value after the B2B transmission is 1.1×10^{-7}, and the obtained BER value is well below the FEC threshold (e.g., 1×10^{-3}) [17]. Spectrum slicing and the original signal reconstruction process reduces the BER value from ideal to 1.1×10^{-7}. This aspect must be considered before the signal transmission over the SMF fiber span.

Next, we show the optical spectra and the waveform of each slice. Observing if the shape of optical spectra and waveform of each slice does not change during signal transmission is critical. The change means that the reconstruction of the original signal is impossible. That, in turn, means that spectrum slicing cannot be used to transmit higher bandwidth signals over a lower bandwidth transceiver. Figure 4 summarises the optical spectra of each slice at the output of the OLT transmitter. Figure 5 shows optical spectra of all four slices at the output of AWG-MUX and after the transmission over SMF fiber. The central frequency in Figs. 4 and 5 is set to 193.25 THz for representation purposes. Accordingly, the central frequencies of the carriers are 193.1, 193.2, 193.3, and 193.4 THz.

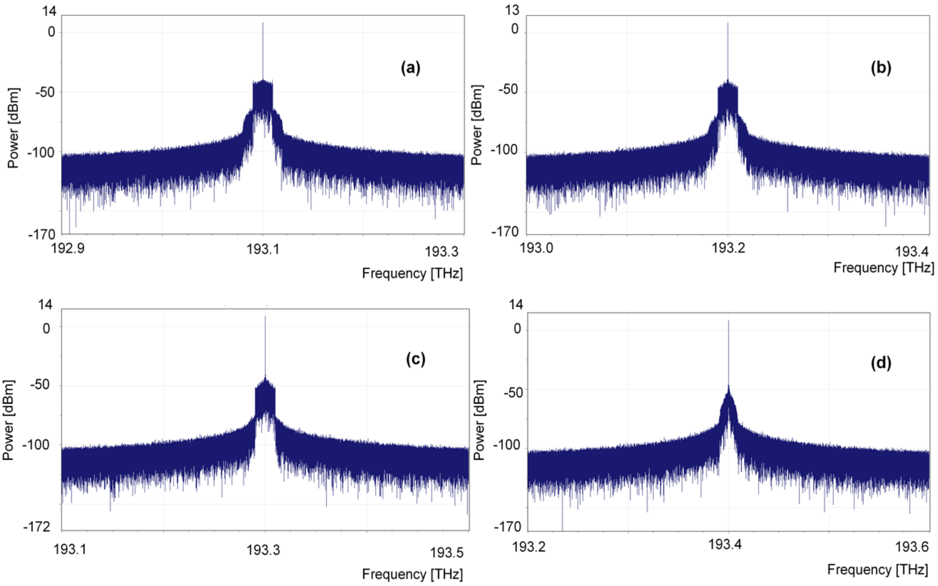

Fig. 4. Optical spectra of each slice on the output of OLT transmitters (a, b, c, d).

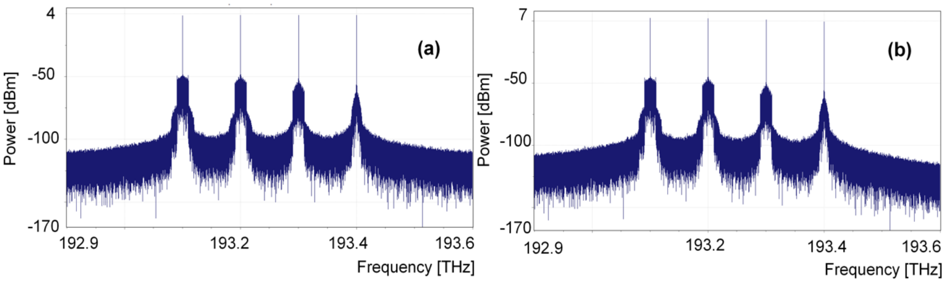

Fig. 5. Optical spectra of four slices – (a) at the output of AWG-MUX and (b) at the output of transmission fiber.

The spectrum of each slice retains the shape after the AWG-MUX combines signals coming from the OLT transmitters if comparing Figs. 4a–d. The shape of the spectrum also does not change after signal transmission over ODN as seen by comparing Figs. 5a and 5b. The only difference here is the attenuation, but all spectral components are attenuated evenly, which will not affect signal reconstruction. We can already state that signal reconstruction is possible as the spectra does not change, and spectrum slicing is viable to fulfill its purpose.

We perform BER counting for the received PAM-4 signal after reconstructing the original signal to assess the transmission quality quantitively. Figure 6 illustrates eye diagrams of the reconstructed PAM-4 signal after 10 km and 20 km transmission distances, respectively. As one can see from Figs. 6a and 6b, the eye stays relatively open despite the increasing transmission distance. The obtained BER values for 40 Gbaud PAM-4 signal sliced in four slices are 1.1×10^{-6} and 2.6×10^{-4} for 10 km and 20 km transmission distances, respectively. These BER values are below the FEC threshold of 1×10^{-3}.

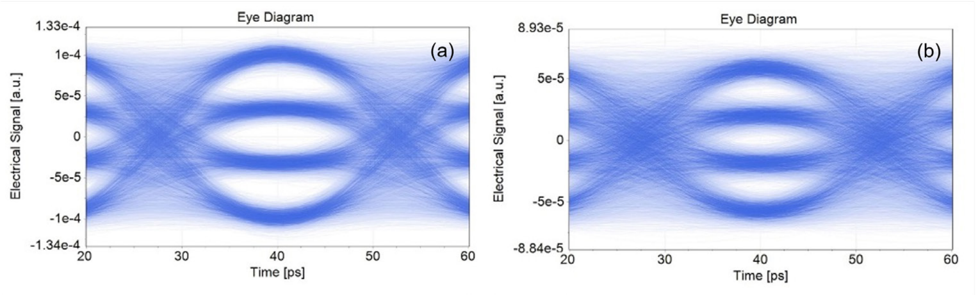

Fig. 6. Eye diagrams for the reconstructed 40 Gbaud PAM-4 signal after (a) 10 km and (b) 20 km transmission distance.

We use the BER correlation diagram to assess how transmission distance changes the BER value. Figure 7a shows BER changes for the worst-performing data channel for 40 Gbaud PAM-4 signal sliced in four slices. The diagram indicates the maximal transmission distance without the dispersion compensation of 22 km, where the BER value stays below the FEC threshold. Maximal transmission distance corresponds to a standard optical access network length.

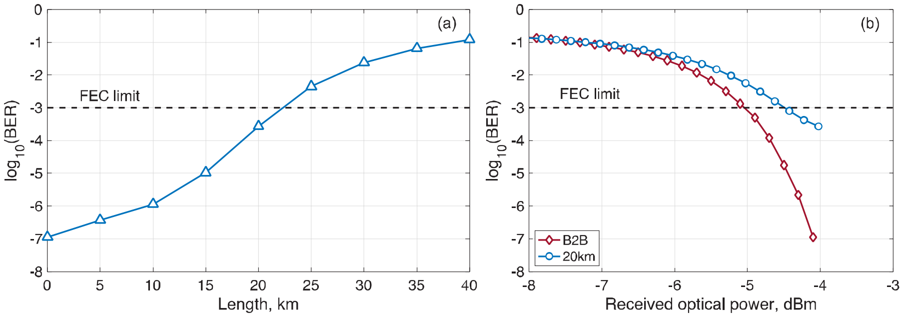

Fig. 7. BER correlation diagrams for 40 Gbaud/s PAM-4 signal sliced in four slices – (a) BER versus fiber length and (b) BER versus average received signal power for B2B and 20 km transmission.

Further, the BER versus average received signal power for B2B and 20 km transmission is investigated. As shown in Fig. 7b, a slight decrease in the received signal power yields a considerable increase in BER. A drop of 2 dB (at the pre-FEC BER level) of the received signal power in both B2B and 20 km fiber span results in the BER value above the FEC threshold. It is difficult to ensure proper signal transmission at such received optical power. Figure 7b also shows that in the case of B2B transmission, the minimal received signal power level on the PIN photoreceiver should be about -5 dBm. However, for 20 km of SMF span, the minimal received power should be about -4.5 dBm to ensure the FEC threshold of 1×10^{-3}. Considering optical power at the input of optical fiber (8 dBm), the power budget to ensure the FEC threshold for B2B transmission is 13 dB, and for 20 km of SMF fiber span is 12.5 dB. These results indicate that power budget is one of the most important considerations when choosing spectrum-slicing for extending the capacity of the transceiver of an optical access network. The inaccurate planning of the power budget can drastically reduce the performance and viability of the proposed solution.

5. CONCLUSIONS

We have successfully demonstrated the proposed spectrum slicing based on DSP. 10 GHz transceiver is capable of transmitting the whole 40 Gbaud PAM-4 waveform over up to 22 km SMF span by slicing it into four slices each occupying 10 GHz bandwidth. Slices are transmitted in parallel using the WDM approach, where each electrical slice is modulated on a separate optical carrier. It is not necessary to buy new equipment for each network upgrade migrating to higher speeds (e.g., from 10 Gbit/s NRZ to 80 Gbit/s PAM-4) by using this technology. The already existing opto-electrical equipment (e.g., 10 GHz transceivers) can be upgraded by using the proposed spectrum slicing technique.

REFERENCES

1. Lavery, D., Gerard, T., Erkilinc, S., Liu, Z., Galdino, L., Bayvel, & Killey, R.I. (2019). Opportunities for Optical Access Network Transceivers Beyond OOK [Invited]. *J. Opt. Commun. Netw*, *11* (24), A186–A195. DOI:10.1364/JOCN.11.00A186
2. Spolitis, S., Olmos, J.J.V., Bobrovs, V., Ivanovs, G., & Monroy, I.T. (2013). A novel approach for transmission of 56 Gbit/s NRZ signal in access network using spectrum slicing technique. In *Asia Communications and Photonics Conf.*, 12–15 December 2013 (AF4D.2). Beijing, China: OSA.
3. Kaminow, I.P., Li, T., & Willner, A.E. (2008). *Optical Fiber Telecommunications VB. Systems and Networks*. USA: Elsevier.
4. Spolitis, S,, Wagner, C., Olmos, J.J.V., Bobrovs, V., Ivanovs, G., & Monroy, I.T. (2014) Experimental demonstration of a scalable sliceable transceiver for optical access networks. In *Asia Communications and Photonics Conf.*, 11–14 November 2014 (ATh1H.3). Shanghai, China: OSA.
5. Wagner, C., Madsen, P., Spolitis, S., Olmos, J.J.V., & Monroy, I.T. (2015). Sliceable transponders for metro-access transmission links. In *SPIE Photonics West, Optical Metro Networks and Short-Haul Systems*, 7 February 2015 (938805). San Francisco, USA: SPIE.

6. Wagner, C., Spolītis, S., Olmos, J., Bobrovs, V., & Monroy, I.T. (2015). Re-use of low bandwidth equipment for high bit rate transmission using signal slicing technique. In *Asia Communications and Photonics Conf.,* 19–23 November 2015 (ASu5E.3). Hong Kong, Hong Kong: OSA.
7. DeSanti, C., Du, L., Guarin, J., Bone, J., & Lam, C. (2020). Super-PON: an evolution for access networks [Invited]. *J. Opt. Commun. Netw*, *12*, D66-D77. DOI: 10.1364/JOCN.391846
8. Cercos, S.S., Wagner, C., Olmos, J.J.V., Fagertun, A.M., & Monroy, I.T. (2015). Digital signal processing for sliceable transciever for optical access networks. In *Symposium on Computers and Communication,* (pp. 483–488). 6–9 July 2015 Larnaca, Cyprus: IEEE.
9. Udalcovs, A., Levantesi, M., Urban, P., Mello, D. A.A., Gaudino, R., Ozolins, O., & Monti, P. (2020). Total Cost of Ownership of Digital vs. Analog Radio-Over-Fiber Architectures for 5G Fronthauling. *IEEE Access*, *8*, 223562–223573. DOI: 10.1109/ACCESS.2020.3044396
10. Nadal, L., Fabrega, J.M., & Moreolo, M.S. (2019). Programmable sliceable transceivers based on multicarrier modulation in disaggregated optical metro networks. *In 21st International Conference on Transparent Optical Networks*, 9–13 July 2019 (Th.B3.5). Angers, France: IEEE.
11. Nadal. L., Moreolo, M.S., Hernandez, J.A., Fabrega, J.M., Casellas, R., Munoz, R., ... & Martinez, R. (2020). SDN-Enabled S-BVT for Disaggregated Networks: Design, Implementation and Cost Analysis. *J. Light. Technol.*, *38* (11), 3037–3043. DOI:10.1109/JLT.2020.2969457
12. Spolitis, S., Kurbatska, I., & Bobrovs, V. (2019). Evaluation of the impact of MZM frequency response on BER performance of PAM-4 modulated WDM-PON. In *Photonics & Electromagnetics Research Symposium*, (pp. 2037–2042). 17–20 June 2019 Rome, Italy: IEEE.
13. Hwang, Y., Choi, D., An, H., Shin, S., & Lee, C.G. (2019). Developments of Python-MATLAB interface program for optical communication system simulation. In *International Conference on Green and Human Information Technology*, (pp. 46–48). 15–17 January 2019, Kuala Lumpur, Malaysia: IEEE.
14. Wey, J.S., & Zhang, J. (2019). Passive Optical Networks for 5G Transport: Technology and Standards. *J. Light. Technol.*, *37* (12), 2830–2837. DOI: 10.1109/JLT.2018.2856828
15. GSM association (2018). *Study on Socio-Economic Benefits of 5G Services Provided in mmWave Bands.* Available at https://www.gsma.com/spectrum/wp-content/uploads/2019/10/mmWave-5G-benefits.pdf
16. Udalcovs, A., Salgals, T., Zhang, L., Pang, X., Djupsjobacka, A., Spolitis, S., ... & Ozolins, O. (2020). Optical Power Budget of 25+ Gbps IM/DD PON with Digital Signal Post-Equalization. *Appl. Sci.*, *10* (17), 6106. DOI: 10.3390/app10176106
17. Pang, X., Ozolins, O., Gaiarin, S., Olmedo, M.I., Schatzg, R., Westergren, U., ... & Jacobsen, G. (2016). Evaluation of high-speed EML-based IM/DD links with PAM modulations and low-complexity equalization. In *42nd European Conference and Exhibition on Optical Communications*, (pp. 872–874). 18–22 September 2016, Dusseldorf, Germany: VDE.

LATVIAN JOURNAL OF PHYSICS
AND TECHNICAL SCIENCES
2024, N 3

DOI: 10.2478/lpts-2024-0020

EVOLVING CONCEPT OF ENERGY COMMUNITIES IN THE EUROPEAN UNION

M. Auders*, S. Lapuke

Riga Technical University,
Faculty of Engineering Economics and Management,
6 Kalnciema Str. 210, Riga, LV-1048, LATVIA
*e-mail: martins.auders@edu.rtu.lv

In accordance with the goal approved by the Council of the European Union, a European climate-neutrality must be achieved by 2050. Namely, the European Union must significantly reduce greenhouse gas emissions and find ways to compensate for the remaining and unavoidable ones. Within the framework of the European Green Deal, which is a set of policy initiatives to achieve climate neutrality goals, energy communities are considered in the context of two initiatives: a just transition and clean and safe energy at an affordable price. Within the latter, energy community is seen as citizen-led actions in the energy sector that will help pave the way for the transition to clean energy.

Keywords: *Energy community concept, legal framework, renewable energy, terminology.*

1. INTRODUCTION

In accordance with the goal approved by the Council of the European Union, a European climate-neutrality must be achieved by 2050. It means that, by the year 2050, the European Union (EU) must significantly reduce greenhouse gas (GHG) emissions and find ways to compensate for the remaining and unavoidable emissions. Within the framework of the European Green Deal, which is a set of policy initiatives to achieve climate neutrality goals, energy communities (EC) are considered in the context of two initiatives: a just transition and clean and safe energy at an affordable price. Within the latter, EC are seen as citizen-led actions in the energy sector that will help pave the way for the transition to clean energy.

With the emergence of alternative energy sources and the ability to generate electricity using more readily available primary energy sources (i.e., solar radiation, wind energy, geothermal heat, renewable gases etc.), it is possible to move towards a more decentralised energy production scheme. This differs from the traditional scheme with a limited number of participants, where energy is transported over long distances from large production centres. According to the policy makers of the EU, the introduction of the EC concept is the way to restructure the energy system, thus allowing citizens to actively participate in the energy transition and, as energy consumers and prosumers in residential homes, to enjoy greater sustainability benefits.

2. THE ORIGIN OF THE ENERGY COMMUNITY CONCEPT: LITERATURE REVIEW

The origins of EC in Europe can be traced back to the 1970s and 1980s in Sweden, the Netherlands, and Denmark, with later developments in Germany, the United Kingdom, and other countries. Initially, these communities focused on the production of renewable energy – both electricity and heat supply. Thousands of initiatives around the world can now be considered to address EC, highlighting the global reach and adoption of this concept [1].

However, it is only in the last decade that research on this topic expanded significantly [2]. EC also appear under such terms as "community energy initiatives (projects)" and "energy cooperatives" [3], renewable energy communities [4], smart energy communities [2], prosumer communities [5], citizens energy communities [6] and other.

In the literature, it has been presumed that the term "energy community" is controversial and can raise a series of questions [1]. There are authors who focus on typology of energy communities, while others concentrate on geographical and local trends, and communities as small businesses, or communities as owners of energy infrastructure [1].

De São José et al. [2] believe that the energy community is one of the types of smart energy communities, and, referring to Barbour et al. [7], and Gorroño-Albizu et al. [8], an energy community: "…is a community of producing consumers that shares or sells energy within the community or to the grid." De São José et al. [2] have also listed other types of smart energy communities, including smart building communities (building clusters), renewable energy communities, and other communities that could be classified as energy communities. Regarding the term "energy community", they expressed the opinion that given the possibility of various forms of energy communities, a unifying term is needed to encompass these diverse manifestations.

Wirth [9] views community energy projects as local residents' involvement in various renewable energy initiatives, for example, in the context of wind energy, where large-scale wind parks do not gain local community support, whereas community-scale projects enjoy widespread public support. At the same time, this author also points out that the term "community" is not clear and unambiguous, and, therefore, it should be clarified [9].

Eagle and Jones believe that in most academic studies and literature, almost no analysis is directed towards determining what "community" means [10]. These authors also associate community energy initiatives with localism, which is contrasted with globalisation and described as a movement to reclaim sovereignty over the local economy in the era of globalisation [10].

In the urban context, the concept of "community" is understood as a specific geographical area characterised by similar physical properties and a network of social ties. The size of a community is not fixed, and it can range from a group of physically similar buildings to an area nearly the size of a district, which includes various uses but is unified by a common identity [11].

Residents have different energy consumption needs, including comfort temperature [12]. Walker and Devine-Wright [13] examine community energy projects according to two dimensions: process and outcomes. The process dimension refers to the need for significant local resident involvement in planning, creation, and possibly project management. The outcome dimension concerns the benefits of the project and how they are distributed among local residents.

Moroni et al. [2] have provided the following classification of communities related to energy:

- communities not related to a specific location. Such a community does not require a geographical connection, therefore, its members can join in various ways;
- communities related to a specific location. They can be located in a single building, including apartment properties in a building, a neighbourhood, or a city. They may have the advantage of using the same network, short transmission distance for shared electricity, and other aspects related to physical distance; moreover, they can help achieve various local objectives;
- single-purpose communities. Communities that are established for only one purpose – to manage energy production, consumption, or procurement;
- multi-functional communities. In addition to energy objectives, these communities can also share other types of goods or services [2].

Although Moroni et al. have classified communities not related to a specific location, there are authors who believe that EC can be formed by consumers, producers, and prosumers located in a specific geographical area [14]. On the other hand, Barbour et al. [7] are not so strict regarding a specific location, as their proposed definition of energy communities suggests that the community is usually (but not exclusively) related to a specific location.

3. THE CONCEPT OF ENERGY COMMUNITY IN THE CONTEXT OF THE OBJECTIVES SET BY THE EU

Many authors also associate the concept of EC with the objectives of the European Union. For instance, Amato et al. [15] point out that Europe has set an ambitious goal to become the first carbon-neutral continent by 2050. Therefore, it has undertaken several initiatives to promote the transition in the energy sector, including the active participation of citizens in the energy industry. According to the authors, the concept of EC has been introduced in the European directives so that community members can consume, share and store locally produced energy [15]. Other authors have expressed a similar opinion, namely, that the concept of EC allows prosumers to utilise locally produced energy and reduce the need for external energy deliveries.

This can lead to significant cost savings and increase the percentage of green energy [16], as well as provide an opportunity for alternative energy system organisation and management methods in the future: smart energy transmission, distribution and metering [17], [18], digital twinning, introduction of green energy sources, for example, gases, in conventional energy distribution and transmission networks [19]–[22]. In future, it could also help minimise impact of energy delivery disruptions during local energy crisis that could occur in practically every centralised and extended energy delivery network [23].

It must also be pointed out that, under the Electricity Market Directive, the EU members have the option to grant EC the right to own, establish, purchase or lease a grid infrastructure. They can be engaged in network operations either under the general regime (public grid) or as closed distribution system operators.

Once an EC is granted the status of a distribution system operator (DSO), it is subject to the same rights and obligations as other kinds of DSO. These include unbundling rules and the related exemptions for DSOs that serve less than 100 000 final customers.

Other authors believe that energy communities will provide end-users with democratic, open access to the network and collective self-consumption. Some again argue that EC will provide end-users with democratic, open access to the network and collective self-consumption. They will promote decentralisation and foster the use of distributed renewable energy sources [24], [25].

Cuenca et al. [14] associate EC with the concept of the sharing economy and express the view that an energy community is defined as a community-driven institution that takes social control over common energy resources through decentralisation.

Similarly, it is visible in the literature that the concept of EC needs to be defined in legislation to engage the public in energy production, and the definition of EC is also mentioned in connection with the rights of prosumers [26]. A similar view has been expressed by Aruta et al. [27], pointing out that residents need to transform from being passive consumers to active prosumers, becoming part of an EC.

In order to extend the life cycle of buildings and to ensure the comfort of every building user, it is necessary to provide the managed property with quality management and maintenance services and organise maintenance properly [12].

Peer-to-peer trading as a form of energy sharing within energy communities has been mentioned by Ciobanu et al. [28]. Meanwhile, Löbbe et al. [29], as well as Hahnel et al. [30], have examined peer-to-peer trading within energy communities in more detail [30]. Despite the consensus among researchers that the essence of the EC concept is to decentralise energy production by involving residents, as believed by de Almeida, Cappelli, Klausmann, and van Soest [31], there is still ongoing debate between researchers and policymakers about what kind of decentralised energy exchange is associated with peer-to-peer trading and what kind is associated with an EC, resulting in many conflicting definitions. This is also due to the fact that before the introduction of the Clean Energy Package in the EU legislation, the term “community” was not used consistently, thus leading to ambiguity in scientific publications and policy debates.

4. ANALYSIS OF THE EU REGULATION

The reference that not every “energy community” is considered an energy community according to European Union regulations stems from the European Parliament and Council Directive (EU) 2019/944 on common rules for the internal market for electricity, amending Directive 2012/27/EU, consideration 43, which clarifies that this directive recognises only certain categories of pre-existing resident electricity initiatives at the Union level as "citizen energy communities". However, despite such a reference in the directive, this aspect has not been given due attention in the literature, and there is hardly any analysis of the EU regulation in publications.

An exception is the article by de Almeida et al. "Peer-to-Peer Trading and Energy Community in the Electricity Market – Analysing the Literature on Law and Regulation and Looking Ahead to Future Challenges". In this article, the authors indicate that, according to the EU regulation, the following models related to decentralised energy exchange can be distinguished:

- individual self-consumption;
- collective self-consumption;
- peer-to-peer trading;
- ECs.

Compliance with established EU regulation on building energy, energy efficiency is relevant for each country's economy and is one of the national priorities [32].

If there are no fundamental disagreements in the literature about distinguishing collective self-consumption from energy communities, then peer-to-peer trading within the framework of energy communities is examined in the works of many authors. As Almeida et al. [31] point out, Directive (EU) 2019/944 simultaneously uses the terms "peer-to-peer trading" and "renewable energy sharing within a renewable energy community", thereby distinguishing these models from each other in the directive. Therefore, Almeida et al. [31] believe that the European Union has adopted a definition that strives to be inclusive, but at the same time, understands peer-to-peer trading differently from the model described in most of the literature.

Examining the European Parliament and Council Directive (EU) 2019/944, it is apparent that a "citizen energy community" is defined as a legal entity that can engage in production, including from renewable resources, distribution, supply, consumption, aggregation, energy storage, energy efficiency services provision, electric vehicle charging services, or provide other energy services to its members or shareholders. Thus, an EC can engage in both energy production and aggregation.

In contrast, peer-to-peer trading with renewable energy is the trade of renewable energy between market participants through a contract with predefined rules that regulate the automatic execution and settlement of the transaction either directly between market participants or indirectly through a certified third market participant, such as an aggregator. Hence, it can be concluded that "peer-to-peer trading" is possible through an EC acting as an aggregator.

However, an EC as an energy producer and an EC as an aggregator represent two distinct operational areas of an EC. In the first case, it involves the production and collective use of renewable energy produced by the community's own production facilities for its members or participants (see European Parliament and Council Directive (EU) 2018/2001). In the second case, the EC has an aggregator function, where through the energy community as an aggregator, the trade of renewable energy produced by active users, who are members of the energy community, takes place. This aligns with the provision in Article 16 of the European Parliament and Council Directive (EU) 2019/944, stating that members or shareholders of a citizen energy community do not lose their rights and responsibilities as household users or active users.

Therefore, a person who has joined an

energy community can have two different roles: they can be a member of the EC, supplied with electricity from production stations within the community, and also an active user who uses the energy community as an aggregator in a peer-to-peer trading model.

5. CONCLUSION

The study of the EC concept is problematic for several reasons. First, different terms are used in scientific literature to denote the same concept. For example, the term "energy community," "energy cooperative," and "community energy project" may all signify essentially the same initiative by residents in the field of energy. Second, the term "energy community" can also be understood to mean conceptually different ideas in various studies.

Regardless of the content of the concept described by the term "energy community", the unifying element is usually the community itself, as well as the goal related to local residents' initiatives in the area of decentralised energy production. Unlike the community's goal, there is a divergent opinion in the literature about the scale of energy communities and their connection to a specific geographical location. Simultaneously, it is entirely possible to agree with the opinion expressed in the literature that there are many conflicting definitions of EC. This is especially significant in discussions about what kind of decentralized energy exchange is associated with peer-to-peer trading and what kind is associated with an EC.

The answer to this question is found by analysing the legal regulation of the EU, namely, the European Parliament and Council Directive (EU) 2019/944 and the European Parliament and Council Directive (EU) 2018/2001. From these legislative acts, it follows that an energy community can have various areas of activity. Among these are the function of an energy producer and the function of an aggregator, which are distinguishable from each other. Therefore, in response to the question of whether a peer-to-peer trading model is possible within the framework of EC, the answer is "yes", but only in relation to the function of the community as an aggregator. Moreover, the energy produced by active users is not considered the energy of the community, i.e., it does not belong to the community.

Conversely, if the question is whether only a peer-to-peer trading model is possible within an EC, without energy production using the community's own production equipment, the answer is "no" because, in such a case, the community will only fulfil an aggregator function.

REFERENCES

1. Moroni, S, Alberti, V, Antoniucci, V, & Bisello, A (2019). Energy Communities in the Transition to a Low-Carbon Future: A Taxonomical Approach and Some Policy Dilemmas. *Journal of Environmental Management*, *236*, 45–53. https://doi.org/10.1016/j.jenvman.2019.01.095
2. De São José, D., Faria, P., & Vale, Z. (2021). Smart Energy Community: A Systematic Review with Metanalysis. *Energy Strategy Reviews*, *36*. https://doi.org/10.1016/j.esr.2021.100678

3. Brummer, V. (2018). Community Energy – Benefits and Barriers: A Comparative Literature Review of Community Energy in the UK, Germany and the USA, the Benefits it Provides for Society and the Barriers it Faces. *Renewable and Sustainable Energy Reviews*, *94*. 10.1016/j.rser.2018.06.013
4. Coenen, F. H. J. M., & Hoppe, T. (2021). Renewable Energy Communities as a New Actor in Home Energy Savings. *Urban Planning*, *7*, 108–122. 10.17645/up.v7i2.5088.
5. Chan, H., Zeng, K. & Yang, Morgan. (2022). Review platforms as prosumer communities: theory, practices and implications. *European Journal of Marketing*, *56*. 10.1108/EJM-10-2021-0819.
6. Wuebben, D., Romero-Luis, J., & Gertrudix, M. (2020). Citizen Science and Citizen Energy Communities: A Systematic Review and Potential Alliances for SDGs. *Sustainability*, *12*, 10096. https://doi.org/10.3390/su122310096
7. Barbour, E., Parra, D., Awwad, Z., & Gonzalez, M.C. (2018). Community Energy Storage: A Smart Choice for the Smart Grid? *Applied Energy*, *212*, 489–497. https://doi.org/10.1016/j.apenergy.2017.12.056
8. Gorroño-Albizu, L., Sperling, K., & Djørup, S. (2019). The Past, Present and Uncertain Future of Community Energy in Denmark: Critically Reviewing and Conceptualising Citizen Ownership. *Energy Research Social Science, 57,* 101231. https://doi.org/10.1016/j.erss.2019.101231
9. Wirth, S. (2014). Communities Matter: Institutional Preconditions for Community Renewable Energy. *Energy Policy*, *70*, 236–246.
10. Eagle, R., & Jones, A. (2017). Localism and the Environment: A Critical Review of UK Government Localism Strategy 2010–2015. *Local Economy, 32* (1), 55–72, https://doi.org/10.1177/0269094216687710
11. Petersen, J.P. (2016). Energy Concepts for Self-Supplying Communities Based on Local and Renewable Energy Sources: A Case Study from Northern Germany. *Sustainable Cities and Society*, *26*. 10.1016/j.scs.2016.04.014
12. Laicāns, M., Amoliņa, I., Geipele, I., Zeltiņš, N., & Greķis, A. (2018), Heat Cost Allocation in Multi-Apartment Buildings: A Literature Review. *Latvian Journal of Physics and Technical Sciences*, *55* (5), 26–35. DOI:10.2478/lpts-2018-0033
13. Walker, G., & Devine-Wright, P. (2008). Community Renewable Energy: What Should it Mean? *Energy Policy, 36*, 497–500. 10.1016/j.enpol.2007.10.019
14. Cuenca, J.J., Jamil, E., & Hayes, B. (2021). State of the Art in Energy Communities and Sharing Economy Concepts in the Electricity Sector. *IEEE Transactions on Industry Applications*. 10.1109/TIA.2021.3114135
15. Amato, A., Ciocia, A., Garello, E., Malgaroli, G., & Spertino, F. (2022). *Hourly Simulation of Energy Community with Photovoltaic Generator and Electric Vehicle*. 10.1109/EEEIC/ICPSEurope54979.2022.9854521
16. Scarcello, L., Giordano, A., Mastroianni, C., & Spezzano, G. (2022). Cascade Computing Model to Optimize Energy Exchanges in Prosumer Communities. *Heliyon*, *8*, e08902. 10.1016/j.heliyon.2022.e08902
17. Savickis, J., Zemite, L., Bode, I., & Jansons, L. (2020). Natural Gas Metering and its Accuracy in the Smart Gas Supply Systems. *Latvian Journal of Physics and Technical Sciences*, *57* (5), 39–50. DOI: 10.2478/lpts-2020-0026
18. Savickis, J., Zemite, L., Zeltins, N., Bode, I., Jansons, L., Dzelzitis, E., … & Ansone, A. (2020). The Biomethane Injection into the Natural Gas Networks: The EU's Gas Synergy Path. *Latvian Journal of Physics and Technical Sciences*, *57* (4), 34–50. DOI: 10.2478/lpts-2020-0020
19. Jansons, L., Bode, I., Zemite, L., Zeltins, N., Geipele, I., & Kiesners, K. (2022). Securing Sustainable Energy Future: Green Hydrogen as a Part of Gaseous Fuel Diversification Risk Management Strategy. *Latvian Journal of Physics and Technical Sciences*, *59* (4), 53–70. DOI: 10.2478/lpts-2022-0033

20. Jansons, L., Silina, J., Bode, Zemite, L., Zeltins, N., & Palkova, K. (2024). Injection of Renewables Gases into the Existing Gas Distribution Grids and Employment of Reverse Gas Flow Technique. *Latvian Journal of Physics and Technical Sciences, 61* (2), 66–79. https://doi.org/10.2478/lpts-2024-00313
21. Zemite, L. Jansons, L., Zeltins, N., Lapuke, S., & Bode, I. (2023). Blending Hydrogen with Natural Gas/Biomethane and Transportation in Existing Gas Networks. *Latvian Journal of Physics and Technical Sciences, 60* (5), 43–55. https://doi.org/10.2478/lpts-2023-00380
22. Savickis, J., Zemite, L., Jansons, L., Bode, I., Dzelzitis, E., Broks, A., & Vempere, L. (2020). The Development of the Smart Gas Distribution: General Trends and the Latvian Context. *Latvian Journal of Physics and Technical Sciences*, *57* (6), 23–39. DOI: 10.2478/lpts-2020-0031
23. Zemite, L., Nevercika, E., Jansons, L., Bode, I., Koposovs, A., Kondrahins, N., & Jasevics, A. (2021). The Natural Gas Supply of the Latvian Municipality during the Local Energy Crisis. *Latvian Journal of Physics and Technical Sciences*, *58* (3), 186–200. DOI: 10.2478/lpts-2020-0025
24. Lazdins, R., & Mutule, A. (2023). Impact of variable factors on the viability and efficiency of energy communities: A scenario simulation study in Latvia. *In IEEE 64th International Scientific Conference on Power and Electrical Engineering of Riga Technical University (RTUCON 2023)*, (pp. 1–5). 9 October 2023, Riga, Latvia. doi:10.1109/RTUCON60080.2023.10413190
25. Di Lorenzo, G., Martirano, L., Araneo, R., Cappello, L., Giorgio Mingoli, G., & Franco Ermellino, F. (2021). Democratic power sharing in renewable energy communities: Engaging citizens for sustainable energy transition. In *2021 IEEE International Conference on Environment and Electrical Engineering and 2021 IEEE Industrial and Commercial Power Systems Europe (EEEIC / I&CPS Europe)*, (pp. 1–6). 7–10 September 2021, Bari, Italy. 10.1109/EEEIC/ICPSEurope51590.2021.9584606
26. Lebedeva, K., Krumins, A., Tamane, A., & Dzelzitis, E. (2021). Analysis of Latvian Households' Potential Participation in the Energy Market as Prosumers. *Clean Technologies*, *3* (2), 437 –449. https://doi.org/10.3390/cleantechnol3020025
27. Aruta, G., Ascione, F., Bianco, N., Bindi, L., De Rossi, F., & Manniti, G. (2023). From consumers to prosumers: The rise of Energy Communities and their role in the energy transition. In *8th International Conference on Smart and Sustainable Technologies (SpliTech)*, (pp. 1–6). Split/Bol, Croatia. doi: 10.23919/SpliTech58164.2023.10193292
28. Ciobanu, I., Lazaroiu, G.C., & Fulginei, F.R. (2023). Energy community part of smart city. In *2023 IEEE International Smart Cities Conference (ISC2),* (pp. 1–7).
29. Löbbe, S., Hackbarth, A., Stillahn, T., Pfeiffer, L., & Rohbogner, G. (2020). Customer Participation in P2P Trading: A German Energy Community Case Study. *Behind and Beyond the Meter*, 83–104. 10.1016/B978-0-12-819951-0.00004-9
30. Hahnel, U.J.J., Herberz, M., Pena-Bello, A., Parra, D., & Brosch, T. (2020), Becoming Prosumer: Revealing Trading Preferences and Decision-Making Strategies in Peer-To-Peer Energy Communities. *Energy Policy*, *137*. 10.1016/j.enpol.2019.111098
31. De Almeida, L., Cappelli, V., Klausmann, N., & Henri van Soest, H. (2021). *Peer-to-Peer Trading and Energy Community in the Electricity Market – Analysing the Literature on Law and Regulation and Looking Ahead to Future Challenges.* Robert Schuman Centre for Advanced Studies Research Paper No. RSCAS 2021/35. http://dx.doi.org/10.2139/ssrn.3821689 10.13140/RG.2.2.29089.22888
32. Upītis, M., Amoliņa, I., Geipele, I., & Zeltiņš, N. (2020). Measures to Achieve the Energy Efficiency Improvement Targets in the Multiapartment Residential Sector. *Latvian Journal of Physics and Technical Sciences*, *57* (6), 40–52. doi:10.2478/lpts-2020-0032

sciendo

LATVIAN JOURNAL OF PHYSICS
AND TECHNICAL SCIENCES
2024, N 3

DOI: 10.2478/lpts-2024-0021

RECONSTRUCTION OF ELECTROPHYSICAL PARAMETER DISTRIBUTION DURING EDDY CURRENT MEASUREMENTS OF STRUCTURAL FEATURES OF PLANAR METAL OBJECTS

V. Ya. Halchenko, R. Trembovetska, V. Tychkov*, N. Tychkova

Instrumentation,
Mechatronics and Computer Technologies Department
Cherkasy State Technological University,
Blvd. Shevchenka, 460, 18006, Cherkasy, Ukraine
*e-mail: v.tychkov@chdtu.edu.ua

The paper proposes a method of simultaneous reconstruction of the electrical conductivity and magnetic permeability profiles of planar metal research objects based on the results of single measurements by eddy current probes using surrogate optimization techniques in a reduced compact subspace design and accumulating the full amount of the most important a priori information about the modes of electromagnetic objects. In addition to the information on the response of probe signals to changes in electrophysical parameters, a priori information includes the data on multifrequency sensing and changes in the lift-off between metal research objects and eddy current probes. All the main stages for the implementation of the method of solving the inverse problem are demonstrated, namely, creating a uniform computer quasi-design of the experiment with improved 2D-projections based on LP_τ-Sobol's sequences; creating surrogate models on fully connected deep neural networks; reducing the dimensionality of the full design space using the principal components method of PCA; reconstructing profiles as a result of surrogate optimisation in a compact subspace. Numerical examples of the method are also presented in the paper.

Keywords: *compact design subspace, eddy current measurements, planar metal research object, profiles of electrophysical parameters, surrogate optimisation.*

1. INTRODUCTION

As a result of various physical factors acting on metal research objects (MRO), such as temperature, deformation, chemical, and other influences, a certain modification of the properties of their sub-surface zone is observed due to changes in the microstructure. This effect is widely used in engineering applications, such as diagnosing critical conditions of industrial equipment, technological operations for strengthening the surface of metal products, etc. Determination of the electrical conductivity (EC) and magnetic permeability (MP) distributions, which are structure-sensitive electrophysical parameters, at a shallow depth from the surface of metal products, i.e., EC and MP profiles, allows tracking the changes in the mechanical properties of the MROs on the basis of appropriate correlations. It is advisable to use non-destructive testing methods for this purpose, namely, the eddy current method. The method is based on the process of the electromagnetic excitation field interaction with the controlled MRO when it penetrates into the depth and the subsequent registration of the total field due to the result of the mutual influence of the secondary field generated by eddy currents in the MRO and the primary field in the form of the induced EMF in the pick-up coil of the surface transformer probe. Thus, the simultaneous reconstruction of the electrophysical parameter profiles based on eddy current measurements is an urgent problem that can be classified as an inverse problem and whose solution is of scientific interest with a given accuracy.

Parametric nonlinear optimisation, which consists in reconstruction of the EC and MP distributions by minimising the discrepancies in a least-squared sense between the measured values of the probe EMF and the calculated theoretical values obtained by solving the direct problem, is the most common approach to solving the issue. The computational process depends on the complexity of the target function, since it requires a significant number of iterations of the direct solver. It becomes a substantial problem with a "heavy" computationally intensive forward direct model.

Methods of local, in particular the ones with gradients for extremum search, and global optimisation [1], [2], were used in the problems with the electrophysical parameter profiles. Their thorough review is given in [3]. Some applications of local optimisation methods are reported in [4], the peculiarity of which is the use of forward and adjoint methods to calculate the Jacobian matrix. To improve the search capabilities of local optimization methods, various modifications are used, for example, in [5], the Newton-Raphson method with regularization and the use of an unmodified sensitivity matrix is proposed to solve ill-posed and ill-conditioning problems, which makes it possible to eliminate the ill-conditioning of computation during the process of reconstruction and to meet the requirements for calculation accuracy.

However, the use of global extremum search methods [6], which find the minimum of a multimodal target function of complex topography in hyperspace in a small number of iterations without strict requirements for the points of initial approximation, proves to be more promising for this purpose. The most famous representative of this class of algorithms is the bioinspired stochastic evolutionary genetic GA. A significant number of algorithms of this class based on metaheuristics are also widely used in practice.

Surrogate optimisation is used for

cases of time-consuming target functions of optimisation algorithms, which are typical for the tasks of determining the EC and MP profiles, which consists in replacing of “heavy” functions with their high-performance alternatives, namely surrogate models (meta-models) [7].

However, due to the “curse of dimensionality”, the problem becomes more critical as the dimensionality of the design space increases, which is also true for profile reconstruction tasks. The large dimensionality of the space requires the creation of cumbersome meta-models and, as a result, large training samples. Reducing the requirements for the volume and quality of training samples is an effective and promising way to improve surrogate optimisation, since the number of points in the training set for creating a meta-model required to correctly sample the design space increases exponentially with the growth of its dimensionality. In addition, a significant number of variables in the optimization algorithm negatively affects the accuracy of the extremum search. Therefore, it makes sense to improve approaches to determining the EC and MP distributions based on modern efficient optimisation techniques, which allows solving both the problems of using resource-intensive for calculating the target functions and reducing the number of variables in search algorithms, and, accordingly, improving the accuracy of solving extreme problems.

2. RESEARCH METHODOLOGY

The task of reconstructing the EC and MP profiles in the optimisation formulation is to minimise the following target function:

$$F(\boldsymbol{\sigma}, \boldsymbol{\mu}, f, z) = \left(C_{mes} - G_{mod}\right)^2 + \left(D_{mes} - Z_{mod}\right)^2 \to min, \tag{1}$$

where $e_{mes} = C_{mes} + \mathrm{j} \cdot D_{mes}$ is the value of the EMF measured by the eddy current probe (ECP) in the algebraic form of writing a complex number with real C_{mes} and imaginary D_{mes} as its parts; $e_{mod} = G_{mod} + \mathrm{j} \cdot Z_{mod}$ is the theoretical value of the EMF calculated in accordance with the electrodynamic model, which is a mathematical formulation of the direct problem; $\boldsymbol{\sigma}$, $\boldsymbol{\mu}$ are the corresponding vectors of electrophysical parameters that determine the desired profiles; f is the frequency of the electromagnetic field excitation; z is the lift-off between the eddy current probe and the surface of the MRO.

The determination of the electrophysical parameter profiles involves the consideration and use of the forward and inverse problems in combination. The Uzal-Cheng-Dodd-Deeds electrodynamic model [8]–[11] of the direct problem in the analytical form used in this research was created under the following assumptions: MROs are characterised by infinite overall dimensions, the medium is assumed to be linear, homogeneous, and isotropic; the electromagnetic field is excited by an ECP generator coil with a sinusoidal current I varying with an angular frequency $\omega = 2 \cdot \pi \cdot f$; the ECP excitation coil has a rectangular cross-section with finite dimensions, is characterised by a uniform current density across the cross-section i_0 and the number of turns W; the measuring coil has a number of turns w_{mes} and an infinite small cross-section. Usually, the sub-surface zone of the MRO to simulate the continuity of the electrophysical parameter profiles is assumed to be conditionally multilayer. Each layer out of *L* possible is characterised by constant EC and MP parameters, i.e., a piecewise constant approximation of the profiles occurs. The model, due to its matrix representation, allows for the introduction of an arbitrary number of conditional discretization layers for calculations, which makes it versatile and rather convenient for numerical experiments. It appears to be essential for achieving acceptable modeling accuracy. It should be noted that the existing experience of its use by researchers indicates the necessity to discretize the sub-surface zone into several hundred conditional layers. The model piecewise constant representation of the profiles provides the ability to set any law of the EC and MP distribution, which allows the chosen model to consider various variants of measurement cases. In the future, the electrodynamic model will be used in the modified form proposed by Theodoulidis [12] and presented below:

$$e_{\mathrm{mod}} = -j \cdot \omega \cdot w_{mes} \cdot \oint_{Lc} A(P)\,dl_{p}\,, \tag{2}$$

where:

$$A(r_{\delta}, z_{\delta}) = \int_{0}^{\infty} J_1(\kappa r_{\delta}) \cdot [C_s \cdot e^{\kappa z_{\delta}} + D_{ec} \cdot e^{-\kappa z_{\delta}}]\,d\kappa;$$

$$C_s = \frac{\mu_0 \cdot i_0}{2} \cdot \frac{\chi(\kappa r_1, \kappa r_2)}{\kappa^3} \cdot (e^{-\kappa z_1} - e^{-\kappa z_2});$$

$$D_{ec} = \frac{(\kappa \cdot \mu_{t+1} - \lambda_1) \cdot V_{11}(1) + (\kappa \cdot \mu_{t+1} + \lambda_1) \cdot V_{21}(1)}{(\kappa \cdot \mu_{t+1} + \lambda_1) \cdot V_{11}(1) + (\kappa \cdot \mu_{t+1} - \lambda_1) \cdot V_{21}(1)} \cdot C_s;$$

$$i_0 = W \cdot I(r_2 - r_1)^{-1} \cdot (z_2 - z_1)^{-1};$$

$$\chi(x_1, x_2) = \left\{ x_1 \cdot J_0(x_1) - 2 \cdot \sum_{m=0}^{\infty} J_{2m+1}(x_1) \right\} - \left\{ x_2 \cdot J_0(x_2) - 2 \cdot \sum_{m=0}^{\infty} J_{2m+1}(x_2) \right\};$$

$$V(1) = T(1,2) \cdot T(2,3) \cdots T(L-2, L-1) \cdot T(L-1, L);$$

$$T_{11}(t, t+1) = \frac{1}{2} \cdot e^{(-\lambda_{t+1} + \lambda_t)dt} \cdot \left(1 + \frac{\mu_t}{\mu_{t+1}} \cdot \frac{\lambda_{t+1}}{\lambda_t} \right);$$

$$T_{12}(t, t+1) = \frac{1}{2} \cdot e^{(\lambda_{t+1} + \lambda_t)dt} \cdot \left(1 - \frac{\mu_t}{\mu_{t+1}} \cdot \frac{\lambda_{t+1}}{\lambda_t} \right);$$

$$T_{21}(t, t+1) = \frac{1}{2} \cdot e^{(-\lambda_{t+1} - \lambda_t)dt} \cdot \left(1 - \frac{\mu_t}{\mu_{t+1}} \cdot \frac{\lambda_{t+1}}{\lambda_t} \right);$$

$$T_{22}(t, t+1) = \frac{1}{2} \cdot e^{(\lambda_{t+1} - \lambda_t)dt} \cdot \left(1 + \frac{\mu_t}{\mu_{t+1}} \cdot \frac{\lambda_{t+1}}{\lambda_t} \right);$$

$$\lambda_t = \left(\kappa^2 + j \cdot \omega \cdot \mu_0 \cdot \mu_t \cdot \sigma_t \right)^{1/2};$$

$A(r_\delta, z_\delta)$ is the azimuthal component of the vector potential, Wb/m; $\mathbf{V}(1)$ is a matrix containing elements V_{11}, V_{21}; $\mathbf{T}()$ is a matrix with elements $T_{11}()$, $T_{12}()$, $T_{21}()$, $T_{22}()$; $\mu_0 = 4\cdot\pi\cdot10^{-7}$ is the magnetic constant, H/m; μ_t is the relative magnetic permeability of the conditional layer t; $J_0()$, $J_1()$, $J_\text{m}()$ are cylindrical Bessel functions of the first kind of zero, first, and m orders; r_δ, z_δ are the coordinates of the observation point P in the cylindrical coordinate system, m; $(r_2–r_1)$ is the width of the cross-section of the ECP excitation coil, m; $(z_2–z_1)$ is the height of the cross-section of the ECP excitation coil, m; Lc is the contour of the ECP measuring coil.

The authors created a program code that implements the electrodynamic model in the MathCAD 15 environment. It was verified by numerical calculations by the finite element method for a three-layer MRO in the COMSOL Multiphysics environment using the AC/DC Module [13]. The maximum relative error in determining the vector potential was no more than 0.2 % in amplitude and 0.5 % in phase. Also, additional testing was performed by comparing with the calculations based on analytical models obtained for one- and two-layer MROs [14], which demonstrated significantly higher accuracy rates. Finally, we tested the experimental data presented in [15] for the magnetic induction vector in the centre and below the ECP excitation coil obtained by A. Philippe [16] and K. Kawashima [17], which proved the adequacy of the solution of the direct problem by the created software.

Using the electrodynamic model (2), the theoretical values of the ECP EMF are calculated, which are used in the target function (1). However, it leads to significant problems in the operation of the optimization algorithm due to the significant time spent on even once calculating e_{mod} values. Therefore, in accordance with the idea of surrogate modelling, this model needs to be replaced by a computationally efficient alternative, namely, a meta-model that approximates the “exact” electrodynamic model with high accuracy. That is, formula (1) is transformed to form (3):

$$F(\boldsymbol{\sigma},\boldsymbol{\mu},f,z) = \left(C_{mes} - G_{metamod}\right)^2 + \left(D_{mes} - Z_{metamod}\right)^2 \rightarrow min, \tag{3}$$

where $e_{metamod} = G_{metamod} + \text{j}\cdot Z_{metamod}$ is the theoretical value of the EMF calculated using a neural network proxy-model (meta-model) for the electrodynamic model.

A deep fully connected neural network (DFCNN) serves as an approximator in these studies, which, due to its outstanding generalization capability, is a modern universal tool for performing the relevant tasks. In addition to its high computational performance, the meta-model serves as a storage device for information about the MRO obtained by preliminary modelling in accordance with the created design of experiment (DOE) in various modes of eddy current measurements. An essential feature of this research is that the meta-model takes into account all the factors that mostly affect the formation of the ECP output signal. These undoubtedly include the vectors $\boldsymbol{\sigma}$ and $\boldsymbol{\mu}$ of the electrophysical parameters, and additional factors, in particular, the frequency of the electromagnetic excitation field frequency f and the lift-off z between the ECP and the MRO surface. Since the ECP output signal is characterised by certain values of amplitude and phase in the exponential form, it is necessary to use a complex-valued neural network, whose inputs are real numbers and whose output is complex. For simplicity, it is advisable to replace the complex-valued neural network by splitting it into two real-valued ones with common inputs. It is useful to consider the outputs of each of the two networks as the real and imaginary parts of the EMF of the ECP, respectively, which eliminates the inconvenience of working with relatively small phase values. Given the complex and significantly nonlinear nature of dependence (2), it is justified to use deep learning for neural networks.

Obtaining an accurate meta-model largely depends on the size and quality of the training sample. These requirements can be met if a perfect DOE is used to create it. To effectively implement the profile reconstruction method, the authors created advanced computer uniform DOEs on quasi-Sobol's sequences [18]. Low discrepancy is their advantage over known designs [19]–[21], and most importantly, in two-dimensional projections. It is these properties of the designs that ensure the accuracy of approximation of complex response hypersurfaces in cases where nothing is known a priori about their topographic features. One of the variants of such quasi-DOEs was used in this research.

The minimisation of the target function (3) was performed by a hybrid multi-agent particle swarm optimisation algorithm with evolutionary formation of the swarm composition [22]–[25] with improved search capabilities. It is a global extremum search algorithm which is of stochastic nature and based on metaheuristics. Due to its stochasticity, a series of algorithm runs were performed to improve the accuracy of the calculations, followed by averaging the results, i.e., the multi-start technique was used. However, the search for an extremum was not carried out in the full design hyperspace, but in its compact subspace, which is characterised by a smaller dimensionality while retaining almost all the properties of the full one without critical loss of information. Finding an extremum in the reduced dimension space makes it possible to take full advantage of the benefits of this approach, described earlier in the introduction. The transition from a multidimensional space to a low-dimensional space was performed using the principal component analysis (PCA) [26]. This is a classical statistical method designed to detect the so-called active new orthogonal basis in the full multidimensional space [27]–[29] based on linear transformations. The basis vectors were found by analysing the singular numbers obtained by the SVD decomposition of the Gram matrix, determined for the data of the full design space. The larger the singular number, the more information is contained in the corresponding eigenvector of the Gram matrix, which is included as a component of the new basis. In this case, the components of the basis maximally preserving information about the MRO were chosen. It allows controlling the choice of the dimension of the compact subspace by mens of balancing. The data concentrated in the full space were projected into the new basis, preserving the essential properties of their originals with the minimal loss. An important advantage of PCA is the ability to back-project the solution data into the original full space after optimisation in the reduced subspace, where the electrophysical parameters of distribution are obtained. It should also be noted that the creation of the meta-model in this case is carried out in a compact subspace, which has a positive effect on the cumbersomeness of its structure, i.e., reducing the number of neurons in the input and hidden layers, etc. In addition, the optimization algorithm operates with normalized values, as this condition is mandatory for neural networks. All these factors together contribute to a higher accuracy of the solution.

It should also be noted that to verify

the solution of the inverse problem, it is not necessary to confirm it experimentally with the results of physical measurements. The validity of its solution can be established by conducting numerical experiments on test problems synthesised using solutions to a previously verified direct problem, which is currently the case. Moreover, the synthesised variants of testing problems should be unique and not used at the previous stages of solving the inverse problem.

3. NUMERICAL MODELLING

According to the proposed methodology, one of its stages involves the creation of a computer homogeneous DOE on quasi-Sobol's sequences, which has low discrepancy rates both for the volumetric case and for two-dimensional projections.

In this research, the task of reconstructing the profiles of the EC and MP is carried out using a meta-model taking into account four factors **σ**, **μ**, and *f, z*, so then a combination of LP$_\tau$-sequences ξ_1, ξ_6, ξ_{14}, ξ_{17} is used to implement a multidimensional homogeneous quasi-plan.

Figure 1 shows this type of DOE with improved two-dimensional projections on a unit scale, the numerical values of the point coordinates of which are given in Table 1.

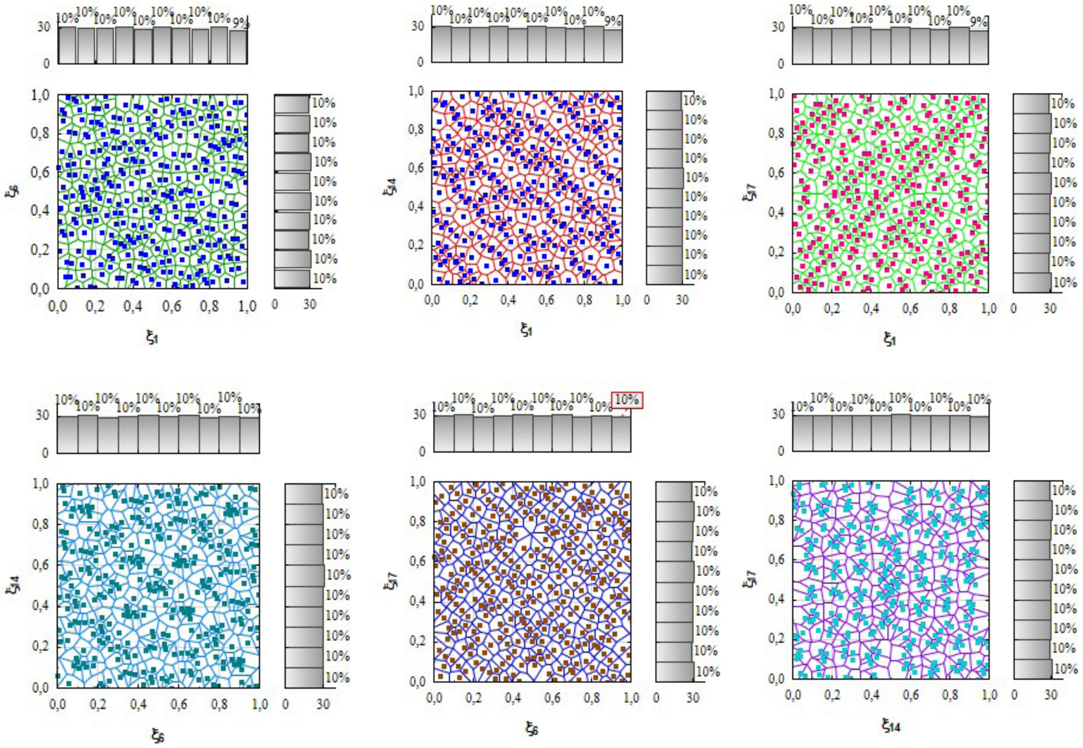

Fig. 1. Visualization of the projections of the experiment design on the LP$_\tau$-sequences ξ_1, ξ_6, ξ_{14}, ξ_{17}.

The total number of DOE points is equal to $N_{profile}$ = 8191, but for the convenience of visualising the DOE homogeneity, only a limited number of them, namely 256, are shown in the figure. A visual analysis of the quality of DOE's 2D-projections using

Voronoi diagrams allows us to assess the degree of their homogeneity by the area of all formed segments. In addition, the homogeneity of the location of points in 2D-projections, even for such a small number of them, is also proved by the coordinate histograms of their distribution. With the number of $N_{profile}$ points, the situation with filling the projection space is even better.

Scaling helps make the transition from a single hyperspace to a real factor space. Initially, before the microstructure changes in the sub-surface zone, the MRO is characterised by the values of the EC σ_{deep} and MP μ_{deep}. When the MRO is exposed to any of the physical factors (temperature, deformation, etc.), the values of the EC and MP change to the maximum on their surface, remaining unchanged at a certain depth of the sub-surface zone. The reconstruction of profiles is performed within some a priori defined limits of their changes relative to the original ones. We will assume that the limits were set within ± 15 % relative to the initial values of the EC and MP on the surface of the MRO. If necessary, these limits can be adjusted.

Table 1 shows the numerical values of the electrophysical parameters μ_{surf} and σ_{surf} on the surface of the MRO at the DOE points in the real four-factor hyperspace. At the same time, point 1, which belongs to the primary profile, is characterised by the values of the EC $\sigma_{deep} = 2 \cdot 10^6$ S/m, $\sigma_{surf} = 9.2 \cdot 10^6$ S/m, and for the MC - $\mu_{deep} = 10$, $\mu_{surf} = 29.78$. Then, taking into account these limits, the ranges of change in the EC parameters on the surface of the MRO will be $7.82 \cdot 10^6 \leq \sigma_{surf} \leq 10.1 \cdot 10^6$ S/m; and for the MP – $24.531 \leq \mu_{surf} \leq 35.028$, with σ_{deep} and μ_{deep} being unchanged for any profile at the depth of the sub-surface zone.

In addition to the values of the electrophysical parameters, the creation of the DOE requires knowledge of the range of changes in the frequency of the electromagnetic excitation field $1 \leq f \leq 20$ kHz, which is informative for observing the signal response at different depths of its penetration, and the lift-off between the ECP and the surface of the MRO, which is taken to be $0.5 \leq z \leq 2.5$ mm.

Table 1. Experimental Design in Four-Factor Space

No point	Design in unit hyperspace				Design in real hyperspace			
	ξ_1	ξ_6	ξ_{14}	ξ_{17}	$\sigma_{surf} \cdot 10^6$, S/m	μ_{surf}	f, kHz	z, m
1	0.5	0.5	0.5	0.5	9.2	29.78	10.5	0.0015
2	0.25	0.75	0.75	0.25	9.89	27.155	15.25	0.001
3	0.75	0.25	0.25	0.75	8.51	32.405	5.75	0.002
4	0.125	0.125	0.125	0.875	8.165	25.8425	3.375	0.00225
5	0.625	0.625	0.625	0.375	9.545	31.0925	12.875	0.00125
…					…	…	…	
8188	0.249878	0.379761	0.497925	0.134644	8.868	27.1539	10.460	0.000769
8189	0.749878	0.879761	0.997925	0.634644	10.248	32.4039	19.960	0.001769
8190	0.499878	0.629761	0.747925	0.384644	9.558	29.7789	15.210	0.001269
8191	0.999878	0.129761	0.247925	0.884644	8.178	35.0289	5.710	0.002269

The laws of distribution of the EC "exponential" and the MP "Gaussian", referring to the typical dependencies determined experimentally in [11], [30] were used as an example, for the model piecewise stable representation of profiles.

Within the specified boundary limits of changes in electrophysical parameters in the real design space (Table 1), we calculated the EC and MP distributions for all DOE points, which corresponds to the number of profiles in the total sample $N_{profile}$ with a sampling of the sub-surface zone $D = 3\cdot10^{-4}$ m by $L = 60$ conditional layers. For the sake of clarity, only some of the obtained profiles are shown in Fig. 2, along with a table that indicates their characteristic parameters.

For these variants of profiles and taking into account the frequency at which measurements are made and the values of the lift-off between the ECP and the MRO, the output signals of the ECP were calculated using the electrodynamic model (2), which are given in Table 2.

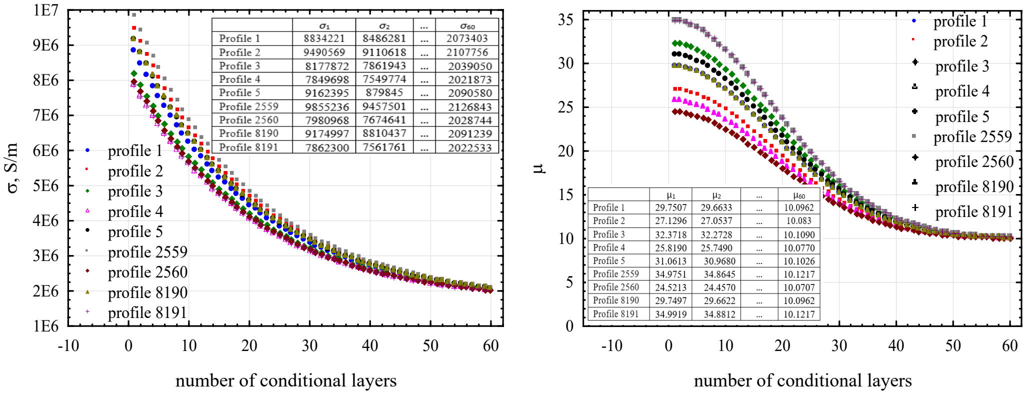

	σ_1	σ_2	...	σ_{60}
Profile 1	8834221	8486281	...	2073403
Profile 2	9490569	9110618	...	2107756
Profile 3	8177872	7861943	...	2039050
Profile 4	7849698	7549774	...	2021873
Profile 5	9162395	879845	...	2090580
Profile 2559	9855236	9457501	...	2126843
Profile 2560	7980968	7674641	...	2028744
Profile 8190	9174997	8810437	...	2091239
Profile 8191	7862300	7561761	...	2022533

	μ_1	μ_2	...	μ_{60}
Profile 1	29.7507	29.6633	...	10.0962
Profile 2	27.1296	27.0537	...	10.083
Profile 3	32.3718	32.2728	...	10.1090
Profile 4	25.8190	25.7490	...	10.0770
Profile 5	31.0613	30.9680	...	10.1026
Profile 2559	34.9751	34.8645	...	10.1217
Profile 2560	24.5213	24.4570	...	10.0707
Profile 8190	29.7497	29.6622	...	10.0962
Profile 8191	34.9919	34.8812	...	10.1217

Fig. 2. MP and EC profiles in the sub-surface zone of the MRO for some of their cases.

Table 2. Training Set 8191×122 for Creating a Meta-model in the Full Factor Space

No profile	Re(e_{mod})	Im(e_{mod})	f, Hz	z, m
1	-2.618	-4.049	10500	0.0015
2	-3.344	-4.34	15250	0.001
3	-1.651	-3.074	5750	0.002
4	-1.082	-2.156	3375	0.00225
5	-3.021	-4.392	12875	0.00125
…				
8188	-2.721	-3.575	10460.1	0.0007692
8189	-3.82	-6.145	19960.1	0.0017692
8190	-3.338	-4.77	15210.1	0.0012692
8191	-1.602	-3.195	5710.1	0.0022692

In this case, the dimension of the factor space is 122, which is significant. Therefore, building a meta-model in such a space is not effective.

Therefore, the next stage of research is the transition to the reduced dimensionality space using the PCA method based on the SVD-decomposition of the Gram matrix created in the previous stage using the training set. The analysis of the obtained singular numbers allowed us to select 63 most influential eigenvectors for which the eigenvalues are greater than 1. Thus, to train the DFCNN, we use a matrix of parameters in a low-dimensional factor space of size $N_{profile} \times n_{red}$, where $n_{red} = 63$ is the number of basis vectors **g** in the new space (Table 3). The total number of samples in the selection was distributed in the following ratio: N_{traine} = 4209 for training, $N_{NN\text{-}test}$ = 904 for testing, and N_{CV} = 904 for cross-validation. The remaining 2177 samples were not used in training, but some of them were later used as synthesised data to check the reliability of the solution to the inverse profile reconstruction problem.

Table 3. Training Set of 8191×63 for Creating a Meta-model in Low-dimensional Factor Space

No point	g_1	g_2	…	g_{62}	g_{63}
1	-34344006	-40876.45	…	-0.2349043	0.0011182417
2	-36406779	469672.51	…	0.4565146	0.0013578367
3	-32281232	-551426.58	…	0.2288428	-0.00084519701
4	-31249845	-806701.24	…	0.2274442	0.00081916363
5	-35375392	214397.8	…	0.2335731	-0.00072947157
…	…	…	…		
8188	-33352224	-286351.94	…	0.6077515	-0.00050085944
8189	-37477772	734747.26	…	0.2040051	0.00094150458
8190	-35414998	224197.78	…	0.0311096	-0.0005216811
8191	-31289451	-796901.49	…	-0.1805091	-0.00094330238

As mentioned in the previous section, further construction of meta-models is carried out by means of deep learning neural networks, for which the outputs of each of the two networks are, respectively, the real and imaginary parts of the ECP EMF, and the inputs are the matrix of **g**-parameters. As a result, we obtained the deep networks Re-MLP-16-17-15-11-1 and Im-MLP-16-17-16-11-1 with four hidden layers for the real and imaginary parts of the EMF, respectively. The validity of the obtained meta-models was assessed by: histograms of residuals (Figs. 3 a, 4 a); Normal P-Plot of residuals (Figs. 3 b, 4 b); scatter plots (Figs. 3 c, 4 c) and $\text{MAPE}_{\text{metamod}}$ errors, % (Mean Absolute Percentage Error) separately for training, cross-validation and test samples; Box-plots (Figs. 3 d, 4 d).

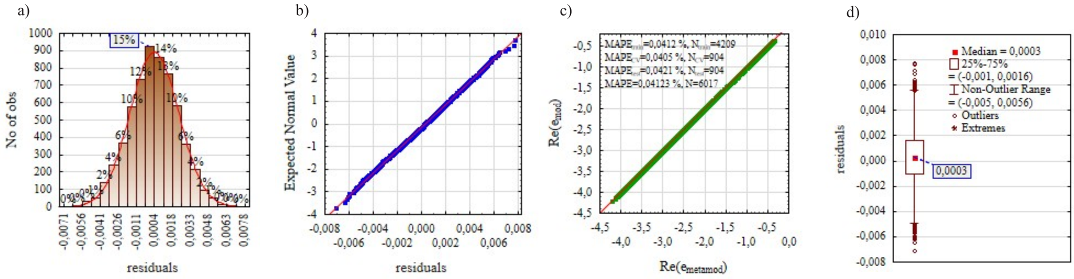

Fig. 3. Statistical assessment of the quality of the Re-MLP-16-17-15-11-1 meta-model:
a – histogram of the residuals distribution; b – Normal P-Plot of the residuals;
c – scatter plot; d – box plot.

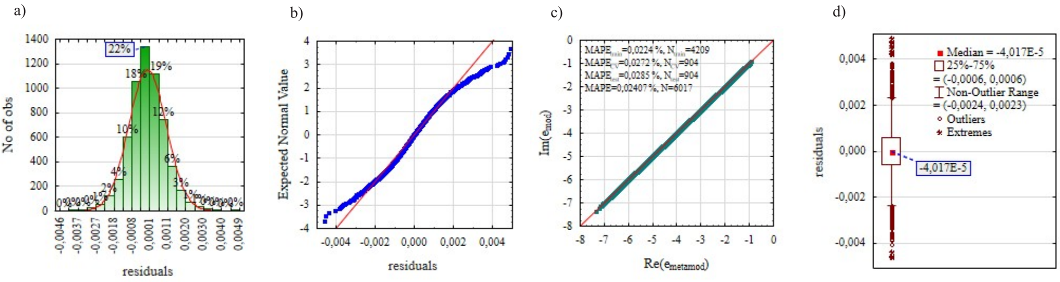

Fig. 4. Statistical assessment of the quality of the meta-model Im-MLP-16-17-16-11-1: a – histogram of the residuals distribution; b – Normal P-Plot; c – scatter plot; d – box plot.

A preliminary assessment of the adequacy of the created meta-models was performed by testing the hypothesis of the normality of the distribution of residuals according to the criteria of skewness and kurtosis with an assessment of the reliability of the obtained coefficients by Student's t-test.

In addition, according to the numerical indicators of the coefficient of determination and Fisher's *F*-ratio $F_{\nu_D;\nu_R}^{total} = {MS_D}/{MS_R}$, where MS_D is the mean square of the regression, MS_R is the mean square of the residuals (ν_D = 63, ν_R = 6017-63-1 = 5953), the informativeness and adequacy of the created meta-models (Table 4) were tested at the level of significance of 5 %.

Both of the created meta-models are adequate, since the calculated model values of the Fisher's criterion for them significantly exceed its critical value. The high informativeness of the created meta-models is also indicated by a significant coefficient of determination, which is significantly reliable according to Fisher's criterion at the level of 5 %.

Table 4. The Verification of the Adequacy and Informativeness of Meta-models

Parameters	Meta-models	
	Re-MLP-16-17-15-11-1	Im-MLP-16-17-16-11-1
Adequacy with ν_D = 63, ν_R = 5953, α = 5 %	$F_{63;5953}^{total} = 7.279 \cdot 10^8$ $F_{0.05;63;5953}^{table} = 1.312$	$F_{63;5953}^{total} = 1.789 \cdot 10^8$ $F_{0.05;63;5953}^{table} = 1.312$
Informativeness	$R^2 = 0.9999$; $F_{63;5953}^{total} = 7.285 \cdot 10^7$	$R^2 = 0.999999$; $F_{63;5953}^{total} = 1.7893 \cdot 10^8$

The inverse problem was solved using a metaheuristic stochastic global optimisation algorithm, namely, a hybrid multiagent particle swarm optimisation algorithm with evolutionary formation of the swarm composition, the effectiveness of which has been proven in [31], [32]. To raise the accuracy of solutions, the multi-start technique was used in the research. Thirty-nine solutions were obtained by a series of starts of the optimisation algorithm, and inverse transformations were performed from the PCA space of the principal components to the primary space and the actual MP and EC profiles were obtained for four test measurements of the EMF.

The bounds within which the MAPE errors of the profiles in thirty-nine starts are obtained are given in Table 5, and Fig. 5 shows the percentage distribution of these errors in the range from minimum to maximum for one *Test 1* measurement as an example.

The reconstructed EC and MP profiles

are finally obtained by averaging the profile variants for each test measurement. Table 6 shows the values of the original and reconstructed profiles and the MAPE, % error, for four test measurements.

Table 5. Ranges of Change in MAPE Error of Reconstruction of Profile Variants

Parameters		Measurements			
		Test 1	*Test 2*	*Test 3*	*Test 4*
Re(e_{mes})		-0.58	-1.094	-1.609	-2.557
Im(e_{mes})		-1.236	-2.045	-2.641	-3.827
f, Hz		1533.52	3205.9	5098.3	9599.4
z, mm		1.065	1.086	1.0446	1.0068
MAPE$_\mu$, %	min	0.154	0.324	0.138	0.235
	max	9.255	8.483	8.874	6.75
MAPE$_\sigma$, %	min	0.248	0.17	0.198	0.322
	max	4.258	4.824	5.62	3.854

Table 6. Reconstructed MP and EC Profiles Based on the Results of Averaging

Parameters		Conditional layers				
		1	2	…	59	60
Test 1	μ_{test1}	30.31168	30.22174		10.11804	10.09899
	μ_{recon1}	30.23665	30.14696		10.10688	10.08789
	MAPE$_\mu$,%	0.178				
	$\sigma_{test1}\times10^6$, S/m	8.277112	7.956343		2.061894	2.044244
	$\sigma_{recon1}\times10^6$, S/m	8.254753	7.934985		2.058932	2.041337
	MAPE$_\sigma$,%	0.204				
Test 2	μ_{test2}	34.63338	34.52431		10.14316	10.12005
	μ_{recon2}	34.76038	34.65093		10.18557	10.16238
	MAPE$_\mu$,%	0.391				
	$\sigma_{test2}\times10^6$, S/m	7.782724	7.486066		2.034691	2.018368
	$\sigma_{recon2}\times10^6$, S/m	7.759168	7.464006		2.040130	2.023889
	MAPE$_\sigma$,%	0.157				
Test 3	μ_{test3}	30.96801	30.87516		10.12185	10.10219
	μ_{recon3}	30.89312	30.80050		10.0945	10.07488
	MAPE$_\mu$,%	0.256				
	$\sigma_{test3}\times10^6$, S/m	7.890392	7.588483		2.040615	2.024003
	$\sigma_{recon3}\times10^6$, S/m	7.858705	7.558117		2.034522	2.017983
	MAPE$_\sigma$,%	0.347				
Test 4	μ_{test4}	30.9439	30.85115		10.12171	10.10207
	μ_{recon4}	30.80823	30.71591		10.083898	10.064342
	MAPE$_\mu$,%	0.405				
	$\sigma_{test4}\times10^6$, S/m	7.574084	7.287602		2.023211	2.007448
	$\sigma_{recon4}\times10^6$, S/m	7.564644	7.278311		2.016711	2.000954
	MAPE$_\sigma$,%	0.228				

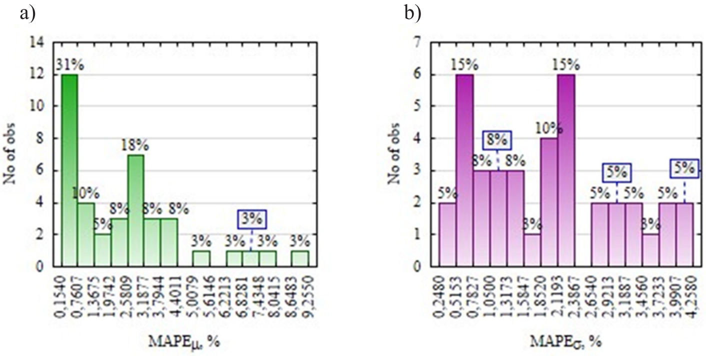

Fig. 5. MAPE error distribution diagrams of reconstructed profile variants for *Test 1* measurement: a – for magnetic permeability; b – for electrical conductivity.

4. DISCUSSION AND CONCLUSION

Studies similar in methodology were performed with a limited number of influential factors in the meta-models taken into account a priori. Thus, in the first case, only two factors were taken into account, namely **μ** and **σ**; and in the second case, three factors **μ**, **σ**, *f* were taken into account, i.e., the multi-frequency mode of ECP operation was considered. In all cases, numerical experiments were performed according to an identical scheme.

The MAPE error of the results of profile identification taking into account only two factors in the active compact space was 0.352 % for the MP profiles and 0.96 % for the EC profiles. When more factors **μ**, **σ**, *f* are taken into account in the meta-model, the following results of profile identification are obtained for the best case: for MP – 0.275 % and for EC – 0.354 %. A decrease in profile reconstruction errors was observed compared to studies where only two factors were taken into account in the meta-models. Model calculations of the reconstruction of the electrophysical parameters of planar MRO's in the presence of a priori information on **μ**, **σ**, *f*, *z* based on the results of direct measurements of the EMF amplitude and phase, which are presented in Table 6, give, in the best case, the MAPE errors for the MP profile – 0.178 %, and for the EC – 0.157 %.

A comparative analysis of the accuracy of the above numerical modelling experiments shows that there is a tendency to improve the results of determining the profiles with an increase in the amount of a priori information about the MRO contained in the meta-models. The best results are demonstrated when the meta-model contains complete information on the most influential factors. It is interesting to note that even with some loss of information caused by the reduction of the design space during optimization, the previously mentioned trend is observed. It is also important to be able to control information losses when reducing the space by making compromise decisions regarding the balance between the size of the space and the accuracy of the problem, which becomes an additional effective means of performing modelling studies to improve the results.

Thus, the studies have convincingly demonstrated the advantages of the proposed method for reconstructing the electrophysical parameter profiles of planar MRO's based on the results of one-time measurements by eddy current probes using surrogate optimisation techniques and accumulating the full volume of the most important a priori information on the modes of electromagnetic research of objects.

REFERENCES

1. Hampton, J., Fletcher, A., Tesfalem, H., Peyton, A., & Brown, M. (2022). A Comparison of Non-linear Optimisation Algorithms for Recovering the Conductivity Depth Profile of an Electrically Conductive Block Using Eddy Current Inspection. *NDT & E International*, *125*, 102571.
2. Cui, Z., Wang, Q., Xue, Q., Fan, W., Zhang, L., Cao, Z., ... & Yang, W. (2016). A Review on Image Reconstruction Algorithms for Electrical Capacitance/Resistance Tomography. *Sensor Review*, *36* (4), 429–445.
3. Xia, Z., Huang, R., Chen, Z., Yu, K., Zhang, Z., Salas-Avila, J. R., & Yin, W. (2022). Eddy Current Measurement for Planar Structures. *Sensors*, *22* (22), 8695.
4. Tesfalem, H., Hampton, J., Fletcher, A. D., Brown, M., & Peyton, A. J. (2021). Electrical Resistivity Reconstruction of Graphite Moderator Bricks from Multi-Frequency Measurements and Artificial Neural Networks. *IEEE Sensors Journal*, *21* (15), 17005–17016.
5. Lu, M. (2018). *Forward and Inverse Analysis for Non-destructive Testing Based on Electromagnetic Computation Methods*. The University of Manchester (United Kingdom).
6. Liu, G. R., & Han, X. (2003). *Computational Inverse Techniques in Nondestructive Evaluation*. CRC press.
7. Jiang, P., Zhou, Q., Shao, X., Jiang, P., Zhou, Q., & Shao, X. (2020). *Surrogate-Model-Based Design and Optimization* (pp. 135–236). Springer Singapore.
8. Zhang, J., Yuan, M., Xu, Z., Kim, H. J., & Song, S. J. (2015). Analytical Approaches to Eddy Current Nondestructive Evaluation for Stratified Conductive Structures. *Journal of Mechanical Science and Technology*, *29*, 4159–4165.
9. Lei, Y. Z. (2018). General Series Expression of Eddy-Current Impedance for Coil Placed above Multi-Layer Plate Conductor. *Chinese Physics B*, *27* (6), 060308.
10. Bowler, N. (2019). *Eddy-Current Nondestructive Evaluation*. New York: Springer.
11. Uzal, E. (1992). *Theory of Eddy Current Inspection of Layered Metals*. Iowa State University.
12. Theodoulidis, T. P., & Kriezis, E. E. (2006). Eddy Current Canonical Problems (with Applications to Nondestructive Evaluation). 107503116
13. Trembovetska, R., Halchenko, V., & Bazilo, C. (2022, June). Inverse multi-parameter identification of plane objects electrophysical parameters profiles by eddy-current method. In *International Conference on Smart Technologies in Urban Engineering* (pp. 202–212). Cham: Springer International Publishing.
14. Halchenko, V., Trembovetska, R., Bazilo, C., & Tychkova, N. (2022, June). Computer simulation of the process of profiles measuring of objects electrophysical parameters by surface eddy current probes. In *International Scientific-Practical Conference "Information Technology for Education, Science and Technics"* (pp. 411–424). Cham: Springer Nature Switzerland.
15. Dodd, C. V., & Deeds, W. E. (1975). *Calculation of Magnetic Fields from Time-Varying Currents in the Presence of Conductors* (No. ORNL-TM-4958). Oak Ridge National Lab. (ORNL), Oak Ridge, TN (United States).
16. Philippe, A. (1969). *Contrôle non destructif par courants de Foucault*. Contribution à l'étude de l'influence de la forme des sondes bobinées sur la distribution spatiale de'induction magnétique. EUR 4284.

17. Kawashima, K. (1975). *Electromagnetic Ultrasonic Transducer* (No. ORNL-5063). Oak Ridge National Lab (ORNL), Oak Ridge, TN (United States).
18. Halchenko, V., Trembovetska, R., Tychkov, V., & Tychkova, N. (2023). Construction of Quasi-DOE on Sobol's Sequences with Better Uniformity 2D Projections. *Applied Computer Systems*, *28* (1), 21–34.
19. Wang, Y., Sun, F., & Xu, H. (2022). On Design Orthogonality, Maximin Distance, and Projection Uniformity for Computer Experiments. *Journal of the American Statistical Association*, *117* (537), 375–385.
20. Fang, K., Liu, M. Q., Qin, H., & Zhou, Y. D. (2018). *Theory and Application of Uniform Experimental Designs* (Vol. 221). Singapore: Springer.
21. Ping, H., Lin, D. K., Min-Qian, L., Qingsong, X., & Yongdao, Z. (2020). Theory and Application of Uniform Designs. *Scientia Sinica Mathematica*, *50* (5).
22. Halchenko, V. Y., Yakimov, A. N., & Ostapuschenko, D. L. (2010). Global Optimum Search of Functions with Using of Multiagent Swarm Optimization Hybrid with Evolutional Composition Formation of Population. *Information Technology*, *10*, 9–16.
23. Halchenko, V. Y., Trembovetska, R. V., Tychkov, V. V., & Storchak, A. V. (2019). Nonlinear Surrogate Synthesis of the Surface Circular Eddy Current Probes. *Przegląd elektrotechniczny*, *9*, 76–82.
24. Kuznetsov, B., Bovdui, I., & Nikitina, T. (2021, February). Optimal design of system of active shielding of magnetic field generated by overhead power lines. In *2021 IEEE 16th International Conference on the Experience of Designing and Application of CAD Systems (CADSM)* (pp. 1–4). IEEE.
25. Koshevoy, N. D., & Beliaieva, A. A. (2017). Application of Particle Swarm Optimization of Composite Second Order Plans. *Radioelectronic and Computer Systems*, *1*, 69–75.
26. Géron, A. (2022). *Hands-on Machine Learning with Scikit-Learn, Keras, and TensorFlow*. O'Reilly Media, Inc.
27. Wang, J., Zhou, J., & Chen, X. (2022). *Data-Driven Fault Detection and Reasoning for Industrial Monitoring*. Springer Nature.
28. Géron, A. (2017). *Deep Learning avec TensorFlow*. Dunod.
29. Raschka, S. (2017). *Machine Learning*. Packt.
30. Galchenko, V. Y., Koshevoy, N. D., & Trembovetskaya, R. V. (2022). Homogeneous Plans of Multi-Factory Experiments on Quasi-Random R-Roberts Sequences for Surrogate Modeling in a Vortex Style Structuroscopy. *Radio Electronics, Computer Science, Control*, *62* (3), 22–30.
31. Halchenko, V. Y., Trembovetska, R., & Tychkov, V. (2021). Surrogate Synthesis of Frame Eddy Current Probes with Uniform Sensitivity in the Testing Zone. *Metrology and Measurement Systems*, *28* (3).
32. Halchenko, V. Y., Trembovetska, R. V., & Tychkov, V. V. (2021). Surrogate Synthesis of Excitation Systems for Frame Tangential Eddy Current Probes. *Archives of Electrical Engineering*, *70* (4), 743–757.

LATVIAN JOURNAL OF PHYSICS
AND TECHNICAL SCIENCES
2024, N 3

DOI: 10.2478/lpts-2024-0022

INSTALLATION OF ALTERNATIVE ENERGY SOURCES AND EQUIPMENT IN RESIDENTIAL BUILDINGS IN LATVIA

A. Cimbale*[1], I. Amolina[2], A. Elsts[3], I. Geipele[2], N. Zeltins[4]

[1] Ltd. "Juridiskā koledža"
Kr. Valdemāra Str. 1c, Riga, LV-1010, LATVIA
[2] Riga Technical University,
Institute of Civil Engineering and Real Estate Economics,
6-210 Kalnciema Str., Riga, LV-1048, LATVIA
[3]Ltd "PRO DEV 24"
Drustu Str. 1D, Riga, LV-1002
[4] Institute of Physical Energetics,
14 Dzerbenes Str., Riga, LV - 1006, LATVIA
*e-mail: a.cimbale@inbox.lv

At the end of 2019, the EC presented the European Green Deal – a set of policy initiatives with the ultimate goal of making Europe climate-neutral by 2050. This means that all EU member states must reach climate neutrality. Emissions in all sectors shall be substantially reduced to achieve this goal. Most of the energy is produced using fossil fuels, which contributes to climate change, water and air pollution, as well as the depletion of natural resources. Individual and district heating systems, which supply residential buildings with heat and hot water, are responsible for a part of global emissions.

Electricity generation also produces emissions. The EU recognises the mitigation of climate change as one of the main challenges that must be overcome to ensure sustainable development of the European Union, which is why it has defined ambitious goals to promote decarbonisation and is deliberately moving towards the implementation of renewable energy.

This article aims at analysing the opportunity of using renewable energy resources in multi-apartment residential buildings in the context of sustainability.

Keywords: *Construction costs, energy efficiency, heat pumps, renewable energy sources, renovation of residential buildings, solar panels.*

1. INTRODUCTION

The EU must address the pressing issues of making buildings sustainable, more energy efficient and reducing their carbon footprint throughout the entire life cycle. The application of circular economy principles to building renovation will reduce greenhouse gases (GHG) associated with materials. The EU renovates residential buildings every year, also by implementing the measures associated with the introduction of renewable energy sources. It is more than just a reduction of energy bills and emissions. Renovation can open up many opportunities and bring a wide range of social, environmental and economic benefits. The renovation process may simultaneously introduce several improvements, such as making a building healthier and greener, more accessible and more resistant to extreme natural conditions, connecting it to other neighbourhood buildings, as well as equipping it with recharging points and bicycle stands as a part of the e-mobility concept. In addition, investment in building renovation can boost the construction ecosystem and the economy as a whole. Renovation is a labour-intensive process, which creates jobs and investments that are often rooted in local supply chains; it can also create a demand for energy- and resource-efficient equipment as well as ensure the long-term value of a property.

Based on projections of climate change [1], the current GHG emission mitigation scenario states that the net GHG emissions shall be reduced by 43 % over the next eight years compared to the net GHG emissions in 2019 [1].

The ever-increasing demand for renewable energy sources (RES), the depletion of fossil energy resources and the need to take care of the environment have made the principles of sustainable development one of the focal points for future development. Adherence to and implementation of such policy ensures economic development, increases competitiveness and promotes employment. At the same time, it preserves and does not disrupt the environmental quality.

Modern energy development involves a widespread use of power plants based on RES, such as hydropower, solar, wind, geothermal, tidal, wave, etc. This direction is associated not only with the struggle for carbon neutrality, but also with ensuring the energy security of territories that provide themselves with energy from their own energy resources, and renewable energy sources in one ratio or another are available in any country in the world. However, the modern view of the use of renewable energy sources is mostly related to the gross potential of energy resources [2].

The growing role of renewable energy sources in the world energy balances contributes to a more efficient use of energy resources and their long-term preservation. At the same time, it positively impacts the environmental quality due to a decrease in emissions that pollute the atmosphere and water. Therefore, supporting the development of renewable resources is becoming an increasingly important and urgent task for all countries of the world, including Latvia. Supporting the use of renewable resources has become an essential part of the European Union (EU) policy. Wider use of renewables can make a significant contribution to the energy balances of particular regions as well as Latvia in general. The use of these resources can increase the security of energy supply, especially in regions with less developed energy infrastructure. Successful implementation of RES requires an integrated approach, and the enactment of renewable energy policies will have an impact on many areas of the economy and life in general. The set targets can be achieved only by coordinating and amending existing policies in key sectors of renewable energy sources.

The present article aims to analyse the opportunity of using renewable energy resources in multi-apartment buildings in the context of sustainability.

To achieve the aim, the following tasks have been set:

- to determine the role of renewable energy resources and their function in the context of the climate neutrality policy of the European Union and the development of the national economy of Latvia;
- to carry out a SWOT analysis of the use of alternative energy sources in the building renovation process;
- to analyse the processes of installation and operation of renewable energy equipment in Latvia.

The authors of the research have applied the analytical, statistical, and comparative analysis methods. Since the research topic is vast in scope, the authors have narrowed down the time period to 2017–2022, and the research object – to residential buildings.

2. THE ROLE OF RENEWABLE ENERGY SOURCES

The importance of RES in ensuring sustainable development can be attributed to the positive impact it has on various areas. Using RES can help:

- replace fossil energy sources, diversify and encourage using local resources, thereby increasing energy security and reducing dependence on energy imports;
- reduce the emissions polluting the atmosphere and water;
- promote regional development by creating new jobs, aiding the development of agriculture, forestry, manufacturing and research related to renewable energy technologies.

As investments in renewable energy resources replace the investments in fossil energy resources, a restructuring in the cost of energy production and a shift between economic sectors take place. Currently, the main stimulus for the support of renewable resources in Latvia is the energy security issues, as well as the possible increase in the prices of fossil energy resources in the future. The policy promoting environmental protection and climate change mitigation also acts as a motivational factor [3].

Renewable energy sources are expanding opportunities for industrial development and can boost economic growth and create new jobs. It is possible to use renewable energy resources cost-effectively in all EU countries. The world is now at the beginning of the global energy transformation. Cost-effective renewable energy technologies provided an opportunity for sufficient development to reach ambitious climate targets of the EU Directive 2018/2001 of the European Parliament and of the Council of 11 December 2018 on promoting the use of energy from renewable sources [4].

RES driving forces can be divided into three main groups: economic, environmental and social. Economic drivers that are optimising the energy supply system are the main rationale for the use of renewable energy resources. It is especially topical in areas, where connecting to a centralised electricity grid is troublesome. Often in such cases, opting for the use of renewable resources is cheaper than trying to connect to the grid. Renewable resources can be used in decentralised systems, which reduces the need to expand the existing power distribution network and allows for money savings. Security of supply: since energy consumption continues to increase, and Latvia has limited fossil fuel reserves, it heavily depends on imported energy resources. The use of renewable resources reduces reliance on imported resources, increasing the security of supply. Thus, the country decreases the dependency on fossil fuel price changes, which in turn increases the socio-economic stability of the country. The energy supply security issues are very topical, as proven by recent events in the oil supply sector. Environmental drivers – reducing emissions. The use of renewable energy resources (excluding biomass) does not directly lead to emissions. Generating energy from the wind or the sun energy does not directly cause emissions. The use of biomass and waste does produce emissions; however, they are controlled by pertinent legislation and regulations [3].

Environmental benefits of renewables include less pollution, socio-economic benefits, and increased credibility for renewable energy as ideas are implemented locally and create new work opportunities. Renewable energy, new technological innovations and efficient energy use are the way to meet climate targets set in Directive (EU) 2018/2001 of the European Parliament and the Council of 11 December 2018 on the promotion of the use of energy from renewable sources [5].

RES have a large share in energy production. Energy resources produced in Latvia are fuel wood, electricity from hydro and wind stations, biogas, straw, biodiesel, and bioethanol. Heat plants produce thermal energy by burning not only natural gas but also in some cases oil products, coal and peat.

3. THE OPPORTUNITY OF INSTALLING ALTERNATIVE ENERGY SOURCES AND EQUIPMENT IN RESIDENTIAL BUILDINGS IN LATVIA

In the current economic climate, the characteristics of a house correspond to the financial status of the homeowner and their expense priorities – how high on the list of expense priorities are the expenses associated with housing and how much the homeowner is willing to invest in their property. Nowadays, it is important for housing to be comfortable, economic in terms of maintenance and energy consumption, as well as to be architecturally and aesthetically pleasing and fit into the surrounding environment. There are three possible ways to achieve a significant reduction in energy consumption:

- to carry out renovation of a building;
- to use alternative energy sources in the energy balance of a building;
- to use both renovation and alternative energy options.

Various RES can be used to produce heat and electricity for households, for example, solar, wind energy, biogas, and geothermal energy.

Although GHG emissions currently align with the set GHG reduction targets, it should be noted that the EU actively discusses raising the GHG reduction target for 2030. It is worth noting that if the climate targets are to be raised at the level of the EU, the national targets will have to be raised as well. The results and actual benefits (reduction of emissions and heat energy) of the current state policy promoting the energy efficiency of buildings will only be seen in the coming years. The same applies to renovation projects that are currently being carried out on residential, and non-residential buildings, including factories and public buildings as well as renovation projects that are still pending. Thus, it is projected that the heat consumption in the household sector and GHG emissions will reduce in the coming years.

As stated in the Strategy of Latvia for the Achievement of Climate Neutrality by 2050, the following objectives would be a part of an overarching policy in 2050:

- construction of all new buildings conforms to the requirements of zero-energy buildings. Citizens are aware of the advantages of zero-energy buildings, both in terms of providing energy savings and a healthy indoor microclimate. Strict energy efficiency requirements are applied to the construction of new buildings. By 2050, it is ensured that all new buildings are zero-energy. During the construction of zero-energy buildings, the location of buildings, the materials used, and the internal engineering networks are also carefully considered;
- all renovation and rebuilding projects meet the requirements of zero-energy or nearly zero-energy buildings. Reducing emissions is unattainable without improving the energy efficiency of existing buildings, while also preserving historic buildings. Renovation and rebuilding projects are carried out qualitatively, using sustainable materials as well as effective technologies and methods. All existing buildings have been renovated or rebuilt following energy performance standards. As one of the biggest challenges to date hindering the holistic renovation of buildings, is limited funding, additional financial instruments are introduced [3].

3.1. Solar Batteries

Solar radiation warms the atmosphere, the soil, and bodies of water. The sun's radiation energy is the foundation of all processes occurring on the Earth. Photosynthesis is a biological process of storing solar energy that creates biomass. All fossil energy sources (coal, oil, natural gas) are essentially the converted and stored solar energy from millions of years ago.

The sun's chemical composition is 81.76 % of hydrogen in the gaseous state, 18.14 % of helium, and 0.1 % of nitrogen. Continuous thermonuclear reactions occur inside the sun turning hydrogen into helium and releasing solar radiation. The temperature on the surface and corona of the sun reaches around 5 900–60 000 °C. Passing through the earth's atmosphere, the intensity of solar radiation continuously decreases. On a clear sunny day, the intensity of solar radiation on the surface of the Earth in our region is 800–1 000 W/m^2. The average solar radiation in Latvia is around 130 W/m^2. Within a year, 10 000 times more thermal energy is projected to the earth's surface than people consume. Even in a city centre with high-density housing, the amount of energy used for heating and hot water is five times less than the amount of solar energy emitted annually to this area. It is clear that the solar energy has enormous potential. However, the intensity of solar radiation greatly varies depending on the time of the year. In the European climate, a solar collector can cover most of the hot water consumption in summer [6].

Solar systems use solar radiation rather than heat to generate electricity, so regardless of air temperature, solar panels operate even in cloudy or rainy weather, as well as on sunny winter days, when the outdoor temperature is as low as –20 °C. The part of the electromagnetic radiation of the Sun with a wavelength of 100–400 nm is what we call solar radiation [6].

Since 2021, there has been a considerable increase in the number of solar panels installed on the roofs of residential buildings in Latvia. However, there is an issue which arises from an applied restriction. A low threshold for the production of green energy has been set, restricting the installation of solar batteries above 11 kW for household needs since neither JSC Sadales tīkls nor JSC Augstsprieguma tīkls is capable of transmitting greater amount of power. As a result, renewables cannot be used to their fullest potential and homeowners cannot use the energy the way they would want to.

Solar batteries have the highest efficiency from March to September. During the remaining period – in autumn, spring and winter – only 10 % of the total annual amount of electricity is produced. From November to March, the solar energy potential is minimal and cannot ensure a sufficient, uninterrupted supply of electricity without an additional power source, such as a diesel generator.

To ensure the most efficient operation of a solar power system, it is recommended to make sure that the solar panels are freestanding and installed at an angle that suits the particular region. For example, given the climate conditions of Latvia, panels installed at the wrong angle could contribute to energy losses of about 28 %. If the panels do not have power optimizers, the power of the entire chain decreases if one of the panels is in the shade. Solar panels can be installed on the roof or the ground, and are suitable for all types of surfaces, except for thatched roofs.

In the current environment of high energy prices, many are tempted to try producing their own electricity for their household needs – more and more solar panels appear on the roofs and in the courtyards of Latvian houses. However, the proper maintenance of these panels is crucial. If solar panels are installed on the roof, all fasteners and fixtures holding the structural parts of the panels as well as mounts should be inspected each spring. In winter, the accumulation of snow and ice can affect the functionality of mounting components. If the air temperature fluctuates around 0 degrees, metal fasteners are also affected.

Installing solar panels on a joint property also poses a challenge. The co-owners must agree on several aspects – whether to install the panels on the roof (sloping or flat) or on the parcel of land, what type of equipment to choose, how to cover the installation costs, what type of mounting to use, etc. Solar batteries can produce electrical energy for common use –provide indoor and outdoor lighting, power elevators, pressure boosting systems, etc. At a sufficient capacity, electricity can be supplied not only to common areas but also to individual spaces, for example, apartments, non-residential areas, and workshops. The simplest way to install solar panels on a joint property, besides reaching a collective agreement, is to install the panels or any other unconventional energy-producing equipment during the construction phase if it is proposed by the contractor. However, the apartment owners can also make such a decision. In this case, the benefits of such a solution must be well-defined and the bearing capacity of existing structures or the suitability of the territory of the house must be evaluated. In a densely built city centre, courtyards are not spacious enough and there is a risk that the panels will be shaded by neighbouring houses all the time.

Solar battery suppliers and power companies often offer a calculator of the required area and capacity of the equipment, which takes into account the technical parameters of the particular solution provided by the manufacturer. For example, in a two-section 5-storey house, serial number 464, with 2 staircases and 30 apartments in Riga about 2500 kWh of energy is consumed annually for common use, since there is no elevator and no pump station. While a single apartment consumes about 1200 kWh/year, all apartments together – 36000 kWh/year. In this case, when the roof is flat, 9 panels with a total area of 18 m^2 would be enough to cover the use of electricity in common areas. According to the manufacturer, the power of such a solar system would be 3.69 kW and it would produce more than enough electricity per year – 3 440kWh. If the goal is to cover the entire electrical energy consumption of the building, 37 panels with a total area of 180m^2 are required to provide 38500 kWh/year. Theoretically, there is enough roof area, however placing that many panels would make it difficult to maintain and clean the ventilation system, as well as access electrical cables and low-voltage networks. If the equipment is to be installed on the ground, one would have to consider the area of the available space, and how it is currently used as well as take into account pertinent safety requirements. It is worth noting that the calculations are made supposing that the panels are installed facing the south, which is usually possible on a roof but can often be challenging on the ground, especially in densely built-up areas.

Similar calculations can be applied to an apartment building, which also has two sections, but corresponds to serial number 602, has 2 elevators, and 72 apartments in total. 10000 kWh are consumed annually in common use areas, while apartments use up 86400 kWh/year, provided that again we suppose that the average consumption is 1200 kWh/year per apartment. 25 panels with a total area of 48 m^2 would be enough to cover energy consumption in common use areas. The capacity of such a solar system would be 10.25 kW, and the amount of electricity produced per year would be 9.556 kWh – slightly less than required. To ensure that the entire electrical energy consumption of the building is covered, 236 solar panels with a total area of 251 m^2 would have to be installed. Although the roof on this type of building is also flat, the mass of the entire system would certainly form a considerable load, which should be taken into account and evaluated separately.

Households generating electricity from RES can reduce the cost of electricity and the variable part of the MPC. If the net electricity use during the monthly billing period was negative (the customer transferred more kWh to the distribution system operator than consumed), the accumulated net amount of electricity would be added to the following billing period as the electricity transferred to the electrical power network. On the other hand, if the net use was positive (the customer consumed more kWh than they transferred to the distribution system operator), the kWh accumulated in the previous billing period would be used to compensate it or an additional amount of electricity would be supplied from the power network.

3.2. Heat Pumps

A heat pump is a specialised piece of equipment that is used to produce heat and is subject to all energy-related laws. Like other types of heating systems, the heat pump has its distinct features. However, the laws of thermodynamics in this equipment work in the same way as in refrigerators and conditioning units used in households. The main aspect that differentiates heat pumps from other types of heating systems is that they use the energy of heat sources present in the environment, which is free, however, there must be a certain amount of energy at the input to initiate the thermodynamic cycle. A heat pump is considered efficient if the amount of input energy, usually electric, is smaller than the output energy, i.e., the heat that is produced by operating the equipment. A heat pump is heating equipment that uses solar energy stored in soil, water bodies, groundwater and air.

A heat pump system consists of a heat pump unit that stores heat and prepares hot water, a collector that collects heat from a heat source, and a system that transfers heat to the desired rooms. Currently, the most commonly used type of heat pump is the so-called phase-change heat pump, which operates by circulating freon, which has a low boiling point, in a closed system. Freon can be in either liquid or gaseous state depending on the temperature and pressure.

Modern heat pumps use the latest technologies and materials, which significantly improve their efficiency. Heat pumps also utilize subcooling to lower the temperature before the expansion valve, and a compressor with a higher efficiency [7].

Freons with a low boiling point are used as refrigerants in heat pumps. The most commonly used ones are R404 and R407C as they do not contain chlorine, which is harmful to the environment. The heat required for evaporation is transferred from the heat collector. The cooled liquid is transferred to the utilised heat source (soil, groundwater, body of water, etc.) where it heats up again.

A heat pump diagram intended for heating (or cooling) and simultaneous production of domestic hot water (DHW) is presented in the patent of Mitsubishi Denki Kabushiki Kaisha (US4592206) in 1986. In this configuration, there are three types of heat exchangers: two internal air exchangers, one external air exchanger and a coil exchanger for the DHW production (Fig. 1) [8].

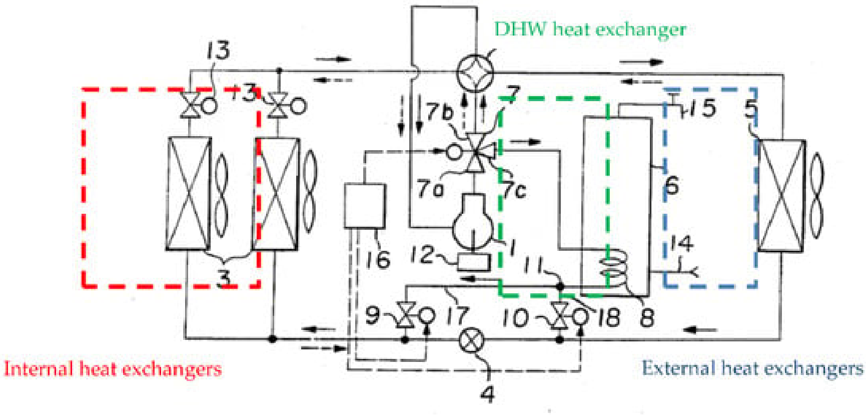

Fig. 1. Schematic diagram of the patent of Mitsubishi Denki Kabushiki Kaisha [8].

A three-way valve at the compressor outlet distributes the vapour, depending on the mode, to the DHW heat exchanger or to a four-way valve. The combination of the two valves allows one to switch between the different operating modes. There are four operating modes:

- Heating only mode (condensation in the internal exchangers and evaporation in the external air exchanger);
- Heating and DHW production mode (condensation in the internal exchangers as well as the coil and evaporation in the external air exchanger);
- Cooling only mode (condensation in the external air exchanger and evaporation in the internal exchangers);
- Cooling and DHW production mode (condensation in the coil and evaporation in the internal exchangers) [7].

The use of heat pumps is topical in the private housing sector in Latvia. There are multiple reasons for that. First, the growing utility bills; second, people have started to think about the environment, how they affect it and how they can protect it. Third, currently, Latvia imports a lot of energy resources. This issue has to be addressed to reduce imports and improve the economy of Latvia. It is not usual in Latvia for heat pumps to be used for the production of energy in heat plants.

3.3. SWOT Analysis

Latvia is facing a major challenge – the use of renewable energy resources in residential buildings holds great potential; however, before initiating any processes associated with the use of renewables, several aspects must be evaluated. The authors of the article have conducted a SWOT analysis, evaluating the strengths and weaknesses of RES.

Strengths:

1. A high share of RES in total energy production. The majority (over 99 %) of the energy resources produced in Latvia is RES – fuel wood, electricity from hydro and wind stations, biogas, straw, biodiesel, and bioethanol. RES play an important role in the production of electricity in Latvia.
2. The share of natural gas used in heat plants for the production of heat energy is less than 54 %, small amounts of oil products (3.8 %), coal (1.1 %) and peat (0.1 %) are also used. The use of woody biomass is in second place after natural gas – about 41 %.
3. The current tendency to use RES and its relatively high share in gross energy consumption [9].
4. The analysis of the situation reveals that the development of renewable energy communities cannot rely solely on citizen investments. Other financial instruments should also be utilised (including investment support programmes and low-interest loans).
5. The most effective incentive to promote the use of renewable resources is the grant programme that is currently implemented to support the reconstruction and increase of efficiency of district heating systems. Its success is indicated by the efficiency of this solution and the positive impact it has on the use of renewable energy. The state and local governments have at their disposal highly qualified specialists with experience in the areas related to the construction and maintenance of residential buildings. Owners of apartments in multi-apartment buildings have access to municipal and state co-financing

for the improvement of the building's energy efficiency.

6. The use of RES and the increase in their share in total energy consumption have a positive impact on the reduction of GHG emissions.
7. According to the Final Report of the Saeima Parliamentary Inquiry Committee on the objectives, impact, criteria for aid implementation, aid intensity, Decision of the European Commission of 24 April 2017 in Case SA.43140 (2015/NN), and damage and action by law enforcement institutions, Latvia's aim was to introduce and subsequently adjust state aid and support mechanisms for electricity producers (including state support programmes for the production of electricity from RES and its use in cogeneration plants).
8. In 2016, the gross energy consumption in Latvia was 184.5 PJ, which was only 0.3 % more than in 2015, while in 2017 it was 194.9 PJ, which was 5.5 % more than in 2016. From 2013 to 2017, the gross energy consumption did not change significantly, but the share of renewables meanwhile increased by 2.55 % [10].
9. Latvia's National Energy and Climate Plan defines the following goals for 2030 – promoting energy independence by increasing self-sufficiency of energy resources and integrating the EU power distribution networks, ensuring sustainable use of energy resources necessary for the development of the national economy, promoting the availability of resource markets, reducing industrial energy consumption and amount of emissions, as well as increasing the share of local renewables in the total amount of consumed energy, while offering competitive energy prices [11].

Weaknesses:

1. The low rate at which the implementation of RES in the electricity sector is developing. Most of the renewable energy – almost 95 % is produced by the cascade of hydroelectric power plants on the Daugava River, which have been operating for several decades, while the remaining part is produced by small hydroelectric power plants, wind power stations, biogas plants, biomass power plants and RES-fuelled CHP plants.
2. In 2017, gross electricity consumption in Latvia amounted to 7500 GWh – 3635 GWh were generated using RES, 873 GWh were imported, while 2992 GWh or almost 40 % of the electricity consumed in the country in 2017 was generated using natural gas. Approximately 80 % of heat energy in the district heating sector is produced by burning natural gas.
3. Flaws in the current RES policy. The current RES energy support scheme has proved to be inefficient, because, despite receiving one of the strongest supports from the EU, the consumption of green energy in Latvia has been growing slowly. Although Latvia has had a relatively wide range of support mechanisms for RES (especially in the electric power sector) for several years now, the share of renewables in gross energy consumption, electricity, and heat generation sector as well as in the transportation sector has been growing very slowly. Biofuel production incentives have aided the development of production sites; however, they have not affected local energy consumption.
4. Inefficient use of RES. The efficiency of a heating plant producing heat energy is less than 80%. Since the efficiency of a natural gas power plant is 92–95 %,

and that of a solid fuel power plant is 85–88%, it can be concluded that fuel, including renewable fuelwood, is still used inefficiently in Latvia. There are no statistics available on the efficiency of fuel use in households as well as commercial and public sectors, but it is unlikely that it would be higher than the aforementioned indicators. Considering that many households still use stove heating or wood-burning boilers, the efficiency is estimated to be lower than in district heating plants.

5. Limitations on the development of cogeneration. Cogeneration is efficient in terms of primary energy use. However, in Latvia, its development is hindered by the seasonality of efficient use of the generated heat, as well as the lack of a substantial industrial heat load.
6. Many homeowners are unwilling or do not have the means to restore hazardous and unsafe buildings. Some apartment buildings are in poor technical condition.

Opportunities:

1. Increasing the share of RES in the total energy consumption. Latvia aims to increase the share of renewable energy in the total gross final energy consumption to at least 40 % and to continue gradually increasing it in the future.
2. Using RES more efficiently. By introducing modern technologies that are compatible with RES, especially in the production of heat energy, it is possible to achieve a more efficient use of these resources.
3. Developing and producing technologies in Latvia. Currently, a relatively small number of power generation equipment is produced locally. Usually, projects that implement the use of RES, utilize imported equipment; therefore, the government should consider providing support to local equipment manufacturers, as this would promote employment and reduce imports.
4. Having a purposeful state aid. It should be carefully considered which renewables to focus on, as it determines the potential state aid programmes that could be implemented. The requirements of the Law on Residential Properties are partly related to the discrepancies between solar panel owners and energy consumers. Households that obtain electricity from solar panels, can store the excess energy by transferring it to the distribution system operator “Sadales tīkls” according to the net metering principles. In the off-season, for example, during winter, when the efficiency of solar panels is lower, households can use up the previously produced and stored electricity, covering only the costs of the distribution service. However, at this moment this model only applies to individual customers using solar panel solutions. In a multi-apartment building, where each apartment has its own commercial energy metering system, the energy generated from solar panels installed on the shared roof must be used immediately. It is intended for all residents of the building and covers only the electricity consumption in common use areas. For this group of customers, the option of transferring the generated energy to the power network and getting it back later is not available. This creates unequal conditions, which the Saeima intends to address by proposing amendments to the Energy Law and including the notion of energy community in it, similar to that in Estonia.
5. According to the European Commission’s proposal, the main objectives

for years 2030 and 2050 in the building renovation sector are decarbonisation and the integration of renewables. Renovation of buildings should accelerate the integration of renewables, in particular the local ones, and promote a wider use of waste heat. Moreover, it should help integrate energy systems at local and regional levels and thus decarbonise the transportation sector as well as the heating and cooling sector [9].

Threats:

1. Improper use of RES – soil depletion, deforestation. The tendency to use biomass and biogas for energy production brings up the issue of sustainability of raw materials, and the impact that exploiting forests and agricultural land has on the environment and the living conditions.
2. Ill-considered state aid – excessive support/double support. For example, certain initiatives (i.e., using renewable energy sources to generate electricity) can simultaneously receive two types of support – in the form of mandatory procurement of electricity (the costs of which are covered by electricity consumers) as well as in the form of financing from the EU funds and other support instruments. The mandatory electricity procurement allows for escalation of purchase prices since this purchase price is determined by using formulas linked to the price of natural gas or certain coefficients. Thus, the purchase price of electricity exceeds the electricity exchange price several times and is also significantly higher than the final tariff for consumers.
3. Only a small number of merchants benefit, not the whole population. Some support programmes benefit only a small number of merchants, as they receive income from mandatory procurement programmes and/or financial aid, while the support provided to society as a whole is negligible – the amount of electricity produced is small, there is only a small increase in employment or no increase at all, and besides, the equipment and spare parts thereof are imported. There is no clear vision or policy on goals in the housing sector, which is characterised by:
   - deterioration of residential buildings built during the Soviet era;
   - population decline;
   - rising construction, renovation, and real estate development costs as a result of price harmonisation across European markets;
   - tax law changes;
   - poor quality construction, and skilled labour shortage;
   - apartment owners experiencing financial distress, resulting in an increase in debt.

If solar panels are to be installed on an existing building, the technical condition of this building plays a crucial role in the entire process of implementing the RES. Therefore, it is important to carry out an initial building survey and evaluation, to be able to successfully choose and install suitable solar panels. A personalised technical and financial evaluation must be carried out before the installation of solar panels and/or heat pumps. When choosing solar panels, one should consider not only the monthly costs but also the cost of one kilowatt of power compared to other solar panel systems with the same total area.

To evaluate the costs and benefits of this investment, the amount of annual electricity consumption should be determined before solar panel installation. If the average monthly electricity consumption is below 300 kWh, there is a relatively high chance that the solar panels will not pay off or pay off rather slowly. When installing solar panels, it is particularly important to know the annual consumption. During the sunniest months of the year, solar panels should produce enough electricity to cover all electricity needs and compensate for the winter months when the sun shines much less. Solar panels typically pay off in 6–7 years, and last for 25–30 years.

Professional management and supervision from the beginning to the end shall be ensured for such projects.

To promote faster implementation of renewable energy resources in Latvia, on 1 March 2022, the Cabinet of Ministers adopted Regulations No. 150 "Regulations of the Open Tender "Reduction of Greenhouse Gas Emissions in Households – Support for the Use of Renewable Energy Resources" of Projects Financed by the Emission Quota Auction Instrument". The objective is to reduce greenhouse gas emissions and improve energy efficiency in households by supporting the purchase of new heat energy or electricity-generating equipment to produce power for household needs, or the connection of households to the district heating system [13].

4. CONCLUSION

The potential of renewables is not to reduce energy consumption but rather to provide energy with a lower environmental impact. RES has great potential in Latvia, but it has not been fully exploited yet. The factors that have impeded the use of RES are inadequate planning, insufficient knowledge, and restricted access to the latest technologies. In addition, the use of renewable energy resources is hampered by socio-economic factors, such as the proximity to Russia's abundant fossil fuel resources, which a few years ago were available to Latvia at very low prices. It is worth noting that local coastlines are technically suitable for the development of wind energy generation and in Latvian conditions wood chips and shavings are considered to be the cheapest types of fuel.

The government has adopted a state support programme to reduce and compensate the costs of energy for the population of Latvia during the rise in energy prices. The state grants support to those transitioning from existing heating equipment that utilises fossil energy sources (natural gas, coal, diesel) to new heating equipment that utilises renewables (biomass pellet boilers, solar panels, heat pumps) and those purchasing new renewable energy equipment (solar panels, wind generators) to produce electricity (regardless of the currently employed heating system). This decision is also a step towards energy independence. This will increase the power output of renewable energy resources and provide citizens with the support they need to reduce the electricity and heating bills in the long term.

REFERENCES

1. IPCC. (2021). *Climate 2021: The Physical Science Basis Contribution of Working Group 1 to the Sixth Assessment Report of the Intergovernmental Panel on Climate Change*. Cambridge University Press.

2. Yein, M.T, Shestopalova, T.A., Tyagunov, M.G., & Beijing, H.H. (2022). Program for the selection of sites to construct renewable energy plants based on the method of analytic hierarchy process (AHP). In *2021 Innovations in Energy Management and Renewable Resources* (52042). 12–15 April 2022. DOI: 10.1109/Inforino53888.2022.9782923
3. Vides aizsardzības un reģionālās attīstības ministrija. (2019). *Informatīvais ziņojums "Latvijas stratēģija klimatneitralitātes sasniegšanai līdz 2050. gadam".*
4. European Commission. (2018). *Directive (EU) 2018/2001 of the European Parliament and of the Council on the Promotion of the Use of Energy from Renewable Sources*. Official Journal of the European Union, 2018(L 328), pp. 82–209.
5. European Parliament and the European Council. (2018). *Directive (EU) 2018/2001 of the Use of Energy from Renewable Sources*. Available at https://eur-lex.europa.eu/legalcontent/en/TXT/?uri=CELEX%3A32018L2001
6. Sauhats, A., Zemite, L., Petricenko, L., Kozadajevs, J., & Bezrukovs, D. (2018). *Elektroenerģijas NETO sistēmas izvērtējums un priekšlikumi sistēmas uzlabojumiem*. Riga: Riga Technical University.
7. Byrne, P. (2022). Research Summary and Literature Review on Modelling and Simulation of Heat Pumps for Simultaneous Heating and Cooling for Buildings. *Energies, 15*, 3529. https://doi.org/ 10.3390/en15103529
8. Yamazaki, K., Otsubo, M., & Okuma, K. (1986). *Mitsubishi Electric Corp. Room-Warming/Cooling and Hot-Water Supplying Heat-Pump Apparatus.* U.S. Patent 4,592,206
9. Eiropas Komisija. (2020). *Komisijas paziņojums eiropas parlamentam, padomei, eiropas ekonomikas un sociālo lietu komitejai un reģionu komitejai. Eiropas Renovācijas vilnis – par zaļākām* ēkām, *jaunām darbvietām un labāku dzīvi (2020).* Brisele. COM(2020) 662 final. Available at https://eur-lex.europa.eu/legal-content/LV/TXT/?uri=CELEX:52020DC0662
10. Ekonomikas ministrija. (2018). *Latvijas Nacionālais enerģētikas un klimata plāns 2021. – 2030. gadam projekts iesniegšanai eiropas komisijā izvērtējumam*. Latvia_NECP2021-2030_PROJECT_2018.docx. Available at https://energy.ec.europa.eu/system/files/2019-02/latvia_draftnecp_0.pdf
11. Ekonomikas ministrija. (2019). *Latvijas Nacionālais enerģētikas un klimata plāns 2030. gadam*. EMp1_131219_NEKP2030.docx. Available at https: //www.em.gov.lv/sites/em/files/2019-12-20_14_56_12empl1_131219_nekp20301_0.docx
12. Latvijas Republikas Ministru kabinets (2022). *Ministru kabineta noteikumi Nr.150 "Emisijas kvotu izsolīšanas instrumenta finansēto projektu atklāta konkursa "Siltumnīcefekta gāzu emisiju samazināšana mājsaimniecībās – atbalsts atjaunojamo energoresursu izmantošanai" nolikums"*. Available at https://likumi.lv/ta/id/330568-emisijas-kvotu-izsolisanas-instrumenta-finanseto-projektu-atklata-konkursa-siltumnicefekta-gazu-emisiju-samazinasana-majsaimniecibas
13. Latvijas Valsts agrārās ekonomikas institūts. *SVID analīze par situāciju valstī saistībā ar atjaunojamajiem energoresursiem.* – Rīga: 2012.-42. p. Pieejams: https://www.arei.lv/lv/2012-gads

LATVIAN JOURNAL OF PHYSICS
AND TECHNICAL SCIENCES
2024, N 3

DOI: 10.2478/lpts-2024-0023

NEUTRONIC INVESTIGATION ON THORIUM MOX FUEL IN VVER-1000 REACTOR ASSEMBLY

Zuhair*, W. Luthfi, R.A.P. Dwijayanto, M.D. Isnaini, Suwoto

Research Center for Nuclear Reactor Technology (PRTRN)
Research Organization for Nuclear Energy (ORTN),
National Research and Innovation Agency (BRIN)
Kawasan Sains dan Teknologi BJ Habibie, OB No. 80, Serpong,
Tangerang Selatan 15310, INDONESIA
*e-mail: zuhair@brin.go.id

The accumulation of plutonium produced by LWR operations causes public concern related to its radiotoxicity and proliferation issue. Therefore, there is some interest in developing various methods for consuming plutonium through plutonium incineration i.e., by utilising thorium-based nuclear fuel. Thorium-plutonium mixed oxide fuel (Thorium MOX) is an attractive option considered for plutonium incineration. The aim of the study is to investigate the neutronic characteristics of Thorium MOX fuel in VVER-1000 nuclear reactor fuel assemblies. The VVER-1000 Benchmark model was utilised in the present study. A series of calculations were performed with the MCNP6 code and the ENDF/B-VII library. The calculation results show that a proper increase in Pu content could increase k_{inf} of ThMOX fuel, so it could have almost the same k_{inf} with MOX fuel or increase Pu content when needed. It was also shown that Thorium MOX fuel assembly had more negative Doppler reactivity due to neutron capture by thorium (^{232}Th). The moderator temperature coefficient was found to be more negative than the Doppler coefficient, and it could be concluded that replacing uranium with thorium could reduce the amount of plutonium produced while increasing plutonium consumption.

Keywords: *ENDF/B-VII, MCNP6, thorium MOX, VVER-1000 reactor assembly.*

1. INTRODUCTION

A continuous and rapid global population increase and economic growth in many countries cause the world's energy demand to increase. Nowadays, around 81 % of the world's energy demand is supplied by fossil fuels, but it increases CO_2 emissions causing global warming and climate change, endangering the environment and society in the future. Utilising nuclear energy which generates low-CO_2 electricity is a realistic choice to mitigate the effects of global warming and climate change answering the increase in energy demand [1], [2]. Currently, there are 443 operating nuclear power plants (NPPs) in more than 30 countries around the globe. All these NPPs, which are dominated by light water reactors (LWR), take up to 10 % of the world's electric energy demand.

In addition to generating a large amount of electricity, NPPs are also producing nuclear waste which is classified as high-level waste (HLW), intermediate-level waste (ILW), and low-level waste (LLW). HLW consists of fission products and transuranic elements generated within fuel elements during reactor operation, while LLW represents waste produced during reactor operation such as neutron-activated structural materials, tools or equipment, radiation protection clothing, and residues from industries.

As previously mentioned, HLW consists of transuranic (TRU) and fission products. TRU is a product of transmutation mostly found in the uranium fuel cycle, which came from fertile isotope ^{238}U, and it captures neutrons and transmutes into heavier isotopes. It provides a significant contribution to the radiotoxicity of nuclear waste, which came from isotopes of plutonium (Pu) and minor actinide (MA) isotopes, such as Neptunium (Np), Americium (Am), and Curium (Cm) [3].

The accumulation of plutonium produced by LWR operations causes public concern related to its radiotoxicity and proliferation issue [4]. Therefore, there is some interest in developing various methods for consuming plutonium through plutonium incineration, i.e., by utilising thorium-based nuclear fuel. Thorium-plutonium mixed oxide fuel (Thorium MOX) is an attractive option that has been considered for plutonium incineration, which significantly produces less plutonium during incinerating plutonium [5]. Several studies successfully demonstrated the superior capabilities of Thorium MOX fuel for plutonium incineration using deterministic code [6]–[10]. However, the neutronic characteristics of the reactor core using Thorium MOX fuel should be examined because plutonium could give a considerable impact on the operational and safety parameters of the reactor [11].

The aim of the study is to investigate the neutronic characteristics of Thorium MOX fuel in VVER-1000 nuclear reactor fuel assemblies. The VVER-1000 Benchmark model [12] was utilised in the present investigation to examine the effect of replacing MOX fuel with Thorium MOX fuel on the same fuel assembly configuration. A series of calculations were performed with the Monte Carlo transport code MCNP6 [13] and the continuous nuclear data library ENDF/B-VII [14]. The analysis was focused on the neutronic performance between MOX and Thorium MOX fuel assemblies such as excess reactivity, fuel temperature coefficients of reactivity (DTC), moderator temperature coefficients of reactivity (MTC), and plutonium incineration.

2. VVER-1000 ASSEMBLY

VVER-1000 (Vodo-Vodyanoi Energetichesky Reactor or Water-Water Energetic Reactor) is a type of pressurized water reactor with 3000 MW thermal power that could convert into 1000 MW electric power. The benchmark model for VVER-1000 consists of two typical hexagonal fuel assemblies from advanced Russian fuel designs, a LEU fuel assembly and MOX fuel assembly. These two assemblies are calculated as verification to VVER-1000 fuel calculation code, and supporting the mission to reduce weapon-grade plutonium proliferation [12].

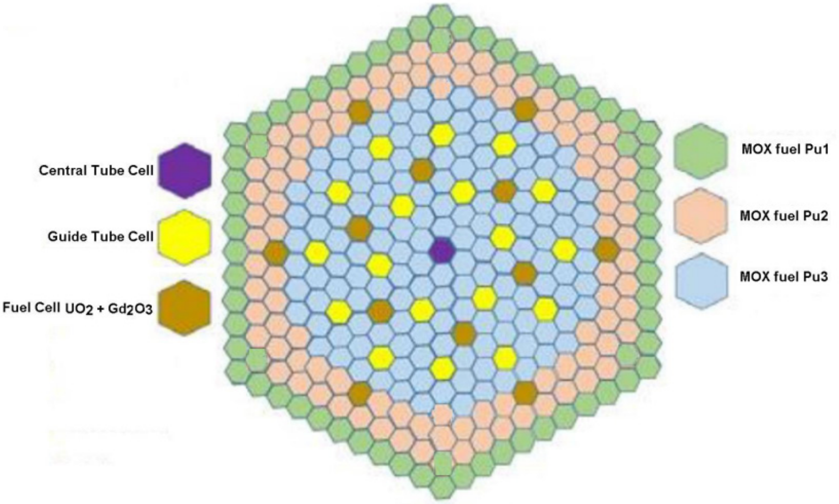

Fig. 1. VVER-1000 MOX fuel assembly.

The MOX fuel assembly consists of 300 MOX fuel rods, 12 GD1 fuel rods, 18 guide tubes, and one central tube. The fuel rods and guide tubes are arranged in a twelfth symmetry, and there are three different plutonium contents in MOX fuel assembly. The outermost ring of MOX assembly is loaded with 66 fuel rods with 2.0 wt% fissile plutonium (PU1), while the second and third inner rings are filled with 96 fuel rods with 3.0 wt% fissile plutonium (PU2). The central region (138 fuel rods) has the highest plutonium content of 4.2 wt% (PU3). The Gd_2O_3 content is used in the fuel assembly to suppress excess reactivity at the beginning of cycle, i.e., GD1 in this model is a UO_2 fuel with 3.6 wt% ^{235}U enrichment mixed with 4 wt% Gd_2O_3 [15]. The configuration of the VVER-1000 MOX fuel assembly is shown in Fig. 1, and reactor design parameters are given in Table 1.

In this study, the thorium MOX fuel was loaded into the fuel assembly by replacing the regular MOX fuel without significant assembly modifications, called Thorium MOX fuel. The Thorium MOX fuel being analysed in this paper consists of two types: ThMOX1 with plutonium content adjusted from 2 wt% to 3 wt%, 3 wt% to 4.5 wt%, and 4.2 wt% to 6.3 wt%, or increased 1.5 times, and ThMOX2 with plutonium content adjusted from 2 wt% to 6 wt%, 3 wt% to 9 wt%, and 4.2 wt% to 12.6 wt% or increased three times. The three plutonium compositions being used remain unchanged and are given in Table 2. The plutonium content is increased to anticipate the reduction in nuclear fission reactions due to the replacement of uranium to thorium.

Table 1. Design Parameters of the VVER-1000 MOX Fuel Assembly

Number of MOX fuel cell (PU1)	66
Number of MOX fuel cell (PU2)	96
Number of MOX fuel cell (PU3)	138
Number of UO_2+Gd_2O_3 fuel cell (GD1)	12
Number of guide tubes	18
Number of central tube	1
Inner/outer radius of fuel cell (cm)	0.3860/0.4582
Inner /outer radius of central tube cell (cm)	0.4800/0.5626
Inner/outer radius of guide tube cell (cm)	0.5450/0.6323
Pitch of fuel cell (cm)	1.2750
Pitch of fuel assembly (cm)	23.6
Temperature of fuel (K)	1027
Temperature of non-fuel (K)	575
Enrichment of ^{235}U (wt%)	3.6
Density of Gd_2O_3 (g/cm^3)	7.4

Table 2. Plutonium Isotopic Composition

Isotope	PU1	PU2	PU3
^{239}Pu	0.9290	0.9310	0.9300
^{240}Pu	0.0610	0.0590	0.0599
^{241}Pu	0.0100	0.0100	0.0101

3. CALCULATION MODEL

In this study, a series of calculations using MCNP6 code and ENDF/B-VII nuclear data have been performed to investigate the neutronic aspect of Thorium MOX fuel of the VVER-1000 fuel assembly. MCNP6 is a general-purpose, continuous-energy Monte Carlo radiation transport code developed by Los Alamos National Laboratory (LANL) to track neutron, photon, electron, or combined radiation particles over broad ranges of energies. MCNP6 is the latest Monte Carlo transport code created by merging and integrating all features of MCNP5 [16] and MCNPX [17]. Code capabilities have been demonstrated in simulating fuel assembly and complex core configurations on various reactor types [18]–[29].

Modelling the VVER-1000 MOX fuel assembly began with modelling the fuel, central tube, and guide tube cells. The fuel rod was modelled with a radius of 0.3860 cm surrounded by water that made up a hexagonal lattice. The zircaloy-4 cladding in the fuel rod was modelled encasing the fuel with a thickness of 0.0722 cm. Zr-Nb-Hf alloys are utilised as a structural material. The MOX fuel has three different plutonium contents: 2.0 wt% fissile plutonium (PU1), 3.0 wt% fissile plutonium (PU2), and 4.2 wt% (PU3). The GD1 fuel cell was modelled with a similar technique as the MOX fuel cell.

Although they have different functions, the modelling of the central tube and guide tube is quite similar, the water fill in both tubes was placed with a radius of 0.4800 cm and 0.5450 cm, respectively. The claddings with thicknesses of 0.0826 cm for the central tube and 0.0873 cm for the guide tubes are also placed, followed by surrounding water outside these claddings marking up a fuel rod lattice with a hexagonal pitch of 1.2750 cm. The exact geometry modelled by MCNP6 for fuel, central tube and guide tube cells is depicted in Fig. 2.

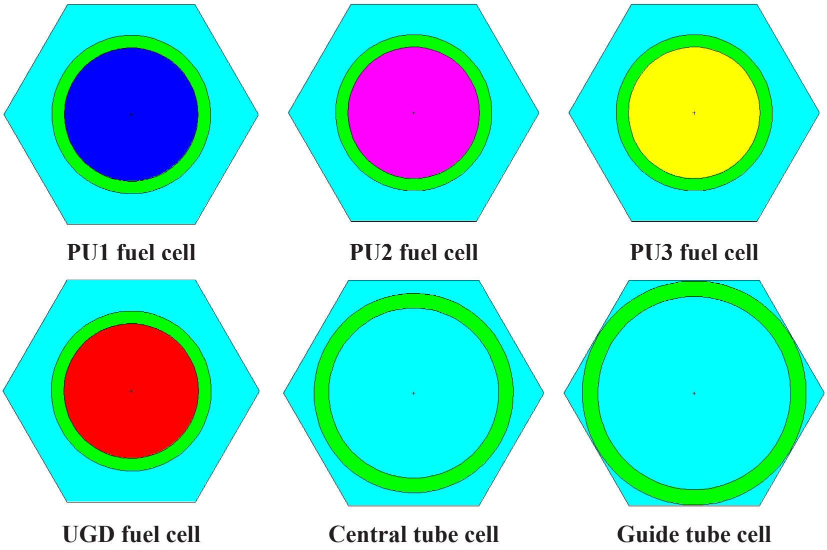

Fig. 2. MCNP6 model for fuel, central tube, and guide tube cells.

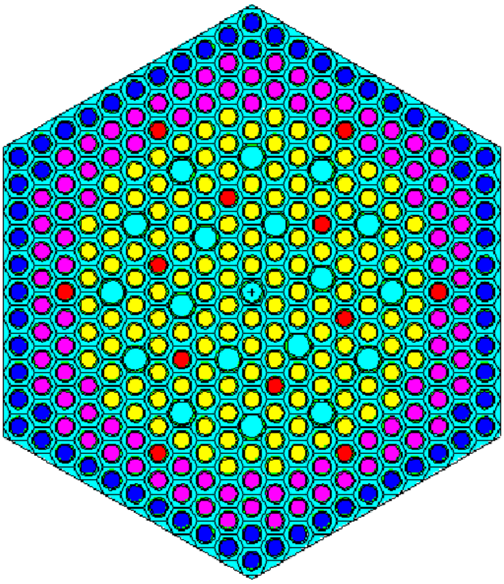

Fig. 3. MCNP6 model for VVER-1000 MOX assembly.

The VVER-1000 MOX fuel assembly model was constructed by making an array of fuel, guide tubes, and central tube cells in a hexagonal geometry. The water surrounding the whole fuel array is then making up the fuel assembly that has a pitch of 23.6 cm. All outer surfaces of the VVER-1000 MOX fuel assembly were assumed to be reflective surfaces. The exact geometry modelled by MCNP6 model for fuel assembly is depicted in Fig. 3. Detailed isotopic compositions of MOX fuel assemblies is given in Table 3.

Table 3. Isotopic Compositions of VVER-1000 MOX Assembly

PU1	MOX fuel with 2.0 wt% Pu fissile	^{235}U	4.2672E-5	^{239}Pu	4.2414E-4
		^{238}U	2.1025E-2	^{240}Pu	2.7250E-5
		^{16}O	4.3047E-2	^{241}Pu	4.5228E-6
PU2	MOX fuel with 3.0 wt% Pu fissile	^{235}U	4.2209E-5	^{239}Pu	6.3621E-4
		^{238}U	2.0797E-2	^{240}Pu	4.0875E-5
		^{16}O	4.3045E-2	^{241}Pu	6.7842E-6
PU3	MOX fuel with 4.2 wt% Pu fissile	^{235}U	4.1652E-5	^{239}Pu	8.9071E-4
		^{238}U	2.0522E-2	^{240}Pu	5.7225E-5
		^{16}O	4.3043E-2	^{241}Pu	9.4980E-6
UGD	UO$_2$ fuel with 3.6 wt% ^{235}U and 4 wt% Gd$_2$O$_3$	^{235}U	7.2875E-4	^{155}Gd	1.8541E-4
		^{238}U	1.9268E-2	^{156}Gd	2.5602E-4
		^{16}O	4.1854E-2	^{157}Gd	1.9480E-4
		^{152}Gd	2.5159E-6	^{158}Gd	3.0715E-4
		^{154}Gd	2.7303E-5	^{160}Gd	2.6706E-4

Table 4. Isotopic Compositions of VVER-1000 Thorium MOX Assembly

PT1	Thorium MOX fuel with 3 wt% Pu fissile	^{230}Th	4.3000E-6	^{239}Pu	6.3426E-4
		^{232}Th	2.1310E-2	^{240}Pu	4.1647E-5
		^{16}O	4.3994E-2	^{241}Pu	6.8274E-6
PT2	Thorium MOX fuel with 4.5 wt% Pu fissile	^{230}Th	4.2292E-6	^{239}Pu	9.5145E-4
		^{232}Th	2.0959E-2	^{240}Pu	6.2474E-5
		^{16}O	4.3975E-2	^{241}Pu	1.0242E-5
PT3	Thorium MOX fuel with 6.3 wt% Pu fissile	^{230}Th	4.1443E-6	^{239}Pu	1.3321E-3
		^{232}Th	2.0539E-2	^{240}Pu	8.7470E-5
		^{16}O	4.3953E-2	^{241}Pu	1.4339E-5
PT4	Thorium MOX fuel with 6 wt% Pu fissile	^{230}Th	4.1585E-6	^{239}Pu	1.2687E-3
		^{232}Th	2.0609E-2	^{240}Pu	8.3304E-5
		^{16}O	4.3957E-2	^{241}Pu	1.3656E-5
PT5	Thorium MOX fuel with 9 wt% Pu fissile	^{230}Th	4.0170E-6	^{239}Pu	1.9032E-3
		^{232}Th	1.9907E-2	^{240}Pu	1.2497E-4
		^{16}O	4.3920E-2	^{241}Pu	2.0487E-5
PT6	Thorium MOX fuel with 12.6 wt% Pu fissile	^{230}Th	3.8471E-6	^{239}Pu	2.6649E-3
		^{232}Th	1.9066E-2	^{240}Pu	1.7498E-4
		^{16}O	4.3876E-2	^{241}Pu	2.8686E-5

Table 5. Isotopic Compositions of Non-fuel Material in VVER-1000 Assembly

CL1	Zirconium alloy	^{93}Nb	4.2250E-4	^{174}Hf	1.0555E-8
		^{90}Zr	2.1913E-2	^{176}Hf	3.4700E-7
		^{91}Zr	4.7786E-3	^{177}Hf	1.2270E-6
		^{92}Zr	7.3042E-3	^{178}Hf	1.7997E-6
		^{94}Zr	7.4021E-3	^{179}Hf	8.9851E-7
		^{96}Zr	1.1925E-3	^{180}Hf	2.3142E-6
MOD1	Moderator, 0.6 g/kg of boron, T_m= 575K, ρ= 0.7235 g/cm^3	^{1}H	4.8430E-2	^{10}B	4.7940E-6
		^{16}O	2.4220E-2	^{11}B	1.9420E-5
MOD2	Moderator, without boron, T_m= 575K, ρ= 0.7235 g/cm^3	^{1}H	4.8430E-2	^{10}B	0
		^{16}O	2.4220E-2	^{11}B	0
MOD3	Moderator, without boron, T_m= 300K, ρ= 1.0033 g/cm^3	^{1}H	6.7170E-2	^{10}B	0
		^{16}O	3.3580E-2	^{11}B	0

This study investigates the neutronic performance of Thorium MOX fuel in the fuel assembly of the VVER-1000 reactor. Modelling the modified fuel assembly by Thorium MOX fuel was done in the same way as those of MOX assembly since it used an identical dimension and geometry. Thorium MOX fuel being modelled was modified as mentioned in the previous section: ThMOX1 with 3 wt% fissile plutonium (PT1), 4.5 wt% fissile plutonium (PT2), and 6.3 wt% (PT3), and ThMOX2 with 6 wt% fissile plutonium (PT4), 9 wt% fissile plutonium (PT5), and 12.6 wt% (PT6). Detailed isotopic compositions of Thorium MOX fuel assemblies are provided in Table 4, and the isotopic compositions of non-fuel materials in fuel assemblies are given in Table 5. This paper considers three different coolant states shown as MOD1, MOD2, and MOD3 representing different densities, temperatures, and boron concentrations in g Boron/kg water, used in the calculation. MOD1 stands for 575 K water with density of 0.7235 g/cm^3 and 600 ppm boron, MOD2 stands for 575 K water without soluble boron, and MOD3 stands for 300 K water with density of 1.0033 g/cm^3 also without soluble boron.

4. RESULTS AND DISCUSSION

The KCODE card was used in MCNP6 with 100,000 neutrons per cycle, 500 total cycles and the first 100 cycles skipped. The initial fission source defined by the KSRC card was positioned in the middle of a fuel assembly. The thermal scattering data S(α,β) for light water were used to consider thermal neutron interaction with water at the energy region below ~4 eV. Reflective boundary conditions were used on the outer surface of the fuel assembly to make sure that the neutrons were reflected back to the fuel assembly when reaching boundaries.

4.1. Model Validation

The benchmark problems are made up of five conditions or states, covering both cold and hot operation conditions of the VVER-1000 reactor as shown in Table 6. S1 is the operation condition while soluble boron exists within the coolant at 600 ppm, and the burnup calculation was carried out in this condition. S2 was the same as S1 but it was calculated without ^{135}Xe and ^{149}Sm poisoning. S3 was a hot zero power condition with 575 K fuel and coolant temperature and 600 ppm boron concentration, while S4 was the same as S3 but without soluble boron. S5 was set to a cold zero power condition without soluble boron with fuel and coolant temperature of 300 K. These five reactor conditions were then used to estimate the reactivity coefficients of the VVER-1000 fuel assembly.

Table 6. Calculated Reactor Conditions

State	Description	Fuel temp. (K)	Non-fuel temp. (K)	^{135}Xe, ^{149}Sm	Moderator type	Boron (ppm)	Moderator density (g/cm^3)
S1	Operating poisoned state	1027	575	Equil.	MOD1	600	0.7235
S2	Operating non-poisoned state	1027	575	0	MOD1	600	0.7235
S3	Hot state	575	575	0	MOD1	600	0.7235
S4	Hot state without boron acid	575	575	0	MOD2	0	0.7235
S5	Cold state	300	300	0	MOD3	0	1.0033

Table 7. The k_{inf} of VVER-1000 MOX Assembly

State	MCNP6 (M)	SERPENT (S)	Δk (%) [(M-S)/S]
S2	1.20072 ±9E-05	1.19258 ±8.6E-05	0.683
S3	1.21201 ±9E-05	1.20919 ±8.4E-05	0.233
S4	1.24673 ±1E-04	1.24408 ±8.5E-05	0.213
S5	1.33015 ±9E-05	1.32487 ±7.6E-05	0.398

The k_{inf} results from MCNP6 calculations for VVER-1000 MOX assembly in the states S2-S5 in comparison with Serpent calculation from reference [30] are given in Table 7. All these calculations were conducted without burnup. It can be observed that k_{inf} values are in good agreement with SERPENT results. The small difference in k_{inf} of MCNP6 and SERPENT could be neglected and it could be stated that the model used in this calculation was quite consistent to the ones being used in SERPENT.

4.2. Thorium MOX Fuel

The k_{inf} result from the burnup calculation of VVER-1000 fuel assemblies using MOX and Thorium-MOX fuels is illustrated in Fig. 3. The burnup calculation was performed using the CINDER depletion module with the equilibrium ^{135}Xe and ^{149}Sm state was used at a thermal power density of 108 MW/m^3, with 1027 K fuel temperatures and 575 K on non-fuel as mentioned before (S1). The 20 burnup steps consist of 15 steps with intervals of 1 MWd/kgHM for 0-15 MWd/kgHM and 5 steps with intervals of 5 MWd/kgHM for 15–40 MWd/kgHM.

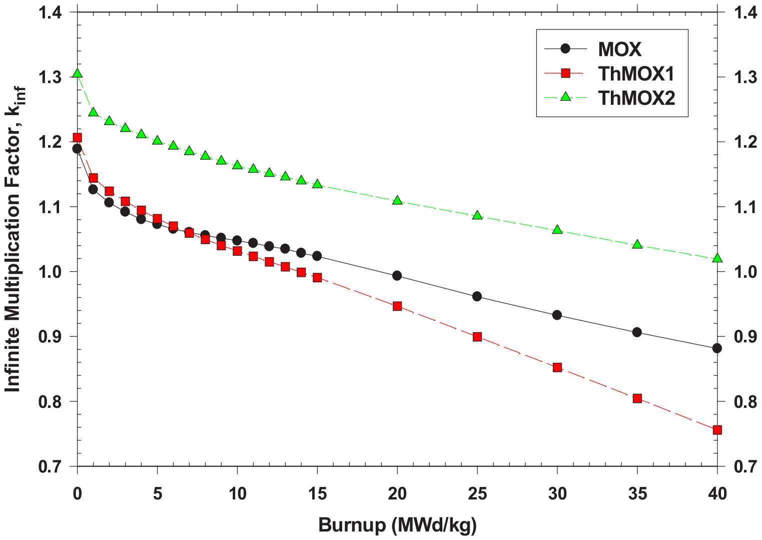

Fig. 3. K_{inf} as a function of burnup.

Figure 3 shows that at the beginning of cycle, the k_{inf} values are 1.18896 for MOX, 1.20649 for ThMOX1, and 1.30397 for ThMOX2 fuel assemblies, with a standard deviation below 10^{-4}. The MOX fuel shows a slightly sharper reduction in reactivity than the ThMOX fuel. At the beginning of cycle (BOC), ThMOX1 has almost the same k_{inf} as MOX fuel and ThMOX2 has higher k_{inf} since it uses a higher percentage of fissile plutonium as shown in Table 4. The MOX fuel assembly k_{inf} drops below unity when it reaches 20 MWd/kg, while the ThMOX1 fuel assembly can only keep criticality up to 14 MWd/kg. ThMOX2 demonstrates its ability to maintain criticality for up to 40 MWd/kg. This means that the ThMOX2 fuel could provide higher discharge reactivity than MOX fuel with its higher fissile plutonium content. It could improve the overall core cycle length but further consideration might be needed in terms of the production cost of plutonium fuel with higher fissile content and mixed with thorium.

Doppler and moderator temperature coefficients of reactivity are the two most dominant temperature coefficients in nuclear reactor systems. In reactor physics, the Doppler effect is due to Doppler broadening on resonance spectrum of nuclear reaction cross section of heavy metal isotopes, Th, U, Pu, etc. The Doppler temperature coefficient of reactivity (DTC) is then defined as the ratio of reactivity changes caused by fuel temperature increase. The moderator temperature coefficient of reactivity (MTC) is then defined as the change in reactivity caused by a change in moderator temperature. As the moderator increases in temperature, it becomes less dense and caused lower neutron moderation, leading to a hardened neutron spectrum which will decrease the core reactivity or lower reactivity. DTC is considered to have a greater effect than MTC because fuel temperature changes immediately followed by a change in reactor power.

The calculated temperature coefficient of reactivity for MOX and Thorium MOX fuel is listed in Table 8, and all MTC and DTC values are negative and take part as an inherent safety feature in the reactor physic aspect. The temperature coefficient of reactivity was computed at 0 MWd/kgHM, 20

MWd/kgHM, and 40 MWd/kgHM using the isotopic compositions from the burnup calculations on state S1. The Doppler coefficient of reactivity was simulated from the differences in k_{inf} for the state S2 and S3, where fuel temperature changed from 575 K to 1027 K and the non-fuel was constant at 575 K. The moderator temperature coefficient was estimated as differences in k_{inf} between the state S4 and S5 by switching the temperature of fuel and moderator from 575 K to 300 K.

Table 8. The Doppler Coefficient of Reactivity (DTC, $\Delta k/k\ K^{-1}$)

Burnup (MWd/kgHM)	MOX	ThMOX1	ThMOX2
0	-7.75793E-03	-1.01569E-02	-9.06375E-03
20	-8.82312E-03	-1.24533E-02	-9.80345E-03
40	-1.03861E-02	-1.65213E-02	-1.12742E-02

Table 9. The Moderator Coefficient of Reactivity (MTC, $\Delta k/k\ K^{-1}$)

Burnup (MWd/kgHM)	MOX	ThMOX1	ThMOX2
0	-5.03034E-02	-3.68157E-02	-3.98879E-02
20	-4.39760E-02	-4.00401E-02	-3.78422E-02
40	-4.12520E-02	-2.90968E-02	-4.55328E-02

From Table 8, it is evident that the Doppler reactivity value of the Thorium MOX assembly increases negatively with the burnup; contrary, the negative value of the moderator temperature coefficient decreases with the burnup. Compared to MOX fuel, Thorium MOX assembly has more negative Doppler reactivity due to thorium, in this case, ^{232}Th, absorbs larger neutrons than ^{238}U in higher fuel temperatures. The value of the moderator coefficient, as shown in Table 9, is found to be more negative than the Doppler coefficient because the fuel temperature was not kept at a constant as defined in conditions S4 and S5. However, these negative Doppler and moderator temperature coefficients are desirable from a safety point of view, as they help stabilize reactor power and avoid reactor excursions.

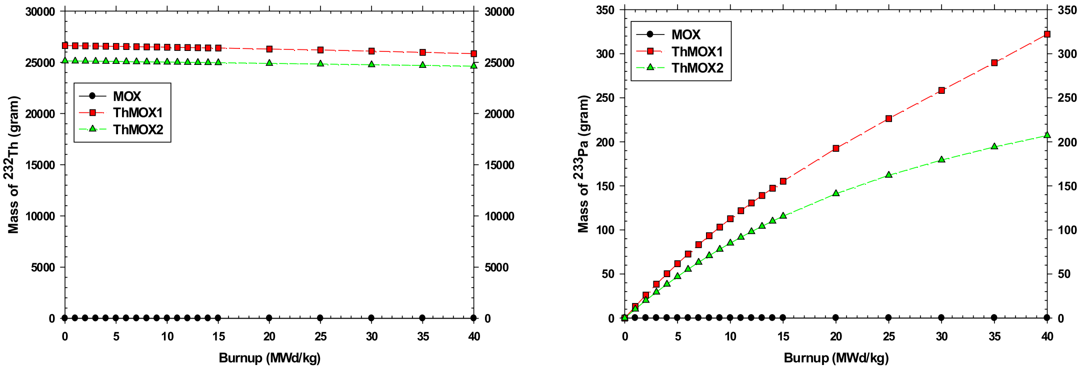

Fig. 4. Mass of ^{232}Th and ^{233}Pa as a function of burnup.

The fuel consumption and the production of some important isotopes in MOX and Thorium MOX fuel assembly are shown in Figs. 4–6. The curve in Figure 4 shows the mass of ^{232}Th being consumed and ^{233}Pa being produced. After 40 MWd/kg burnup, almost 790 g and 510 g of ^{232}Th isotope are being consumed from the 26,630 g and 25,130 g loaded in the first place of ThMOX1 and ThMOX2. There were 322.2 g and 207.1 g of ^{233}Pa being produced. They are lower than thorium being consumed since ^{233}Pa will decay into ^{233}U or transmute into other isotopes i.e., ^{234}Pa. It is straightforward that MOX fuel did not have thorium. Therefore, ^{232}Th and ^{233}Pa will be a flat line on zero. Also, ^{232}Th isotope production in MOX fuel assembly is very small and virtually non-existent since it will be produced by (n,2n) reaction and other neutron emission reactions without fission that have a small possibility to occur.

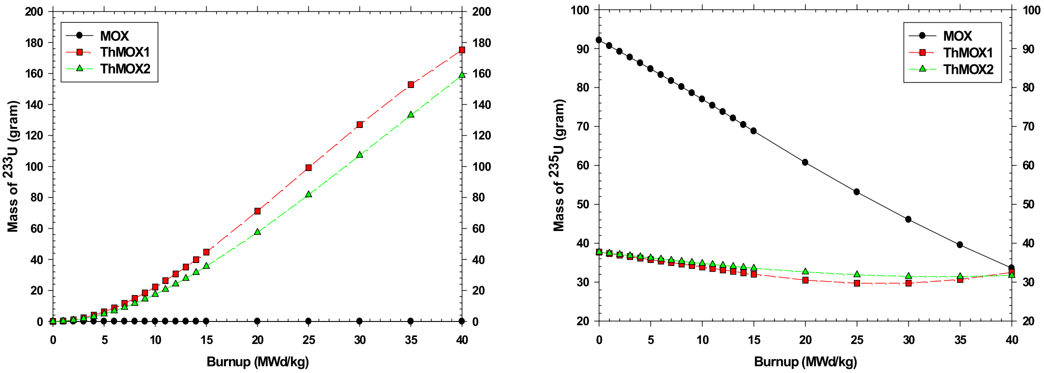

Fig. 5. Mass of ^{233}U and ^{235}U as a function of burnup.

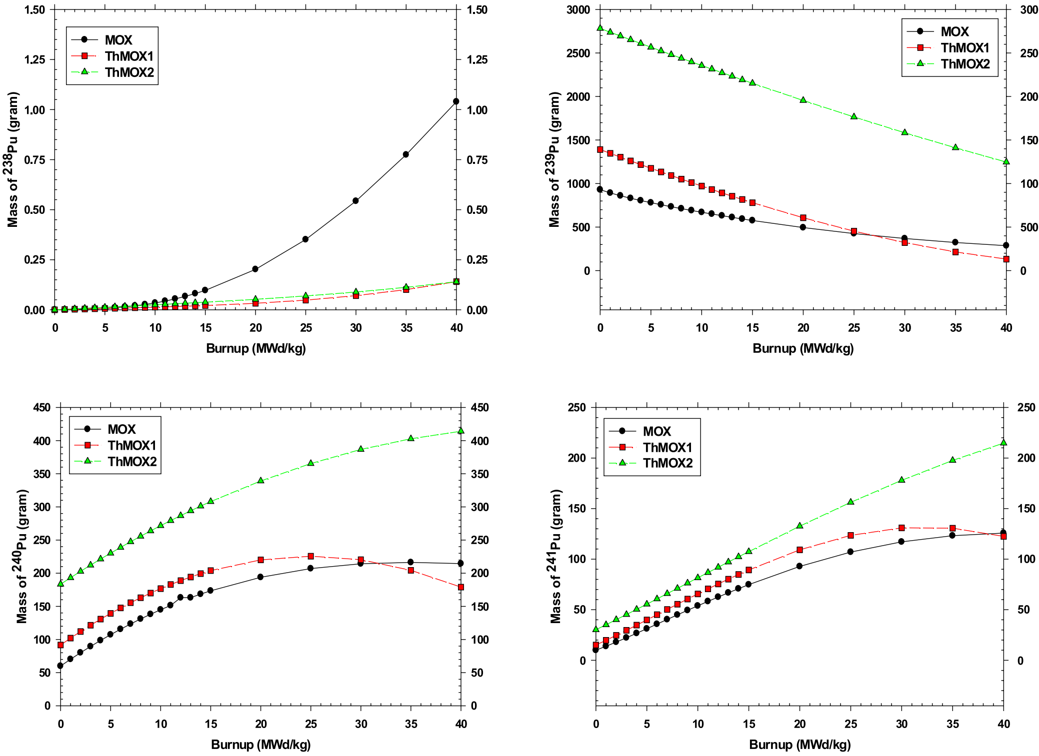

Fig. 6. Mass of ^{238}Pu, ^{239}Pu, ^{240}Pu, and ^{241}Pu as a function of burnup.

Figure 5 shows the ^{233}U and ^{235}U mass change in both fuel elements. ^{233}U in Thorium MOX grows up to 175.2 g and 158.8 g after 40 MWd/kg burnup and is almost unnoticeable on MOX fuel even though ^{233}Pa is being produced in small quantities (1.034E-7 g). Using Thorium as a fuel option could increase the number of fissile isotopes within the fuel assembly since ^{233}U is fissile but with some drawbacks on the economy of neutrons within the fuel assembly since thorium will capture neutrons. As it is shown in Fig. 5, one can observe that the mass reduction of ^{235}U in MOX fuel is sharp from 92.14 g to 33.59 g or 63.54 % since ^{235}U is being consumed. On the another hand, Thorium MOX fuel is only 13.84 % and 15.91 % since they only have a small quantity in the first place, which came from 12 burnable fuel pins (GD1). There is also some tendency for ^{235}U in Thorium MOX fuel to increase after 40 MWd/kg burnup since enough lighter heavy metals, i.e., Pa and U are produced, and they could capture more neutrons and become ^{235}U. However, it is also noticeable that an increase of ^{233}U in Thorium MOX fuel for almost the same amount as the decrease of ^{235}U in MOX fuel does not increase fuel reactivity (k-inf) since plutonium fissile isotopes are dominating the source of fuel reactivity.

Figure 6 shows the changes in some plutonium isotopes, ^{238}Pu, ^{239}Pu, ^{240}Pu, and ^{241}Pu. ^{238}Pu mass is less produced both in ThMOX1 (0.1404 g) and ThMOX2 fuel (0.1403 g) in comparison with MOX fuel (1.039 g) since Thorium MOX fuel has a lower amount of uranium isotopes. In general, ^{238}Pu came from ^{238}Np that undergoes beta decay, or from ^{238}Am emits a positron. On the other hand, the fissile isotope ^{239}Pu is produced from ^{238}Pu that captures a neutron becoming ^{239}Pu, or from ^{238}U that captures a neutron and is followed by beta decay twice. ^{239}Pu is the second most used nuclear fuel in nuclear reactors after ^{235}U since it is dominantly produced by ^{238}U, which is abundant inside the reactor core. From Fig. 6, it can be seen that ^{239}Pu is higher in Thorium MOX fuel in comparison with MOX fuel because plutonium enrichment inside both ThMOX1 and ThMOX2 fuel was higher (1.5 and 3 times) than one being used inside MOX fuel. Even though Thorium MOX reduces more ^{239}Pu, it has higher initial mass so its reduction fraction is similar.

The same as other isotopes, ^{239}Pu could capture neutrons and become a heavier isotope, becoming ^{240}Pu, capturing more neutrons, becoming ^{241}Pu, and so on. Another isotope of plutonium that has an odd mass is fissile, i.e., ^{241}Pu and isotopes with even mass are fertile and have a low capture reaction cross section. Therefore, they tend to accumulate inside nuclear reactors, especially ones dominated by thermal neutrons, as mostly designed in today's nuclear power plants. Like ^{239}Pu at the beginning of cycle, ^{240}Pu mass in ThMOX1 (91.71 g) and ThMOX2 fuel (183.4 g) is almost 1½ and 3 times greater than that in MOX fuel (60.0 g). Figure 6 shows that ^{241}Pu mass in ThMOX1 and ThMOX2 fuel increased by up to 8 and 7, less than MOX fuel reached 12 times. Table 10 summarises the change of plutonium from the beginning until its k_{inf} reaches 1, and it can be seen that adding thorium can increase plutonium being consumed (fraction) within the fuel assembly with some drawback on k_{inf} which leads to smaller core operating time if its Pu content only increases to 1.5 times as ThMOX1 or the VVER core can be made up of various fuel assemblies that use a lot higher Pu content, i.e., 3 times as ThMOX2.

Table 10. Plutonium Mass (g) at BOC and Critical Condition

Isotope	BOC (0 MWd/kg)			Critical condition ($k_{\text{inf}} = 1$)		
	MOX	ThMOX1	ThMOX2	MOX (20 MWd/kg)	ThMOX1 (14 MWd/kg)	ThMOX2 (>40 MWd/kg)
^{238}Pu	0.000E+00	0.000E+00	0.000E+00	2.019E-01	1.943E-02	1.403E-01
^{239}Pu	9.300E+02	1.391E+03	2.782E+03	4.945E+02	8.169E+02	1.247E+03
^{240}Pu	6.000E+01	9.171E+01	1.834E+02	1.938E+02	1.993E+02	4.141E+02
^{241}Pu	1.000E+01	1.510E+01	3.020E+01	9.282E+01	8.484E+01	2.147E+02
^{242}Pu	0.000E+00	0.000E+00	0.000E+00	1.406E+01	7.026E+00	2.669E+01
Total	1.000E+03	1.498E+03	2.996E+03	7.954E+02	1.108E+03	1.903E+03
Reduced total Pu (g) [mass at critical – mass at BOC]				-2.046E+02	-3.900E+02	-1.093E+03
Consumption rate [(Reduced total Pu/ mass at BOC) × 100 %]				-25.72 %	-35.20 %	-57.44 %

5. CONCLUSION

The neutronic investigation on Thorium MOX fuel in the VVER-1000 reactor assembly was conducted. A series of calculations were done with the MCNP6 code and the ENDF/B-VII library. The calculation results show that ThMOX1 has almost the same k_{inf} as MOX fuel and ThMOX2 has higher k_{inf} since it uses a higher percentage of fissile plutonium. Compared to MOX fuel, Thorium MOX assembly has more negative Doppler reactivity due to thorium. In this case, ^{232}Th, absorbs larger neutrons than ^{238}U in higher fuel temperatures. The value of the moderator coefficient was found to be more negative than the Doppler coefficient in this configuration. It can be concluded that replacing uranium with thorium can reduce the amount of plutonium produced while increasing plutonium consumption.

ACKNOWLEDGEMENT

The authors gratefully acknowledge Dr. Eng. Topan Setiadipura, S.Si, M.Si. and Dr. Anis Rohanda, S.T., M.Si. for their inspiration and motivation. The authors also gratefully acknowledge Prof. Dr. Eng. Zaki Su'ud from the Nuclear Physics and Biophysics Research Division, Physics Department, Institut Teknologi Bandung (ITB) for granting us permission to use the MCNP6 code license in our simulations.

REFERENCES

1. Lentzos, I. (2016). *Molten Salt Fast Reactor: Shift from Burner to Breeder Moving on to the Thorium Era.* Master Thesis. Delft University of Technology.
2. Bijman, R. (2014). *Radiotoxicity and Decay Heat Comparison of Nuclear Waste Produced by a Thorium or Uranium Fuelled Pebble Bed Reactor.* Bachelor Thesis. Delft University of Technology.
3. Arthur, E. (2002). *Motivation and Programs for Transmutation of Nuclear Waste*. Lecture Notes: The 2002 Frederic Joliot-Otto Hahn Summer School, Cadarache, France.

4. Meshesha, A.Z. (2007). *Viability of Thorium-Based Reactors.* Master Thesis. Department of Physics - University of Surrey.
5. Nuclear Science. (2015). *Perspectives on the Use of Thorium in the Nuclear Fuel Cycle.* OECD NEA No. 7228.
6. Björk, K.I., & Fhager, V. (2009). Comparison of Thorium-Plutonium fuel and MOX fuel for PWRs. In *Proceedings of Global 2009*, 6–11 September 2009. Paris, France.
7. Björk, K.I. (2013). A BWR Fuel Assembly Design for Efficient Use of Plutonium in Thorium-Plutonium Fuel. *Progress in Nuclear Energy, 65*, 56–63.
8. Björk, K.I. (2014). Development of a fuel performance code for Thorium-Plutonium fuel. In *Proceedings of PHYSOR2014,* 28 September–3 October 2014. Kyoto, Japan.
9. Lau, C.H., Nylén, H., Björk, K.I., & Sandberg, U. (2014). Feasibility Study of 1/3 Thorium-Plutonium Mixed Oxide Core. *Science and Technology of Nuclear Installations, 2014*, Article ID 709415. DOI: 10.1155/2014/709415
10. Björk, K.I., Lau, C.W., Nylén, H., & Sandberg, U. (2013). Study of Thorium-Plutonium Fuel for Possible Operating Cycle Extension in PWRs. *Science Technology of Nuclear Installations*, Article ID 867561.
11. Fridman, E., & Kliem, S. (2011). Pu Recycling in a Full Th-MOX PWR Core. Part I: Steady State Analysis. *Nuclear Engineering and Design, 241* (1), 193–202.
12. NEA/NSCDOC 10. (2002). *A VVER-1000 LEU and MOX assembly computational Benchmark*. OECD NEA.
13. Goorley, J.T., James, M.R., Booth, T.E., Brown, F.B., Bull, J.S., Cox, L.J., … & Anthony, J. (2013). *Initial MCNP6 Release Overview – MCNP6 Version 1.0.* LA-UR-13–22934. Los Alamos National Laboratory.
14. Chadwick, M.B., Herman, M., Obložinský, P., Dunn, M.E., Danon, Y., Kahler, A.C., … & Young, P.G. (2011). ENDF/B-VII.1 Nuclear Data for Science and Technology: Cross Sections, Covariances, Fission Product Yields and Decay Data. *Nuclear Data Sheets, 112* (12), 2887–2996. DOI: 10.1016/j.nds.2011.11.002
15. Tran, V.T., Tran, H.N., Nguyen, H.T., Hoang, V.K., & Ha, P.N.V. (2019). Study on Transmutation of Minor Actinides as Burnable Poison in VVER-1000 Fuel Assembly. *Science and Technology of Nuclear Installations, 2019*, Article ID 5769147. DOI: 10.1155/2019/5769147
16. X-5 Monte Carlo Team (2003). *MCNP – A General Monte Carlo N-Particle Transport Code*, Version 5. LA-UR-03-1987.
17. Hendricks, J.S, McKinney, G.W., Fensin, M.L., James, M.R., Johns, R.C., Durkee, J. W., … & Johnson, M. W. (2008). *MCNPX 2.6.0 Extensions*. LA-UR-08-2216. Los Alamos National Laboratory.
18. Zuhair, Z., Dwijayanto, R.A.P., Sriyono, S., Suwoto, S., & Su'ud, Z. (2022). Preliminary Study on TRU Transmutation inVVER-1000 Fuel Assembly using MCNP6. *Kerntechnik, 87* (3), 305–315. DOI: 10.1515/kern-2021-1017
19. Hassan, M. (2020). Simulation of a Full PWR Core with MCNP6. *International Journal of Science and Research (IJSR), 9*, 913–918. DOI: 10.21275/SR20916224433
20. Zuhair, Z., Dwijayanto, R.A.P., Suwoto, S., & Setiadipura, T. (2021). The Implication of Thorium Fraction on Neutronic Parameters of Pebble Bed Reactor. *Kuwait Journal of Science, 48*, 1–16, DOI: 10.48129/kjs.v48i3.9984
21. Facchini, A., Giusti, V., Ciolini, R., Tuček, K., Thomas, D., & D'Agata, E. (2017). Detailed Neutronic Study of the Power Evolution for the European Sodium Fast Reactor during a Positive Insertion of Reactivity. *Nuclear Engineering and Design 313*, 1–9. DOI: 10.1016/j.nucengdes.2016.11.014
22. Zuhair, Z., Suwoto, S., Setiadipura, T., & Su'ud, Z. (2020). Study on MCNP6 Model in the Calculation of Kinetic Parameters for Pebble Bed Reactor. *Acta Polytechnica, 60,* 175–184. DOI: 10.14311/AP.2020.60.0175

23. Carter, J.P., & Borrelli, R.A. (2020). Integral Molten Salt Reactor Neutron Physics Study using Monte Carlo N-Particle Code. *Nuclear Engineering and Design, 365*, 110718. DOI: 10.1016/j.nucengdes.2020.110718
24. Zuhair, Z., Suwoto, S., Setiadipura, T., & Kuijper, J.C. (2019). Study on the Characteristics of Effective Delayed Neutron Fraction (*β*eff) for Pebble-Bed Reactor with Plutonium Fuel. *Iranian Journal of Science and Technology, Transactions A: Science, 43*, 3037–3045. DOI: 10.1007/s40995-019-00772-8.
25. Liem, P.H., Zuhair, Z., & Hartanto, D. (2019). Sensitivity and Uncertainty Analysis on the First Core Criticality of the RSG GAS Multipurpose Research Reactor. *Progress in Nuclear Energy, 114*, 46–60. DOI: 10.1016/j.pnucene.2019.03.001
26. Zuhair, Z., Suwoto, S., Setiadipura, T., & Kuijper, J.C. (2019). The Effects of Fuel Type on Control Rod Reactivity of Pebble-Bed Reactor. *Nukleonika, 64,* 131–138. DOI: 10.2478/nuka-2019-0017
27. Kabach, O., Chetaine, A., Benchrif, A., Amsil, H., & El Banni, F. (2021). A Comparative Analysis of the Neutronic Performance of Thorium Mixed with Uranium or Plutonium in a High-temperature Pebble-bed Reactor. *International Journal of Energy Research*, 1–18. DOI: 10.1002/er.6935.
28. Zuhair, Z., Suwoto, S., Setiadipura, T., & Su'ud, Z. (2017). The Effects of Applying Silicon Carbide Coating on Core Reactivity of Pebble-bed HTR in Water Ingress Accident. *Kerntechnik, 82* (1), 92–97. DOI:10.3139/124.110628.
29. Zuhair, Z., Suwoto, S., Permana, S., & Setiadipura, T. (2021). Study on Control Rod Reactivity of Small Pebble Bed Reactor with Wallpaper Fuel Design. Journal of Physics: Conference Series, *1772* (1), 012021. DOI: 10.1088/1742-6596/1772/1/012021
30. Mercatali, L., Venturini, A., Daeubler, M., & Sanchez, V.H. (2015). SCALE and SERPENT Solutions of the OECD VVER-1000 LEU and MOX Burnup Computational Benchmark. *Annals of Nuclear Energy, 83,* 328–341.